



COMILLAS

UNIVERSIDAD PONTIFICIA

ICAI

GRADO EN INGENIERÍA EN TECNOLOGÍAS INDUSTRIALES

TRABAJO FIN DE GRADO

ADHESIVE JOINTS IN COMPOSITE-METAL INTERFACES FOR FORMULA STUDENT COMPOSITE SUSPENSION

Autor: Alberto Caballero Valls

Director: Ignacio Granell Heredero

Madrid

julio de 2024

Declaro, bajo mi responsabilidad, que el Proyecto presentado con el título
ADHESIVE JOINTS IN COMPOSITE-METAL INTERFACES FOR
FORMULA STUDENT COMPOSITE SUSPENSION

en la ETS de Ingeniería - ICAI de la Universidad Pontificia Comillas en el
curso académico 2023-2024 es de mi autoría, original e inédito y
no ha sido presentado con anterioridad a otros efectos. El Proyecto no es
plagio de otro, ni total ni parcialmente y la información que ha sido tomada
de otros documentos está debidamente referenciada.



Fdo.: ALBERTO CABALLERO VALLS

Fecha: 03/ 07/ 2024

Autorizada la entrega del proyecto

EL DIRECTOR DEL PROYECTO :

Ignacio Granell Heredero

Fdo.:



Fecha: 10/07/2024



COMILLAS

UNIVERSIDAD PONTIFICIA

ICAI

GRADO EN INGENIERÍA EN TECNOLOGÍAS INDUSTRIALES

TRABAJO FIN DE GRADO

ADHESIVE JOINTS IN COMPOSITE-METAL INTERFACES FOR FORMULA STUDENT COMPOSITE SUSPENSION

Autor: Alberto Caballero Valls

Director: Ignacio Granell Heredero

Madrid

julio de 2024

Acknowledgements

Completing this final degree project has been a fulfilling endeavor, and I sincerely appreciate all the support and guidance I have received along the way.

I am profoundly grateful to my director, Ignacio Granell. Your knowledge and support have been critical to the success of this project. Your commitment to my academic growth has been deeply motivating.

My deepest gratitude goes to my family, whose constant support and encouragement have been my anchor throughout this journey.

Lastly, I want to extend my gratitude to all the ISC Racing Team members who have accompanied me during my years in the team. Your guidance and mentorship have been invaluable. Thank you.

UNIONES ADHESIVAS ENTRE METAL Y MATERIALES COMPUESTOS EN LA SUSPENSIÓN DE UN FORMULA STUDENT FABRICADA CON MATERIALES COMPUESTOS

Autor: Caballero Valls, Alberto.

Director: Granell Heredero, Ignacio.

Resumen

El objetivo de este proyecto es estudiar y mejorar las uniones adhesivas para su uso en sistemas de suspensión fabricados con materiales compuestos en un monoplaza de Formula Student. El estudio implica un análisis de distintos tipos de uniones, materiales y mejores técnicas. Además, el proyecto incluye la fabricación de componentes, seguida de ensayos en laboratorio para evaluar la correlación entre los resultados del análisis de elementos finitos (FEA) y los resultados del laboratorio.

Palabras clave: longitud de pegado, espesor de pegado, análisis de elementos finitos, unión a solape simple, adhesivo estructural, carga de tracción

1. Introducción

La industria del automovilismo de competición se basa en la búsqueda de los mejores diseños, centrándose en el desarrollo de componentes ligeros que proporcionan un rendimiento óptimo. En los últimos años, esta industria ha vivido el desarrollo de nuevos materiales y técnicas de fabricación avanzadas. Este proyecto tiene como objetivo determinar los parámetros geométricos óptimos de la unión adhesiva para un sistema de suspensión de un monoplaza de Formula Student, continuando el trabajo de Antonio Hernández-Briales en "Diseño y Fabricación de una Suspensión para Formula Student" (ANTO23) [1], en el cual el autor diseña una suspensión de un Formula Student desde la perspectiva de la dinámica del vehículo. Identificar estos valores óptimos de los parámetros contribuirá a la reducción del peso del sistema de suspensión al minimizar el volumen de metal de los insertos sin comprometer la seguridad. Se emplea análisis de elementos finitos para calcular los valores óptimos de los parámetros del adhesivo y los resultados se comparan con la literatura existente sobre uniones adhesivas. A continuación, se realizan ensayos en laboratorio para validar la precisión de las simulaciones. Finalmente, se presenta una guía completa de fabricación para asegurar la calidad de la unión. Los materiales utilizados en este estudio son aluminio 7075 T6, fibra de carbono y adhesivo estructural 3M DP420 NS.

2. Definición del proyecto

El proyecto sirve como guía para el diseño de los insertos metálicos y de la unión adhesiva de un sistema de suspensión de un Formula Student y asegura la calidad del proceso de unión. El inserto de aluminio, se adhiere a un tubo de fibra de carbono con adhesivo estructural, formando una barra de suspensión. Este proyecto investiga cómo

las modificaciones geométricas influyen en la distribución de las tensiones a lo largo del adhesivo y detalla los pasos necesarios para garantizar la calidad de la unión.

3. Descripción del modelo

Este modelo está diseñado para replicar el comportamiento real del adhesivo entre metal y materiales compuestos.

La imagen 1, la imagen 2 y la imagen 3 muestran la metodología utilizada, la cual se divide en tres fases.

La fase 1 comienza con el desarrollo de un modelo de simulación, el cual es validado mediante ensayos de tracción en un laboratorio. Para validar el modelo de simulación, se fabrica una barra de suspensión, la cual se simula bajo las mismas condiciones de contorno que en la máquina de ensayos y se somete a la carga que causa el fallo del adhesivo en los ensayos. El resultado de la simulación debe mostrar que el valor máximo de tensión en el adhesivo coincide con el esfuerzo cortante máximo del adhesivo.

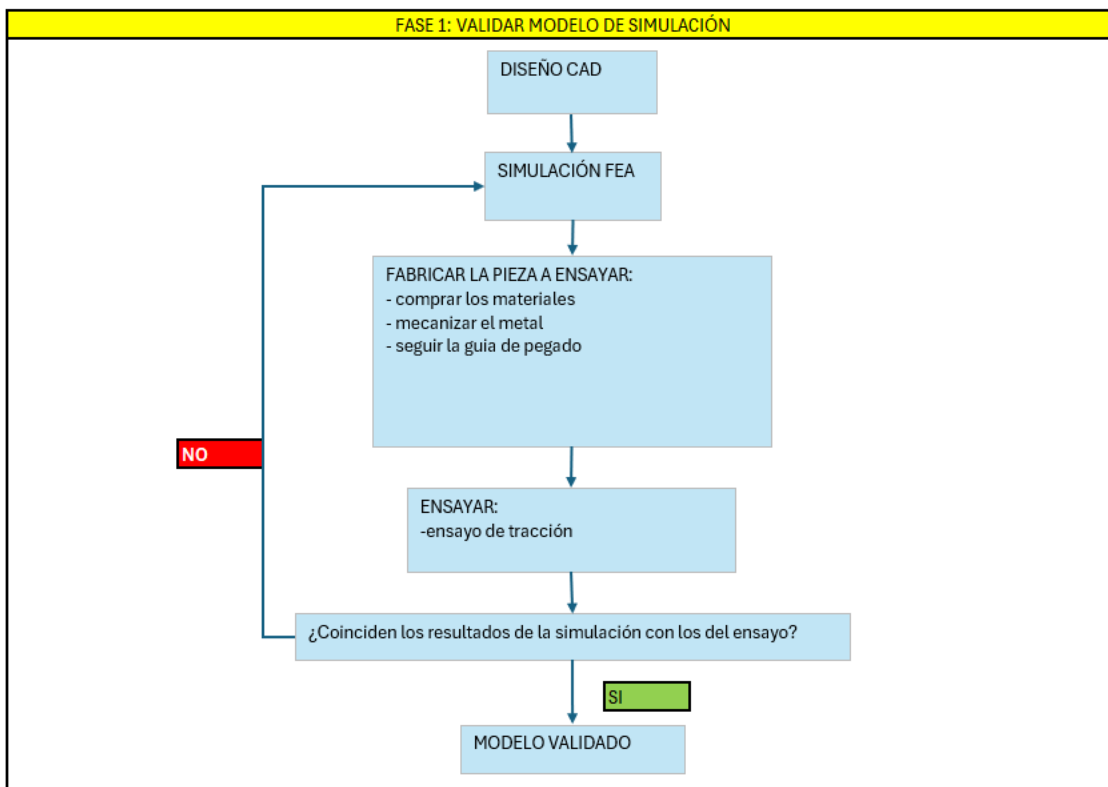


Imagen 1 fase 1: Validar modelo de simulación

La fase 2 incluye la investigación de la influencia de los valores de los parámetros geométricos del adhesivo en la distribución de tensiones del mismo.

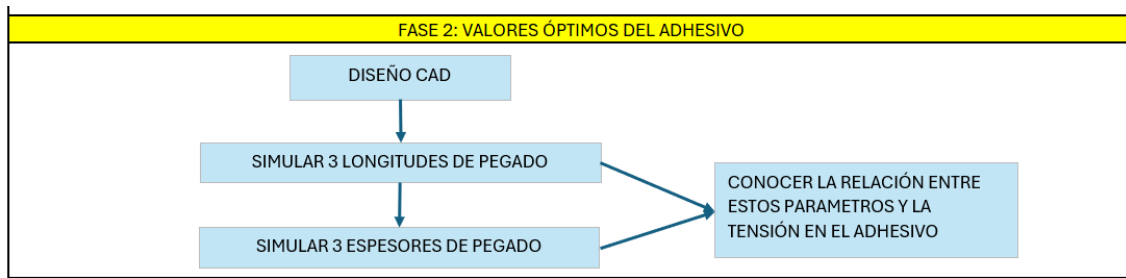


Imagen 2 Fase 2: valores óptimos de la geometría del adhesivo

Finalmente, el proyecto termina con el diseño de la pieza metálica y el dimensionado de la unión adhesiva. También se desarrolla una guía completa de unión para asegurar un rendimiento óptimo del adhesivo.

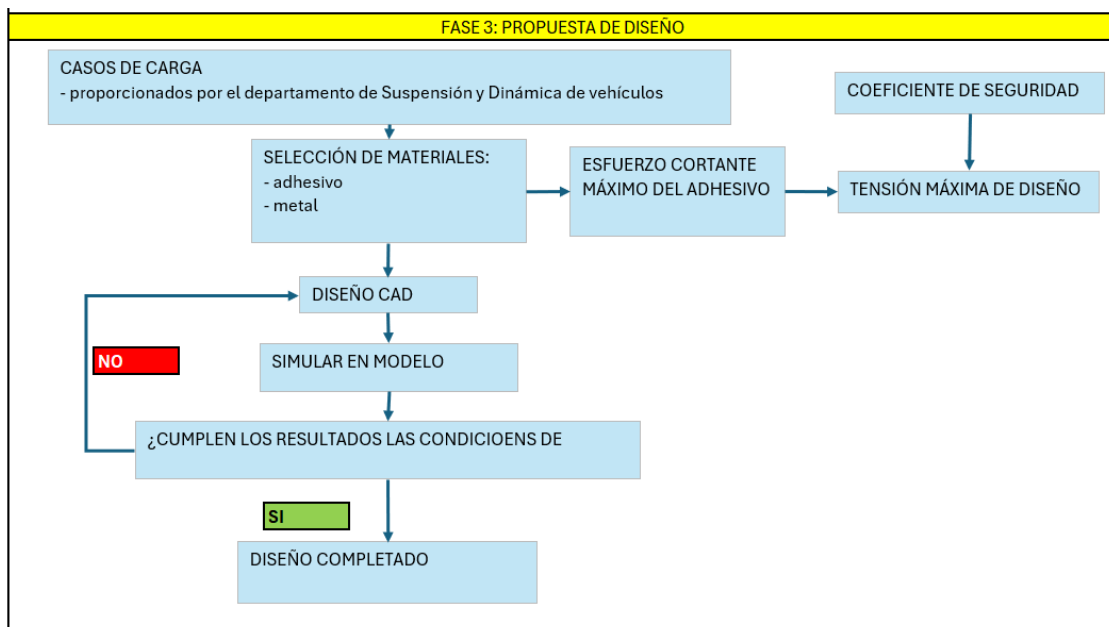


Imagen 3 Fase 3: diseño óptimo

Se realizan dos diseños de insertos metálicos distintos, uno usado para las fases 1 y 2, y otro para la fase 3. A continuación se explican los usos de ambos diseños.

Inserto usado para ensayar y simular (fase 1 y fase 2)

El diseño empleado en las fases 1 y 2 presenta una geometría diseñada para facilitar la fijación de la barra de suspensión a la máquina de tracción. La imagen 4 muestra el inserto utilizado para estas fases.



Imagen 4 vista CAD del inserto ensayado

La barra de suspensión utilizada para simular y ensayar debe incluir las siguientes características:

- Debe tener dos insertos metálicos, cada uno con un agujero pasante M6 cuya eje es perpendicular al eje axial del tubo de fibra de carbono, permitiendo fijar el inserto a la máquina de ensayos mediante un pasador que evita el movimiento desde la mordaza de la máquina.
- No debe tener chaflanes ni cilindrados interiores para reducir los costes de fabricación.
- Reducción de la longitud del tubo de fibra de carbono a 120 mm para minimizar los costes de fabricación y el desperdicio de material.

Para completar la simulación, la barra de suspensión se modela como cinco cuerpos:

- Dos insertos de aluminio en los extremo.
- Dos cuerpos entre el aluminio y el carbono con un espesor mayor a 0 mm que modelan el comportamiento del adhesivo.
- Un tubo de fibra de carbono.

La imagen 5 presenta una vista explosionada de la barra de suspensión usada para los ensayos y la imagen 6 muestra la barra de suspensión antes de ser ensayada.

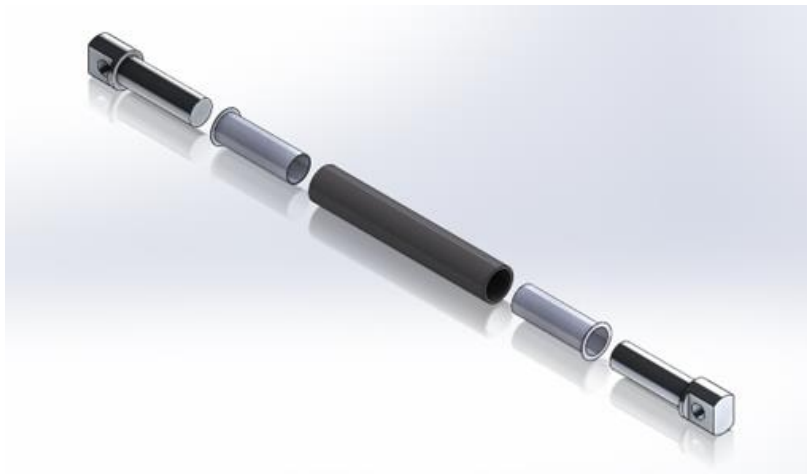


Imagen 5 Vista explosionada de la barra de suspensión ensayada



Imagen 6 Barra de suspensión ensayada

Se fabrican dos barras de suspensión y se someten a ensayos de tracción en laboratorio para validar los resultados de la simulación. La imagen 7 muestra la barra de suspensión siendo ensayada.



Imagen 7 Ensayo de tracción realizado

Una vez validada la simulación comparando los resultados del ensayo y de la simulación se termina la fase 1.

Para el análisis de la influencia de la variación de los parámetros geométricos del adhesivo en la distribución de tensiones en el adhesivo, se simulan tres longitudes de pegado y tres espesores de pegado distintos, manteniendo los mismos parámetros de simulación.

Una vez desarrollado un modelo de simulación para uniones adhesivas tubulares y comprendidos los efectos de la variación de los parámetros geométricos del adhesivo en la distribución de tensiones, se desarrolla un diseño que cumpla con las restricciones de diseño establecidas.

Propuesta de diseño (fase 3)

El diseño propuesto del inserto óptimo para montar en el coche se diferencia del diseño de las fases 1 y 2 debido a los distintos requisitos geométricos. La mayoría de las modificaciones se concentran en la región del inserto de aluminio donde interactúa con el pasador durante los ensayos y con las rótulas cuando está montado en el coche. Sin embargo, estas modificaciones no tienen un impacto significativo en los resultados de la simulación. Validar el modelo de simulación a través de los ensayos en laboratorio garantiza la precisión del modelo de simulación para este diseño, eliminando la necesidad de realizar ensayos de nuevo.

La barra de suspensión está diseñada para resistir el peor caso de carga de todas las barras, en lugar de dimensionar cada inserto a la fuerza máxima de cada barra de suspensión, con el objetivo de reducir los costes de fabricación. La imagen 8 presenta las cargas máximas para diferentes casos de carga. La barra de suspensión para esta carga está trabajando a

tracción, y la simulación replica esta condición, haciendo que el adhesivo experimente esfuerzos cortantes.

-279	-1659	-9371	-7735	-492	-1032	N	Fatigue (only in tension)
6262	2916	5878	2927	5937	4003	N	Buckling
6262	2916	5878	2927	5937	4003	N	Comp
-435	-2343	-14377	-12776	-811	-1427	N	Tens

Imagen 8 cargas máximas para distintos casos de carga

El diseño del inserto propuesto se muestra en la imagen 9. En este diseño se propone aumentar el espesor de pegado en los extremos para aliviar los picos de tensiones.

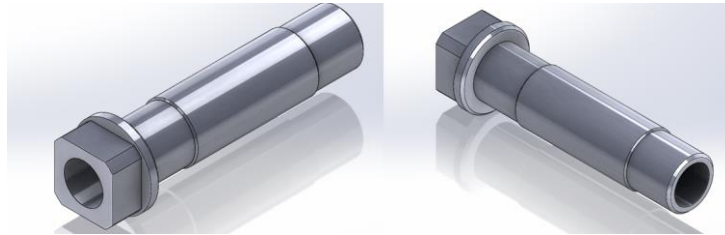


Imagen 9 Propuesta de diseño

Las condiciones de diseño son las siguientes:

- El tubo de fibra de carbono debe tener dimensiones de $\varnothing 15 \times 1.5$ mm.
- El inserto debe permitir roscar la rótula M6 mostrado en la imagen 10.
- El diseño debe soportar una carga de tracción de 14,377 N con un factor de seguridad de 3.
- Debe facilitar el apriete de la rótula roscada usando una llave inglesa.



Imagen 10 Rótula roscada M6

El adhesivo es el material con la menor resistencia a esfuerzo cortante en comparación con el aluminio y la fibra de carbono. El adhesivo seleccionado tiene una resistencia a esfuerzo cortante de 31 MPa a temperatura ambiente. Considerando un factor de seguridad de 3, la tensión máxima en el adhesivo debe ser inferior a 10.33 MPa cuando se somete a la carga máxima de tracción de 14,377 N. La imagen 11 presenta las propiedades mecánicas del adhesivo seleccionado, el cual es el 3M Scotch DP 420 NS, un adhesivo estructural bicomponente.

	viscosity at 24°C [Pa s]	mixture life at 24°C [min]	Peel strength at 24°C [N/cm]	shear strength [Mpa]		
				-55°C	24°C	82°C
DP 420 NS	180000	20	133	31	31	9

Imagen 11 Propiedades del adhesivo elegido

4. Resultados

Fase 1: Validación del modelo de simulación

Se realizan dos ensayos de tracción con dos barras de suspensión. Los resultados del mejor ensayo de tracción se muestra en la imagen 12. Se observa que el adhesivo falla a una fuerza de 13012 N. Para verificar el modelo de simulación, la misma barra de suspensión que ha sido ensayada se simula con la carga que provoca el fallo del adhesivo con las mismas condiciones de contorno.

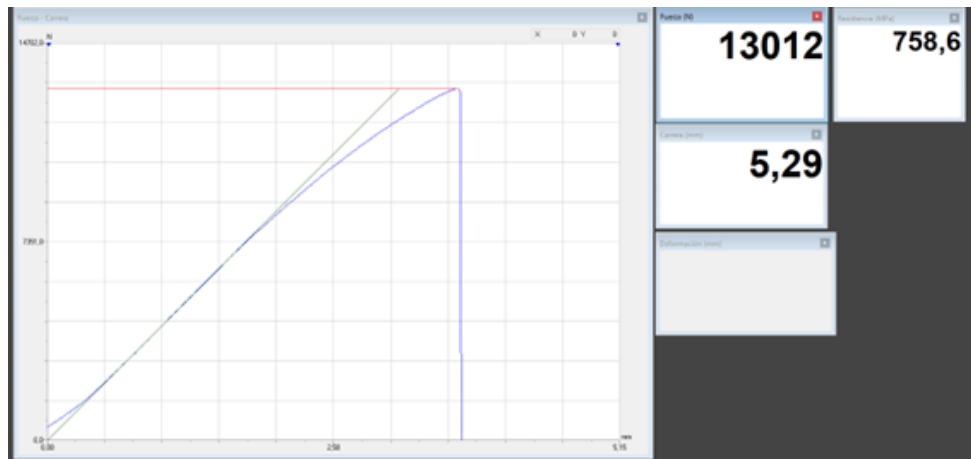


Imagen 12 Resultados del ensayo de tracción

La imagen 13 muestra la barra de suspensión antes y después del ensayo.



Imagen 13 Barra de suspensión antes (izquierda) y después (derecha) de ser ensayada

Los resultados de la simulación se presentan en la imagen 14. Estos resultados indican un tensión máximo en el adhesivo de 32.315 MPa en un extremo y 27.416 MPa en el otro inserto. Estos resultados coinciden con los resultados de los ensayos, ya que un extremo del inserto superó el tensión cortante máximo del adhesivo de 31 MPa exactamente en la carga que provoca el fallo, mientras que el otro extremo permaneció pegado.



Imagen 14 Correlación entre la simulación y los ensayos

Análisis la influencia de la geometría del adhesivo en la distribución de tensiones

Los resultados del análisis de longitud del adhesivo se muestran en la imagen 15. Este gráfico representa la variación de la tensión en el adhesivo con la variación de la longitud del adhesivo. En este gráfico se representan los valores mínimo, promedio y máximo para longitudes de adhesivo de 30 mm, 37.5 mm y 45 mm.

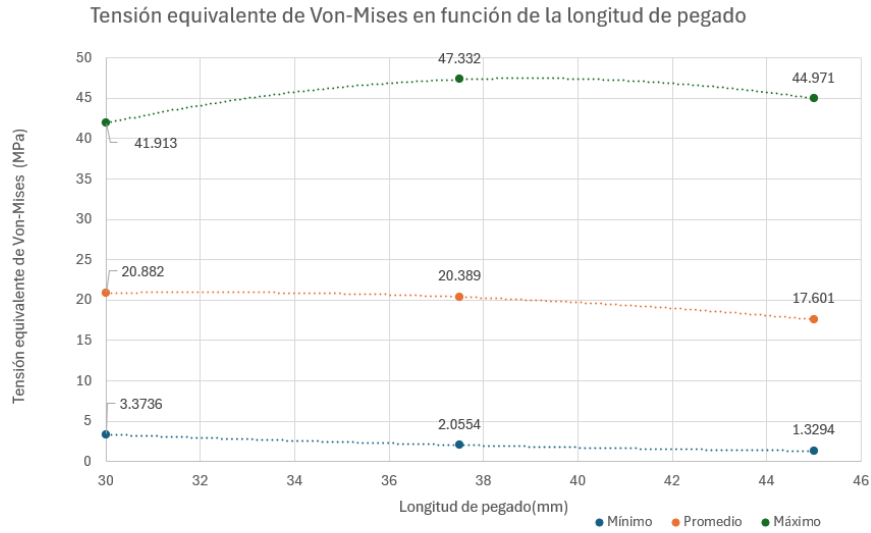


Imagen 15 Variación de la tensión con la longitud de pegado

La tabla 1 presenta una representación gráfica de los resultados de las simulaciones de las longitudes de pegado. La tabla muestra una vista lateral del adhesivo, mostrando los contornos de distribución de tensiones en el adhesivo con una escala de colores.

Longitud del adhesivo (mm)	Vista lateral
30	
37.5	
45	

50
42.913 Max
35
30
25
20
15
10
5
3.3736 Min

Tabla 1 Comparativa de la longitud de pegado

La imagen 16 presenta la evolución de los valores máximos, mínimos y promedio de tensión para tres diferentes espesores de adhesivo, los cuales son 0.15 mm, 0.3 mm y 0.6 mm, manteniendo constante una longitud de adhesivo de 45 mm.

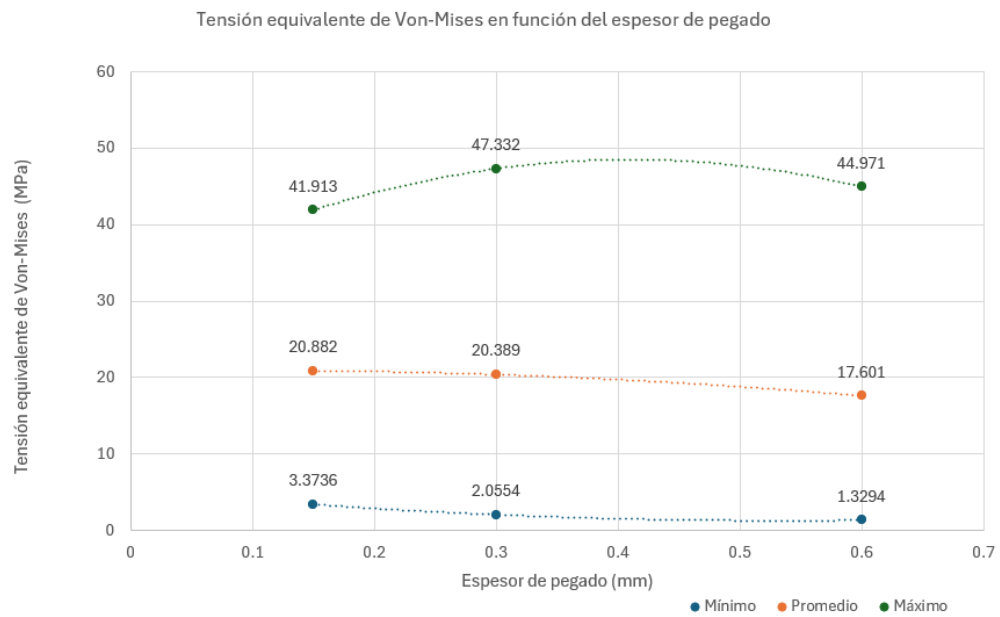


Imagen 16 Variación de la tensión con el espesor de pegado

La tabla 2 muestra una representación gráfica de los resultados de las simulaciones anteriores sobre el espesor de pegado.

Esesor de pegado (mm)	Vista lateral
0.15	
0.30	
0.60	

50
42.913 Max
35
30
25
20
15
10
5
3.3736 Min

Tabla 2 Comparativa del espesor de pegado

Propuesta de diseño

Los resultados del diseño óptimo propuesto del inserto metálico y de la unión adhesiva se presentan en la tabla 3, donde se muestran los valores mínimo, máximo y promedio de la distribución de tensiones en el adhesivo. La imagen 17 muestra la distribución de tensiones representada con una escala de colores.

Tabular Data				
	Time [s]	<input checked="" type="checkbox"/> Minimum [MPa]	<input checked="" type="checkbox"/> Maximum [MPa]	<input checked="" type="checkbox"/> Average [MPa]
1	1.	0.14691	8.884	5.8672

Tabla 3 Resultados de la simulación del diseño propuesto

G: EF-5-45
Equivalent Stress
Type: Equivalent (von-Mises) Stress
Unit: MPa
Time: 1
6/30/2024 10:46 AM

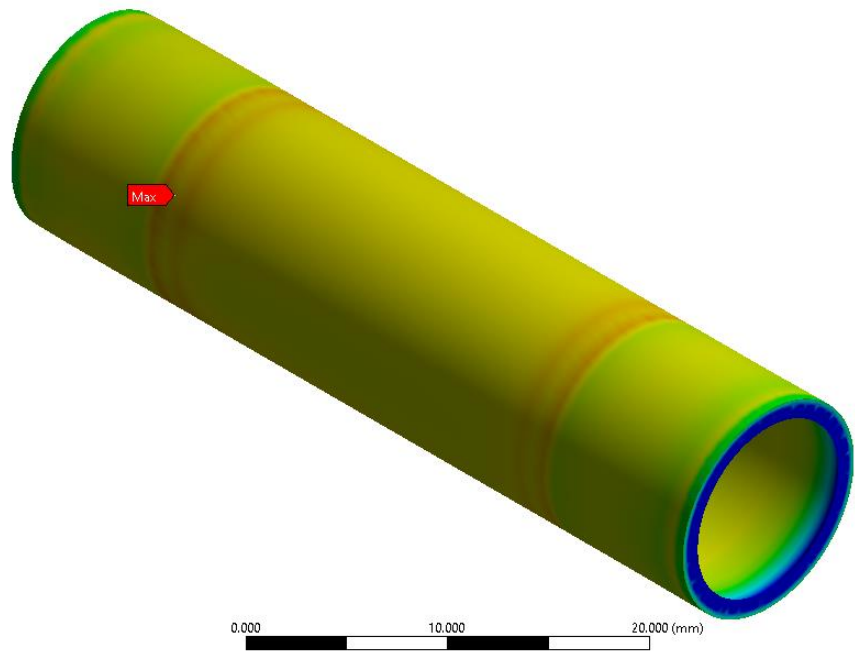
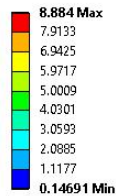


Imagen 17 Distribución de tensiones del diseño propuesto

El tensión máximo en el adhesivo es 8.884 MPa, lo cual está por debajo del objetivo de carga seleccionado de 10.3 MPa.

5. Conclusiones

Las conclusiones de este proyecto son las siguientes:

- El modelo de simulación está validado y puede utilizarse para diseñar uniones adhesivas entre materiales compuestos y metal.
- Los picos de tensiones cerca de las caras laterales permanecen constantes al aumentar la longitud del adhesivo.
- A medida que aumenta la longitud del adhesivo, el valor mínimo de tensión disminuye siguiendo una relación lineal. El valor promedio de tensión muestra una distribución cóncava, alcanzando un valor máximo a los 40 mm. El valor máximo de tensión sigue una distribución cóncava, alcanzando un máximo de 48 MPa, demostrando que aumentar la longitud del adhesivo no implica que el adhesivo resistirá más carga.
- El valor mínimo de tensión muestra una relación lineal directa con el espesor del adhesivo. Por otro lado, el valor promedio sigue una distribución cóncava, mientras que los valores máximos de tensión muestran una relación convexa. El valor promedio de tensión alcanza su máximo a 0.3 mm y su mínimo a 0.6 mm.
- Aumentar el espesor de pegado no asegura que la unión adhesiva sea más resistente, ya que aparecen problemas de porosidad y falta de adhesión.
- Para este diseño, el espesor de adhesivo más óptimo es la combinación de 0.3 mm en el centro del inserto y 0.6 mm en los bordes para reducir los picos de tensión.

El diseño propuesto del inserto metálico y de la unión adhesiva:

- Reduce el tensión cortante máximo en un 81.63%, de 48.354 MPa a 8.884 MPa.
- Reduce el tensión cortante promedio en un 64.54%, de 16.546 MPa a 5.8672 MPa.
- Reduce el tensión cortante mínimo en un 76.70%, de 0.6307 MPa a 0.1469 MPa.
- Reduce el peso en un 23.87%, de 10.81 g a 8.23 g.
- Trabaja con un factor de seguridad de tres bajo la carga más crítica.

6. Referencias

- [ANTO23] [1] Briales, A. H.-R. (2023). *Design and manufacture of a Formula Student Suspension*. Madrid: Universidad Pontificia Comillas.

ADHESIVE JOINTS IN COMPOSITE-METAL INTERFACES FOR FORMULA STUDENT COMPOSITE SUSPENSION

Author: Caballero Valls, Alberto.

Director: Granell Heredero, Ignacio.

Abstract

The objective of this project is to examine and enhance adhesive joints specifically for use in Formula Student composite suspension systems. The investigation involves a comprehensive analysis of various suspension joint types, materials, and best practices. Additionally, the project involves the manufacturing of components, followed by testing to assess the correlation between Finite Element Analysis (FEA) results and real-world outcomes.

Keywords: adhesive length, adhesive thickness, finite element analysis, single lap joint, structural adhesive tensile load

1. Introduction

The motorsport industry is driven by the pursuit of the best designs, emphasizing the development of lightweight components that deliver optimal performance. In recent years, this industry has witnessed the development of new materials and advanced manufacturing techniques. This project aims to determine the optimal adhesive geometric parameters for a Formula Student suspension system, continuing the work of Antonio Hernandez-Briales in Design and Manufacture of a Formula Student Suspension (ANTO23) [1], in which the author designs a Formula Student suspension from a vehicle dynamics perspective. Identifying these parameters will contribute to the reduction of the car weight by minimizing the volume of the metal end-fitting without compromising safety standards. Finite element analysis is employed to determine the optimal adhesive parameters values and the results are compared with existing literature on adhesive lap joints. Subsequently, testing is conducted to validate the accuracy of the simulations. Finally, a complete manufacturing guide is presented to ensure the quality of the bonding. The materials used in this study are aluminum 7075 T6, carbon fiber and 3M DP420 NS structural adhesive.

2. Project definition

The project serves as a guide for the design of the end-fittings of a Formula Student suspension system and ensures the quality of the bonding process. The end-fitting, made of aluminum, is adhered to a carbon fiber tube with structural adhesive, forming a suspension arm. This project investigates how geometric modifications influence the stress distribution along the adhesive and outlines the necessary steps to guarantee bonding quality.

3. Description of the model

This model is designed to replicate realistic adhesive behavior at the interface between metal and composite materials. The primary objective is to understand how modifications in the adhesive geometric parameters influence the stress distribution, with the aim of optimizing the design of the end-fitting. The model will then be validated through testing. Finally, the validated model will be employed to design the optimum end-fitting.

Figure 1, Figure 2 and Figure 3 illustrates the methodology used, which is divided into three phases.

Starting with the development of a simulation model in phase 1, which is validated through testing. During this phase, a suspension arm is manufactured and subjected to testing.

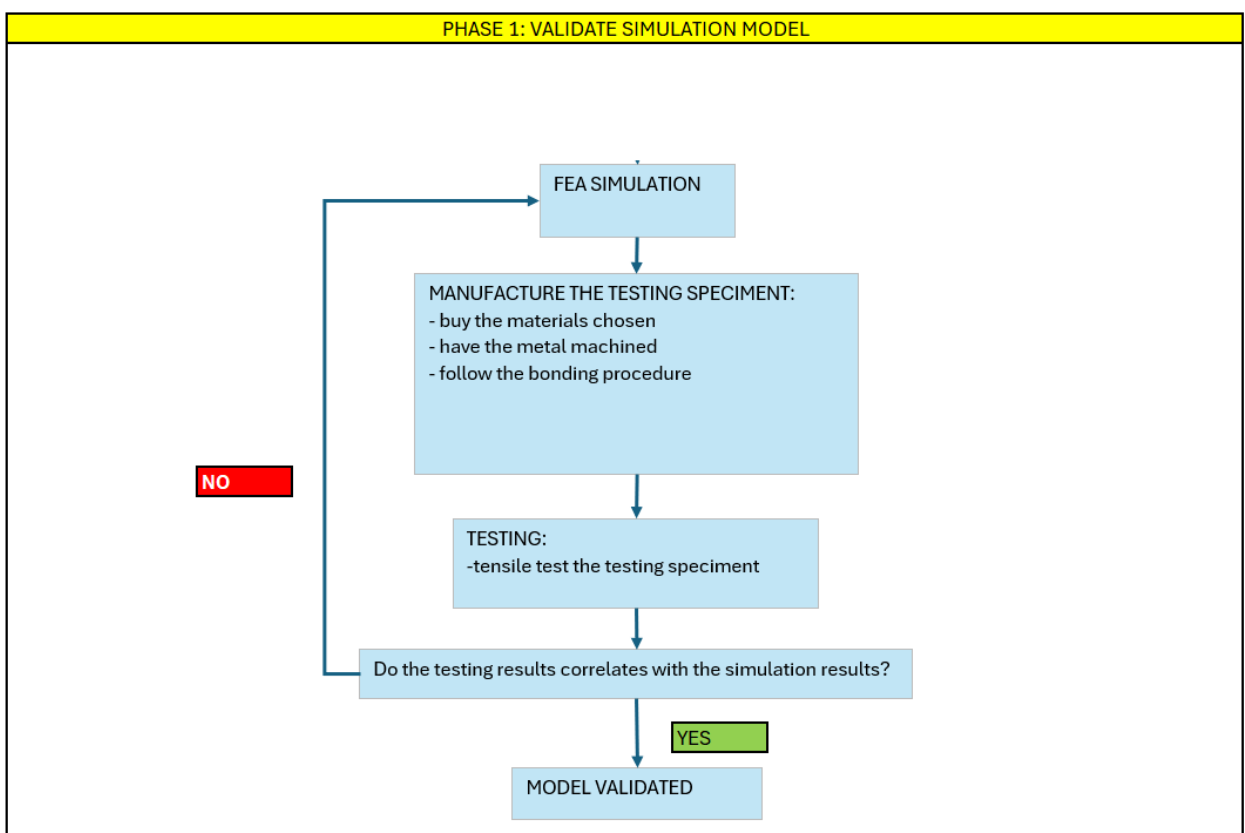


Figure 1 Phase 1: Validate simulation model

Continuing, phase 2 includes the research into the influence of adhesive geometric parameters on the adhesive stress distribution.

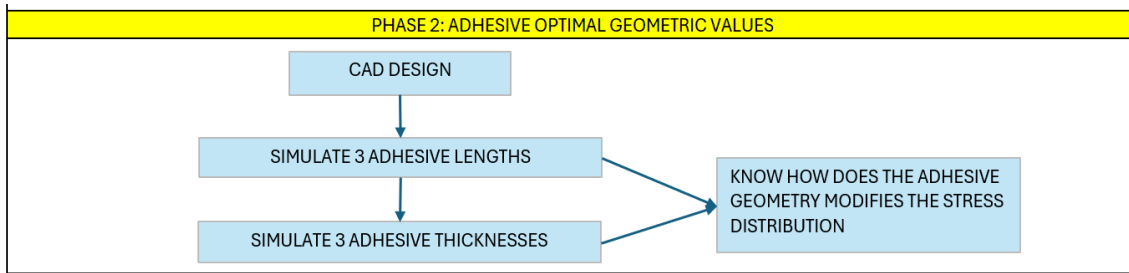


Figure 2 Phase 2: Adhesive optimal geometric values

Finally, the project involves the design of the optimum end-fitting and the elaboration of a complete bonding guide to ensure optimal adhesive performance.

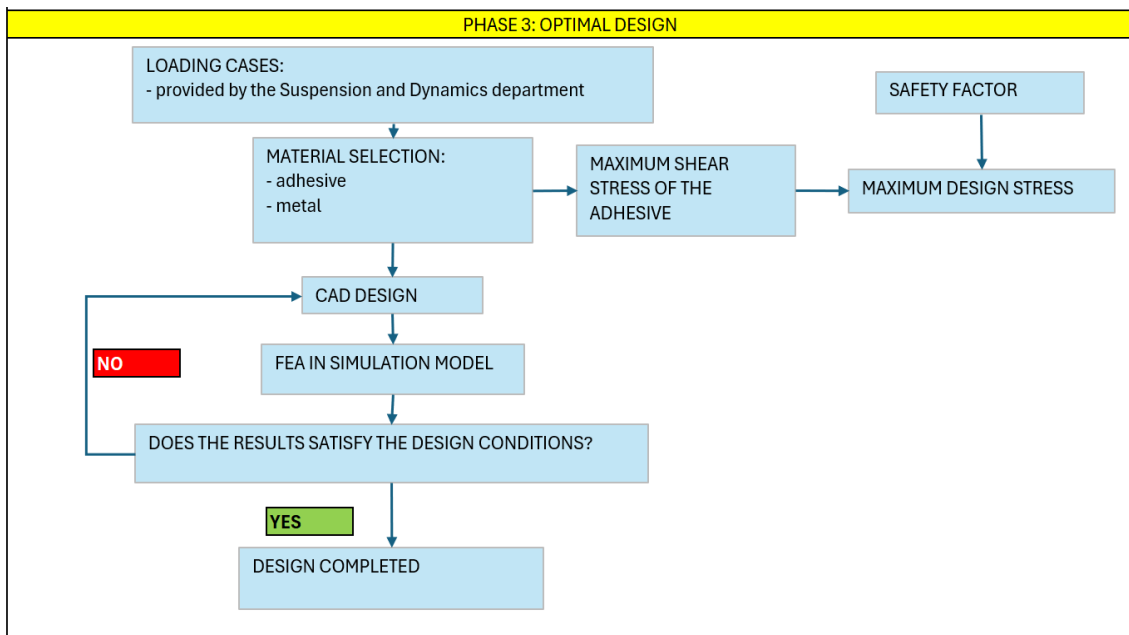


Figure 3 Phase 3: optimal design

End-fitting model for testing and validating the simulation model

Phase 1 and 2 use a suspension arm model with a geometry designed to facilitate the attachment of the end fitting to the testing machine, as it will be fabricated for testing purposes to validate the simulation. Figure 4 illustrates the end-fitting used in phase 1 and 2.



Figure 4 CAD view of the testing end-fitting model

The suspension arm model used for simulation and testing must include the following features:

- Two metal end-fittings, each one with a M6 hole which centerline is perpendicular to the axial axis of the carbon fiber tube, allowing fixing the end fitting to the testing machine using a pin that prevents movement from the machine's clamp.
- The omission of fillets and internal cylindrical features to reduce manufacturing costs.
- A reduction of the carbon fiber tube length to 120 mm to minimize manufacturing costs and material waste.

In order to complete the simulation the assembly is modeled as five bodies, which are:

- Two aluminum end-fittings.
- Two bodies between the aluminum and the carbon fiber with a thickness greater than 0mm that model the adhesive behavior.
- One carbon fiber tube.

Figure 5 illustrates an exploded view of the suspension arm used for testing and Figure 6 shows the suspension arm manufactured before being tested.

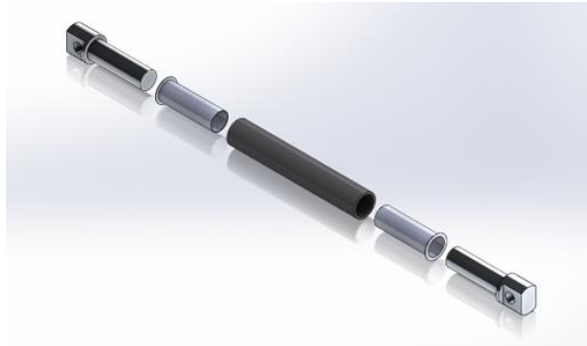


Figure 5 Exploded view of the suspension arm used for testing



Figure 6 Suspension arm used for testing manufactured

Two suspension arms are manufactured and subjected to testing to validate the simulation results. Figure 7 exhibits the suspension arm being tested.



Figure 7 Suspension arm testing

To validate the simulation model, the suspension arm is simulated under the same boundary conditions as in the testing machine and subjected to the load that causes the adhesive to fail in the testing. The simulation result must show that the maximum stress in the adhesive is the adhesive maximum shear stress.

Once the simulation is validated and the effects of adhesive geometric parameters on the stress distribution are understood, a design that meets the load requirements and constraints is developed.

End-fitting design proposed

The proposed end-fitting design intended for installation in the car differs from the testing design due to distinct geometric requirements. The majority of modifications are concentrated in the aluminum end fitting region where it interfaces with the pin during testing and with the rod end when it is installed in the car. However, these modifications do not have a significant impact on the simulation results. Validating the testing design through simulation ensures the accuracy of the simulation model for this design, negating the need for manufacturing and physical testing again.

The suspension arm is designed to withstand the highest load case for all the arms instead of having each end-fitting tailored to the maximum force of each suspension arm, aiming to reduce manufacturing costs. Figure 8 presents the maximum loads for different load scenarios. The suspension arm works under tensile stress, and the simulation replicates this condition, forcing the adhesive to experience shear stress.

-279	-1659	-9371	-7735	-492	-1032	N	Fatigue (only in tension)
6262	2916	5878	2927	5937	4003	N	Buckling
6262	2916	5878	2927	5937	4003	N	Comp
-435	-2343	-14377	-12776	-811	-1427	N	Tens

Figure 8 Maximum loads for different load cases

The end-fitting design proposed is illustrated in Figure 9.

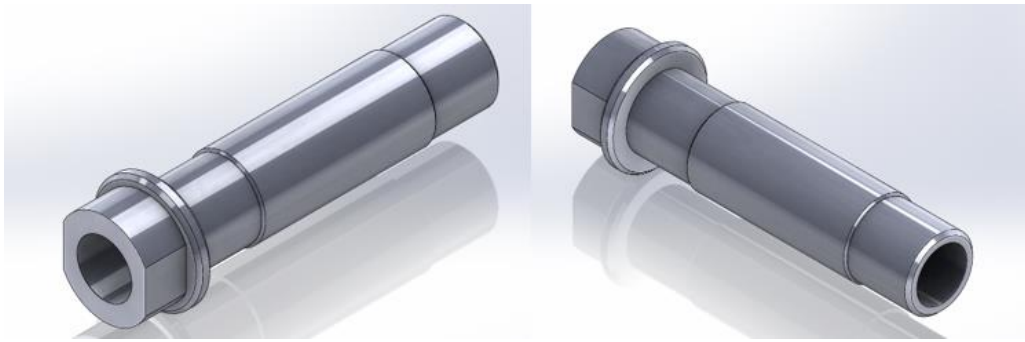


Figure 9 End-fitting design proposed

The design specifications are as follows:

- The carbon fiber tube must have dimensions of $\varnothing 15 \times 1.5 \times 120$ mm.
- The end-fitting must accommodate the M6 male rod end shown in Figure 10.
- The design must support a tensile load of 14,377 N with a safety factor of 3.
- It must facilitate the tightening of the rod end using a wrench.



Figure 10 M6 male rod end

The adhesive is the material with the lowest shear strength compared to aluminum and carbon fiber. The adhesive selected has a shear strength of 31 Mpa at ambient temperature. Considering a safety factor of 3, the maximum stress in the adhesive must be below 10 MPa when subjected to the maximum tensile load of 14377 N. Figure 11 presents the mechanical properties of the adhesive selected.

	viscosity at 24°C [Pa s]	mixture life at 24°C [min]	Peel strength at 24°C [N/cm]	shear strength [Mpa]		
				-55°C	24°C	82°C
DP 420 NS	180000	20	133	31	31	9

Figure 11 Properties of the adhesive chosen

4. Results

End-fitting design proposed

The results for the optimum design of the end-fitting that will be installed in the car are presented in Table 1, where the minimum, maximum and average values of the stress distribution in the adhesive are shown. Figure 12 illustrates the stress distribution plotted with a color scale.

Tabular Data			
Time [s]	Minimum [MPa]	Maximum [MPa]	Average [MPa]
1	0.14691	8.884	5.8672

Table 1 Simulation results for the design proposed

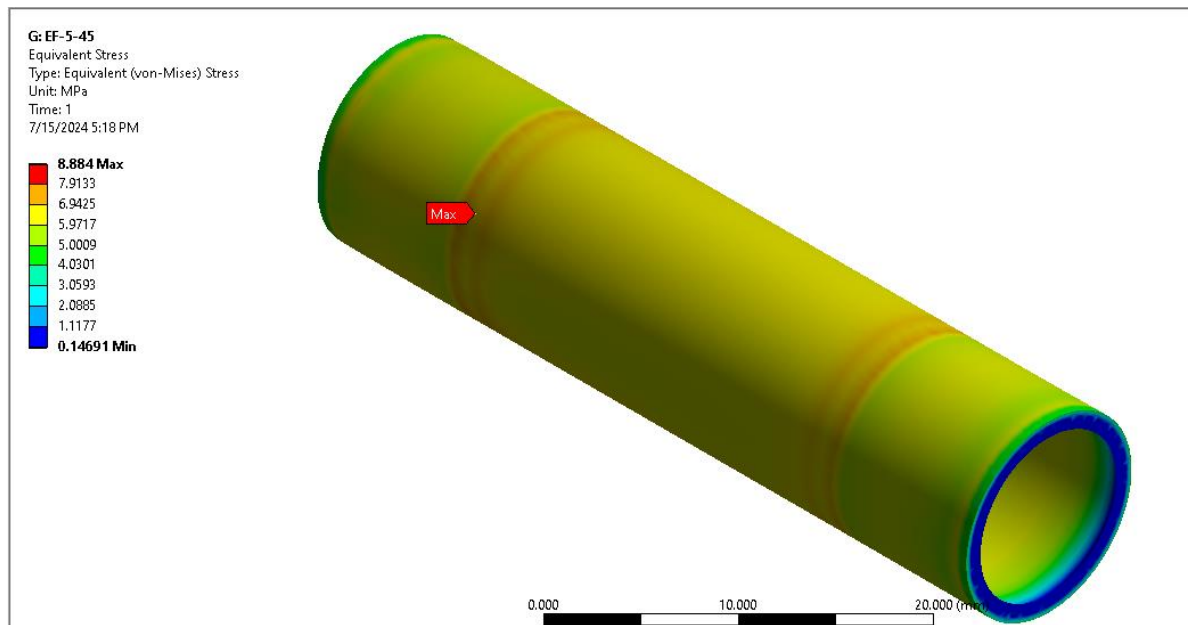


Figure 12 Stress distribution for the design proposed

The maximum stress in the adhesive measures 8.884 MPa, which is below the targeted design load goal of 10 MPa.

End-fitting model for the adhesive geometric parameters investigation

The results for the adhesive length analysis are shown in Figure 13. This chart depicts the variation of the stress with the variation of the adhesive length. Minimum, average and maximum values are plotted in this chart for adhesive lengths of 30mm, 37.5mm and 45mm.

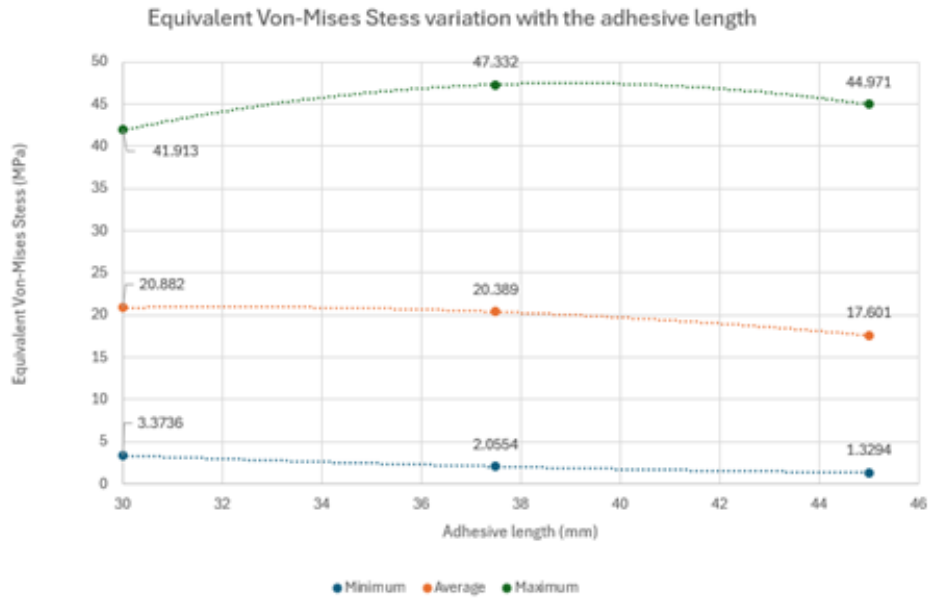



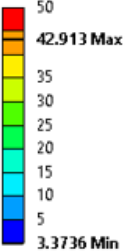


Figure 13 Equivalent Von-Mises stress variation with the adhesive length

Table 2 reveals a graphical representation of the results of the previous adhesive lengths simulations. The table below shows a lateral view of the adhesive, plotting the stress distribution contours in the adhesive with a color scale.

Adhesive length (mm)	Lateral view
30	
37.5	
45	



50
42.913 Max
35
30
25
20
15
10
5
3.3736 Min

Table 2 Adhesive length comparison

Figure 14 presents the evolution of the maximum, minimum and average stress values for three different adhesive thickness, which are 0.15mm, 0.3mm and 0.60mm maintaining an adhesive length constant of 45mm.

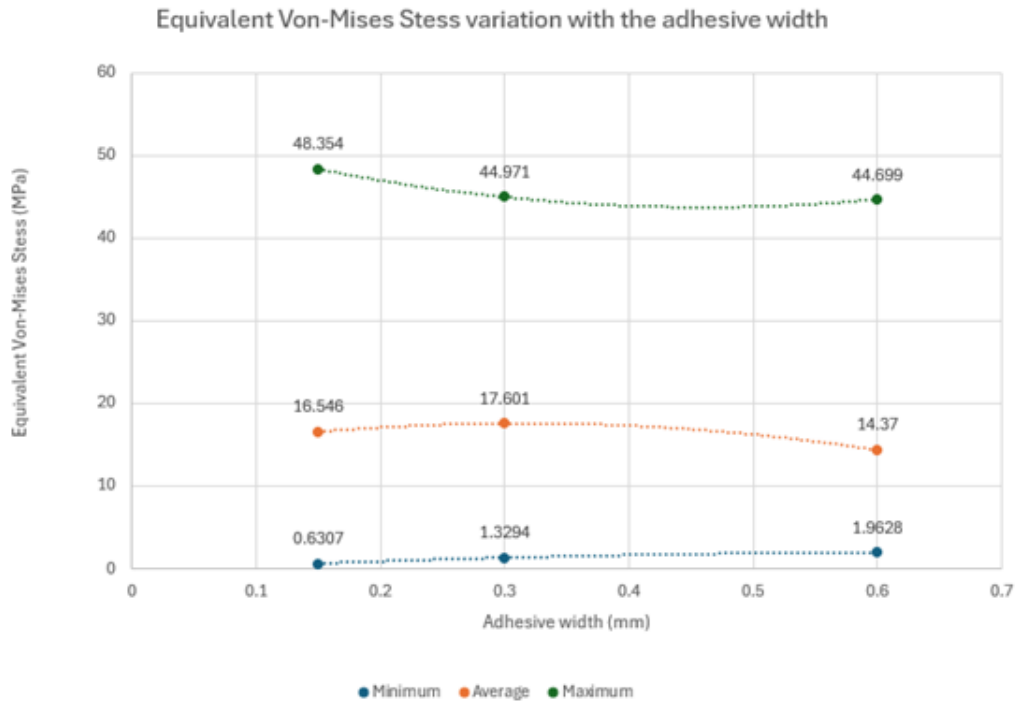


Figure 14 Equivalent Von-Mises stress variation with the adhesive thickness

Table 3 illustrates a graphical representation of the results of the adhesive thickness configurations mentioned before.

Adhesive thickness (mm)	Lateral view
0.15	
0.30	
0.60	

Table 3 Adhesive thickness comparison

Simulation model validation

The testing suspension arm is assembled for testing to validate the simulation model. The results of the tensile test are shown in Figure 15. It can be observed that the adhesive bond fails at a force of 13012N. To verify the simulation model, the same suspension arm that has been tested is simulated with the same boundary conditions.

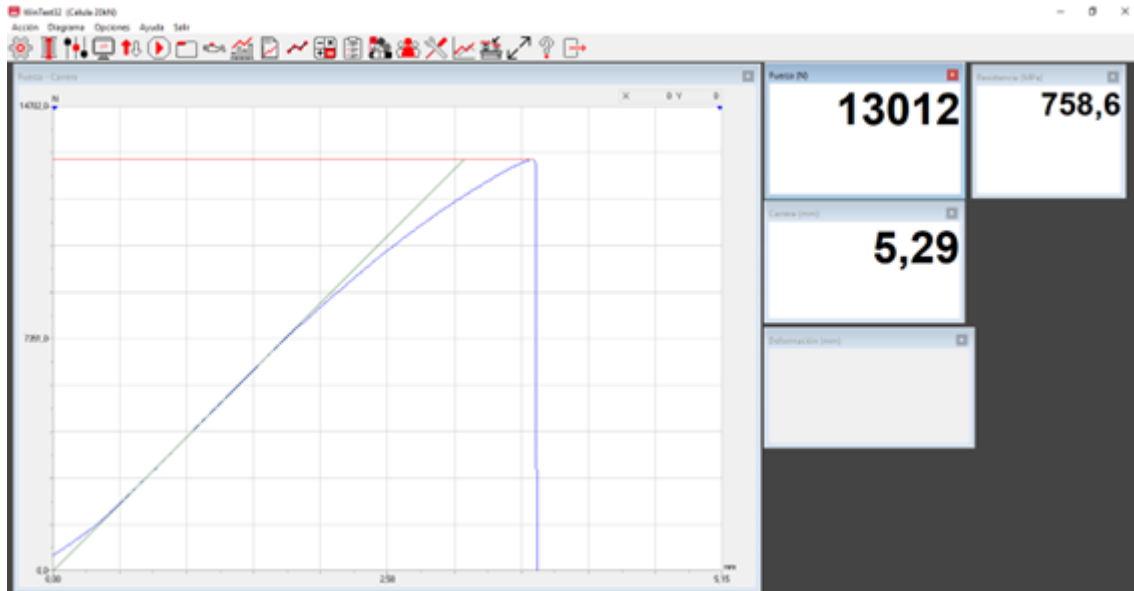


Figure 15 Tensile test results

Figure 16 illustrates the testing end-fitting assembly before and after testing.



Figure 16 Testing end-fitting before (left) and after (right) testing

The results of the simulation are presented in Figure 17. This results indicate a maximum stress in the adhesive of 32.315 MPa at one end fitting and 27.416 MPa in the other one. These results correlate with the testing outcomes, as one end fitting exceeded the adhesive's maximum shear stress of 31 MPa exactly at the failure load, while the other end fitting remained adhered.



Figure 17 Correlation between testing and simulating

5. Conclusions

The conclusions of this study are as follows:

- The simulation model is validated and can be used for designing adhesives joints in the composite-metal interface.
- Peak stresses near the lateral faces remain largely unchanged with the increasement of the adhesive length.
- As the adhesive length increases, the minimum stress value decreases, following a linear relationship. In contrast, the average stress value shows a concave distribution, with a maximum value at 40 mm. The peak stress value follows a concave distribution, reaching a maximum of 48 MPa, demonstrating that increasing the adhesive length does not imply that the adhesive will resist more load.
- The minimum stress value shows a direct linear relationship with adhesive thickness. Conversely, the average value follows a concave distribution, whereas the maximum stress values exhibit a convex relationship. The average stress peaks at 0.3 mm and reaches its minimum at the 0.6 mm.
- Increasing the adhesive thickness does not result in lower stress values. The adhesive thickness does not have a linear relation with the stress values.
- For this design the most optimum adhesive thickness is the combination of 0.3 mm at the center of the end-fitting and 0.6 mm at the edges to reduce peak stresses.

The end-fitting design proposed:

- Reduces the maximum shear stress 81.63%, from 48.354 MPa to 8.884MPa
- Reduces the average shear stress 64.54%, from 16.546 MPa to 5.8672 MPa
- Reduces the minimum shear stress 76.70%, from 0.6307 MPa to 0.14691 MPa
- Reduces the weight 23.87%, from 10.81g to 8.23g
- Works in the worst case load with a safety factor of three.

6. References

(ANTO23) [1] Briales, A. H.-R. (2023). *Design and manufacture of a Formula Student Suspension*. Madrid: Universidad Pontificia Comillas.

TABLE OF CONTENTS

<i>LIST OF TABLES</i>	4
<i>LIST OF FIGURES</i>	5
<i>LIST OF SYMBOLS AND ABBREVIATIONS</i>	8
1. INTRODUCTION	9
1.1 Formula student	9
1.2 ISC Racing Team	9
1.3 Aim of this project.....	10
1.4 Objective.....	10
1.5 Motivation.....	10
1.5 Methodology.....	11
1.6 Resources to use	13
1.7 History of composites in formula 1	14
1.8 Literature review.....	17
2. BONDED JOINTS	19
2.1 Bonded joints introduction	19
2.2 Bonded joints geometries	19
2.2.1 Single lap joint (SLJ).....	21
2.3 Methods to predict properties	21
2.4 Types of adhesives.....	22
2.4.1 Structural epoxy adhesives	22
2.4.2 Anaerobic adhesives	23
2.4.3 Cyanoacrylates adhesives	23
2.5 Bonding preparation	24
2.6 Effects of geometry modifications	25
2.6.1 Adhesive thickness	25
2.6.2 Tapering the adhesive	26
2.6.3 Bond overlap	26
2.6.4 Overlap stress distribution	28

2.7	Effect of environmental conditions	29
2.7.1	Temperature effects	29
2.6.2	Humidity effects	30
2.8	FEA analysis	30
2.9	Loading regimes	31
2.9.1	Fatigue loading analysis	33
2.10	Types of failure	34
2.10.1	Adhesive failure.....	34
2.10.2	Cohesive failure.....	34
2.10.3	Substrate failure.....	35
3.	<i>MATERIAL SELECTION</i>	37
3.1	Sorting stages.....	37
3.1.1	Stage 1: material family.....	38
3.1.2	Stage 2: material properties.	40
3.1.3	Stage 3. First graphical representation	41
3.1.4	Stage 4: Second graphical representation.....	42
3.2	Selection results.....	43
4.	<i>ADHESIVE SELECTION</i>	45
5.	<i>GUIDE FOR MANUFACTURING</i>	47
5.1	Required items.....	47
5.2	CFRP tube preparation procedure	47
5.3	Aluminum end-fittings procedure	48
5.4	Bonding procedure	48
6.	<i>CAD DESIGNS</i>	51
7.	<i>SIMULATIONS</i>	53
7.1	<i>simulation characteristics</i>	53
7.1.1	Engineering data	54
7.1.2	Simulation parameters	57
7.2	<i>Simulation results</i>	60
7.2.1	Adhesive length simulation	60
7.2.2	Adhesive thickness simulations.....	64
7.2.3	Testing boundary conditions simulation.....	66

7.2.4 Optimum design	68
7.3 <i>Simulations conclusions</i>	69
8. TESTING.....	73
8.1 Testing results	74
8.2 Simulation validation results	76
8.3 Testing conclusions.....	78
9. FUTURE PROJECTS.....	79
10. References.....	81
ANNEX I SUSTAINABLE DEVELOPMENT GOALS	87
ANNEX II DRAWINGS	91

LIST OF TABLES

Table 1 Database chosen in the material selection process	37
Table 2 Aluminum series	39
Table 3 Material selection process summary	43
Table 4 Optimal materials for this application	43
Table 5 Comparison between different adhesives	45
Table 6 Adhesive length simulations results	60
Table 7 Adhesive thickness simulations results	64
Table 8 Differences between EF-1-45 and EF-4-45. Values in MPa.....	67
Table 9 EF-5-45 Simulation results.....	68
Table 10 Adhesive length comparison. Visual representation.....	70
Table 11 Adhesive thickness comparison. Visual representation	71
Table 12 Differences between EF-1-45 and EF-4-45	72

LIST OF FIGURES

figure 1 Formula Student competition.....	9
figure 2 IFS 02 (left) and IFS 05 (right)	10
figure 3 Methodology	11
figure 4 Schedule of the design process	13
figure 5 Lotus 25	14
figure 6 materials used in a Boeing 787	15
figure 7 Icon A5.....	16
figure 8 Reduction of the stress concentration at the joint (Savage, 2010) [6]	16
figure 9 Increasement of the stiffness of a structure using adhesive bonds (SAVA10) [5]	16
figure 10 figure 10 Lightweight battery enclosures.....	17
figure 11 Most frequently used joints (XIAO11) [25].....	20
figure 12 Comparison between the joint strength and the laminate thickness for different joints (XIAO11)[25]	20
figure 13 Sketch of a SLJ with (upper) and without (lower) a preformed angle of 10 degrees (ZHAN07) [28].....	21
figure 14 Epoxy adhesive example.....	22
figure 15 Anaerobic adhesive example.....	23
figure 16 Cyanoacrylate adhesive example	24
figure 17 Peel stress relief achieved by tapering the bonded joint (SAV10a) [6]	26
figure 18 Load distribution curve for different joint lengths (HOSS07) [36]	27
figure 19 Comparison of the stress distribution for different overlap lengths (HOSS07) [36]	27
figure 20 Distribution of shear stress as a function of the normalized overlap length (RAMI18)[37]	28
figure 21 Shear and normal stress distributions in tubular lap joints subjected to tensile load (ADAM74) [25].....	29
figure 22 Stress-strain curves for sheet steel at -40,+20 and +90°C along with the adhesive strain to failure at the corresponding temperatures (GRAN09) [38].....	30
figure 23 Possible loading regimes for bonded joints (SAV10) [6]	31
figure 24 Response of a bond to mechanical load (SAVA10a) [6]	32
figure 25 Forces acting within a bonded joint (SAVA10a) [6]	32
figure 26 Adhesive failure (SAVA10b) [10]	34
figure 27 Cohesive failure (SAVA10b) [10]	34
figure 28 Substrate failure (SAVA10) [10]	35
figure 29 Common defects in bonded joints ((SAVA10) [10]	35
figure 30 Ansys Granta interface	37
figure 31 Tools used for sanding the interior of the CFRP tube	47
figure 32 Grit blasting machine used.....	48

figure 33 End-fitting before (left) and after (right) blasting.....	48
figure 34 Bonding process.....	49
figure 35 Component bonded.....	49
figure 36 Exploded view of EF-4.....	51
figure 37 Aluminum 7075 T6 properties.....	54
figure 38 Aluminum 7075 uniaxial test data.....	54
figure 39 3M Scotch Weld DP420 NS properties.....	55
figure 40 3M Scotch Weld DP420 NS multilinear isotropic hardening data.....	55
figure 41 CFRP tube properties.....	56
figure 42 uniaxial test data.....	56
figure 43 Meshing view of the assembly.....	57
figure 44 Adhesive meshing detail.....	57
figure 45 Force applied in the end-fitting.....	58
figure 46 Carbon fiber fixed face.....	58
figure 47 Suspension case loads for each suspension bar.....	59
figure 48 Maximum loads for each suspension bar.....	59
figure 49 Stress distribution for EF-1-30. Lateral view.....	61
figure 50 Stress distribution for EF-1-30. Isometric view.....	61
figure 51 Stress distribution for EF-1-45. isometric view.....	62
figure 52 Stress distribution for EF-1-45. lateral view.....	62
figure 53 Stress distribution for EF-1-37.5. isometric view.....	63
figure 54 Stress distribution for EF-1-37.5. Lateral view.....	63
figure 55 EF-2-45-0.15 Stress distribution. Lateral view.....	64
figure 56 EF-2-45-0.15 Stress distribution. Isometric view.....	65
figure 57 EF-3-45-0.6. Lateral view.....	65
figure 58 EF-3-45-0.6. Lateral view.....	66
figure 59 Testing assembly modeled in CAD.....	66
figure 60 Stress distribution for EF-4-45. Isometric view.....	67
figure 61 Stress distribution for EF-4-45. Lateral view.....	67
figure 62 Stress distribution for EF-5-45. Isometric view.....	68
figure 63 Stress distribution for EF-5-45. Lateral view.....	68
figure 64 Equivalent Von-Mises Stress variation with the adhesive length.....	69
figure 65 Equivalent Von-Mises Stress variation with the adhesive thickness.....	71
figure 66 Boundary conditions simplification stress distribution.....	72
figure 67 Testing machine used.....	73
figure 68 Testing parameters.....	74
figure 69 Testing machine preparation.....	74
figure 70 First test results.....	75
figure 71 First testing assembly after testing.....	75
figure 72 Second test results.....	76
figure 73 Second testing assembly after testing.....	76
figure 74 Fixed support.....	77

figure 75 Force applied.....	77
figure 76 Simulation correlation with testing.....	77
figure 77 Suspension arm before testing	78
figure 78 Sustainable Development Goals	87
figure 79 Alignment with the Sustainable Development Goals	87

LIST OF SYMBOLS AND ABBREVIATIONS

F1: Formula 1

FS: Formula Student

IFS05: ISC Racing Team prototype of the year 2023

IFS06: ISC Racing Team prototype of the year 2024

CAD: computer assisted design

FEA: finite element analysis

CFD: computational fluid design

CZM: cohesive zone method

SLJs: single lap joint

1. INTRODUCTION

1.1 Formula student

Formula Student is an international motorsport competition that was founded in 1980s. In this competition, team members must be university students, who are in charge of designing and manufacturing a single-seated formula style car which competes in different circuits around the world against other universities. The biggest difference between Formula Student and other motorsport competition is that performance is not the only factor that decides who wins. Race results are decided on a thousand-point scale, where engineer design, performance, business plan and cost reliability of the project are evaluated.



figure 1 Formula Student competition

1.2 ISC Racing Team

ISC Racing Team is the Formula Student team of Universidad Pontificia Comillas (Madrid, Spain), established in 2017. The first ever prototype of the team's history, the IFS01, was manufactured in 2018, marking the beginning of a series of developments that led to the creation of four additional cars ever since. In 2023, the team unveiled the IFS05, which is shown in figure 2.

I joined the team in 2022, and during the season of 2023-2024 I have been in charge of the chassis and composites departments.

The car's suspension system includes carbon fiber tubes bonded with metal end-fittings. The team has strategic plans to incorporate more composite materials into the next cars. This initiative aims to reduce the car's weight and enhance its overall performance. Further research needs to be done in adhesive joints to ensure weight reduction without compromising safety standards.



figure 2 IFS 02 (left) and IFS 05 (right)

1.3 Aim of this project

The aim of this project is to improve the composite-metal interfaces of the suspension of the IFS06, reducing its weight without compromising safety.

1.4 Objective

- Produce a complete manual that can be used in the future to design and manufacture adhesive joints between composite and metal.
- Reduce the mass of the current design without compromising safety standards.
- Study the different materials that can be used.
- Ensure the structural reliability of the joining through structural analysis and testing.
- Develop a simulation model that correlates with realistic adhesive behavior

1.5 Motivation

My main motivation is to enhance the performance of the ISC car. Ensuring the continuity of the team over the following years is crucial for this team success. The most effective approach over the years has been transferring knowledge from one generation to the next. Additionally, the study of composites will play a key role in elevating the overall performance of the car.

I truly want to learn and have an impact in the motorsport industry. This project will help me to introduce me into the world of adhesives, finite element analysis, and computer assisted design. Furthermore, being able to have a Formula 1 engineer as my director will allow me to learn a lot.

1.5 Methodology

The methodology used in the motorsport industry today relies heavily on simulation due to the high cost and long time periods required to physically testing. FEA primarily helps to achieve faster the optimization of the design (mechanical properties, weight etc.) and reduce manufacturing and testing costs.

The methodology that will be followed is presented in figure 3. The project is divided into three phases.

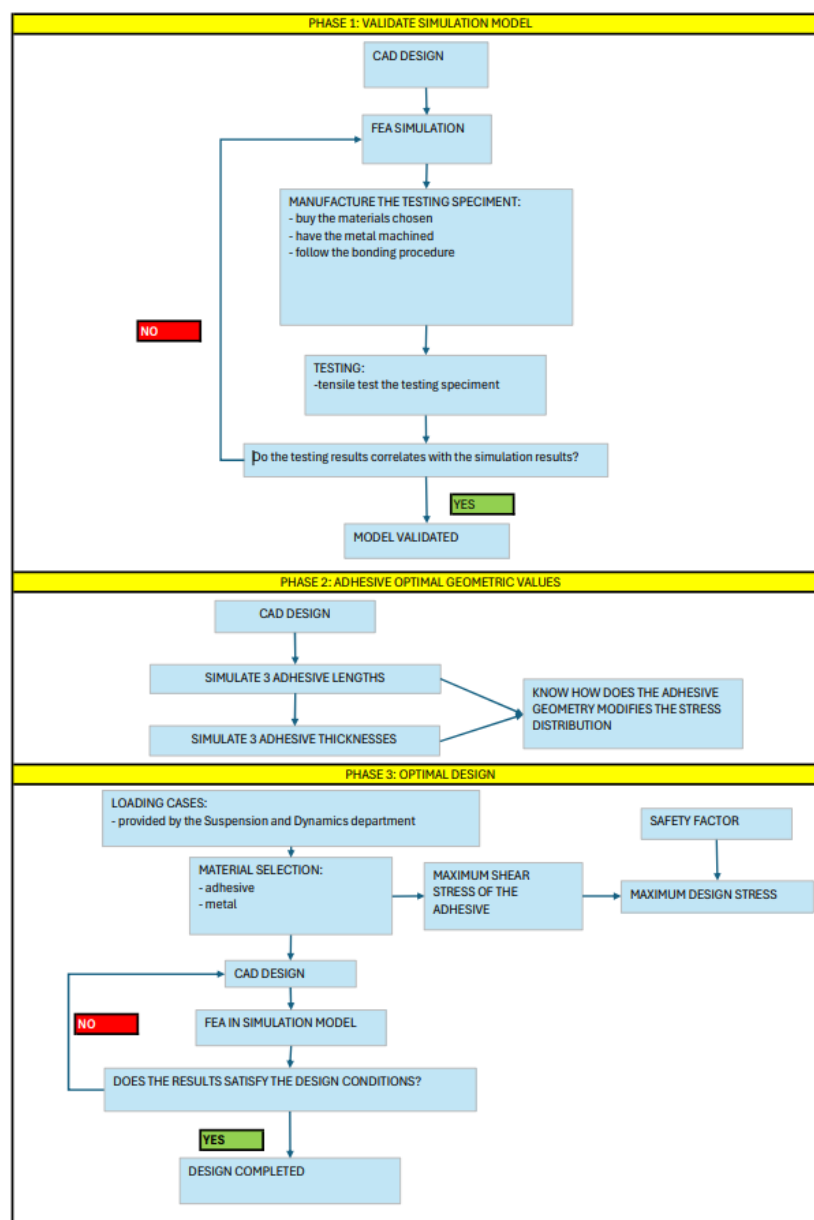


figure 3 Methodology

Phase 1

Firstly, a simulation model will be developed. This model will be validated through testing. This phase includes the CAD design of the suspension arm, followed by the development of the FEA simulation model. In parallel, the designed suspension arm will be manufactured and tested using a tensile testing machine. If the testing results correlate with the simulation results with an accuracy superior to 90% the model can be considered accurate and validated.

Phase 2

Secondly, the project involves the investigation of the influence of variations in adhesive geometric parameters on stress distribution within adhesive. The study will analyze the influence of two parameters, each with three simulations. The aim is to determine how much does the variation of these parameters influence the stress distribution, enabling the selection of optimal values for the adhesive.

Finally, with the simulation model validated and the optimal values of the adhesive geometric parameters, an optimal end fitting design is presented.

Phase 3

Firstly, the Suspension and Dynamics department of ISC Racing Team will provide the loading cases for each suspension arm. The maximum value of all the cases for all the suspension arms will be selected as the maximum tensile force for the design.

Secondly, the materials for the adherents and the adhesive selection will be chosen based on the mechanical properties considered for this design. Ansys Granta Edupack will be used to select the adherents. This software contains a database with thousands of materials that can be filtered and compared. A safety factor will be applied to the maximum shear stress of the adhesive, achieving the maximum shear stress of the design.

Following, the end-fitting will be designed using the CAD software Solidworks 2023. The end-fitting design used for testing requires a M6 hole for the pin required to adapt the end-fitting to the testing machine. Even though the testing end-fitting does not have the same design as the end-fitting that is installed in the car, the difference in the design do not change the simulation results and the conclusions from the simulations done can be used for further projects.

The scheduled proposed for this design is presented in figure 4. The project is divided into four different stages. Firstly, bibliography about the use of adhesive joints in Motorsport will be searched during the first month of the project. Stage two corresponds to the research about bibliography on suspension joint geometries, suspension joints materials, common practices in the adhesion of this components and what type of testing should be done to validate the simulations. This research will be done during the month of November.

Stage three will be done in December, in which CAD and FEA training will be done in order to be able to simulate. This stage will start with theoretical FEA knowledge, continuing with basic FEA exercises. This phase will continue with advanced FEA exercises.

The design stage will be done from January to July, starting with the decision on the prototype characteristics, such as the adherents and adhesive that will be used. Continuing with the CAD design and the FEA analysis. At last, the testing pieces will be manufactured and tested. Once the simulation model is validated with the tests results a final design for the end-fitting is presented.

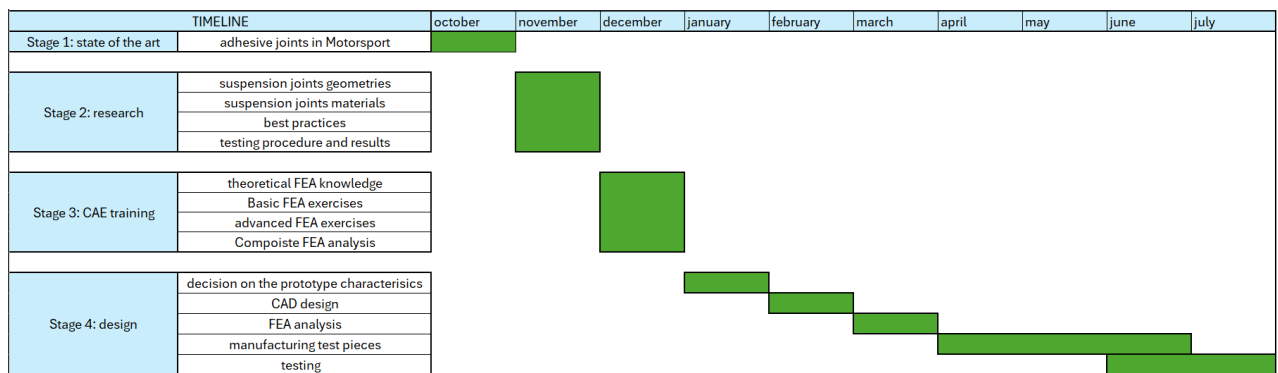


figure 4 Schedule of the design process

1.6 Resources to use

For developing this project, the following resources will be required.

- SolidWorks will be chosen as CAD software and Ansys 19 as FEA software.
- Materials such as carbon fiber or adhesives bought by ISC Racing Team.
- Tensile testing machine provided by ICAI.

The licenses required for using SolidWorks and Ansys 19 will be provided by ISC Racing Team.

1.7 History of composites in formula 1

"Adding power makes you faster on the straights, subtracting weight makes you faster everywhere." - Colin Chapman

The secret to achieving the fastest car lies in these words of the Team Lotus founder, Colin Chapman. The motorsport industry revolves around the endless pursuit of minimizing a racecar's weight. Throughout motorsport's history, cutting-edge technologies have played a critical role in crafting lighter racecars. One such technology is topology optimization, employed in motorsport to improve race car performance, in which weight is reduced while ensuring structural integrity. However, the most influential developments have emerged from the domain of materials research.

Adhesive joints have been used in motorsport for several decades. The motorsport industry has evolved over time, and adhesive technology has advanced alongside it.

When F1 was founded in 1950, cars had an aluminum space frame with aluminum body panels. The use of composites in F1 is traced to a decade later, with the creation of the Lotus 25 F1 car, designed by Colin Chapman and introduced in 1962. The Lotus 25, shown in figure 5, featured a monocoque chassis made of aluminum and fiberglass body panels, representing a departure from the traditional space frame construction. This design contributed to weight reduction and improved performance (PARK24) [1].



figure 5 Lotus 25

Adhesive bonding and composite materials started to gain traction in motorsport in the latter half of the 1970s. F1 has been pioneer in the adoption of advanced materials and construction techniques. It is in the late 20th century and into the 21st century that adhesive bonding has become more popular in various motorsport applications, including bonding carbon fiber composite panels and chassis components.

Today, adhesive joints are commonly used in motorsport for various applications, and they continue to play a significant role in enhancing the performance and safety of racing vehicles. 80% of a F1 car is made from composites structures, such as the carbon fiber monocoque chassis or the suspension members. The assembly of many of the multi-material structures which make up a Formula 1 racing car is dominated by adhesives (SKUS23) [2].

New material joining techniques have been developed in recent years for joining lightweight materials that are hard to weld or dissimilar. Adhesive joining has been the most common joining method in the recent years and the adhesive bonding science has progressed significantly. To give numbers outside the motorsport industry, the Boeing 787, shown in figure 6, and the airbus A350 contain more than 50% of bonded structure (MEMO23) [3].

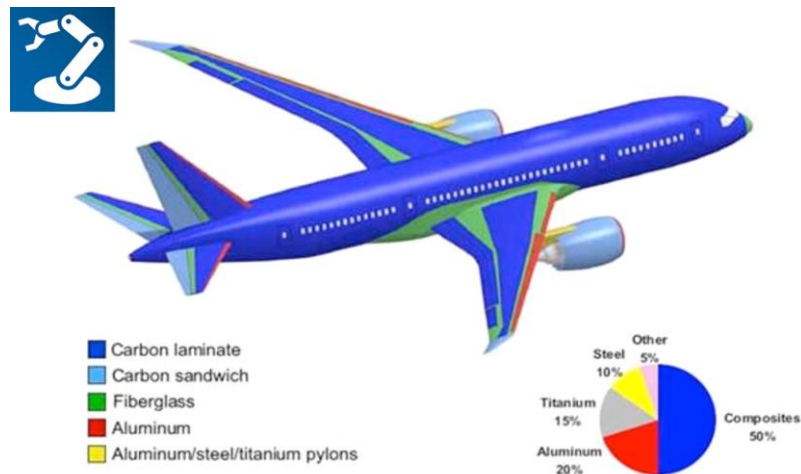


figure 6 materials used in a Boeing 787

More examples can be found in this industry. figure 7 illustrates the Icon A5, an amphibious aircraft with wave-cutter fuselage made of carbon fiber with components adhesively bonded (ICON23) [4].



figure 7 Icon A5

The increase of the use of adhesive bonding compared to more traditional methods such as bolting is due to its advantages, such as high fatigue resistance, lower stress concentration effects and good damping characteristics. As it can be seen in figure 8, the stress concentration at the joint when bonding is reduced compared to other techniques, such as using bolts, avoiding local stress concentrations.

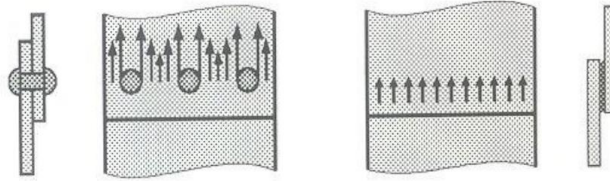


figure 8 Reduction of the stress concentration at the joint (Savage, 2010) [6]

The bond formed is continuous, and the unstiffened area is reduced when comparing with bolting joints, creating stronger and stiffer structures, as it is shown in figure 9.

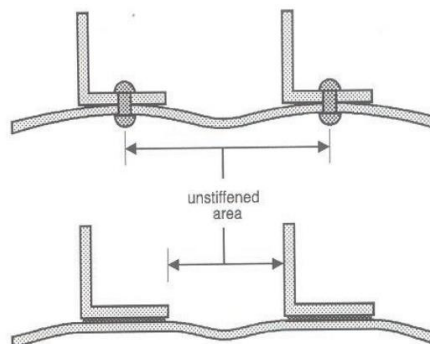


figure 9 Increase of the stiffness of a structure using adhesive bonds (SAVA10) [5]

1.8 Literature review

Even though composite materials have been used in motorsport for decades, there is not much information about it. This is because sharing the team's knowledge can end in the competitors hands. However, composite materials have been used in aerospace since the first world war and there is much information about composites in this industry. Composite materials are not often used in the automotive industry due to its expensive cost and its difficulty to produce in mass. Some examples can be found in the automotive industry, major industry leaders, such as BMW, are starting to use composite materials in their battery modules to improve structural performance while reducing weight. Another great example is the British company TRB lightweight structures, that achieved a reduction of their battery modules weight of 87.5% using composites (FAB23) [6]. figure 10 presents a battery enclosure made from continuous fiber-reinforcement thermoplastics (FARI21) [7].

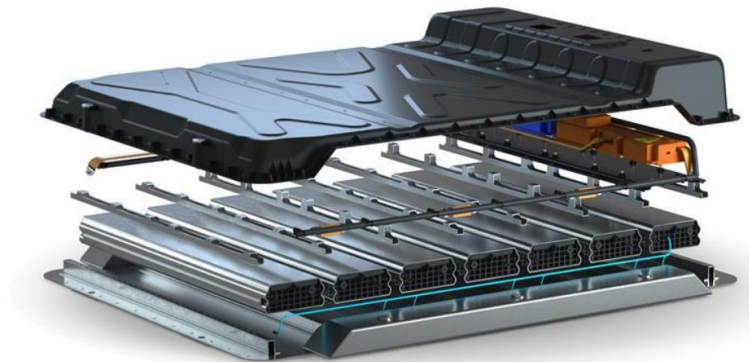


figure 10 figure 10 Lightweight battery enclosures

Most of the knowledge of adhesive bonding in formula-type cars comes from the work of Gary Savage. In “Formula 1 Composites Engineering” (SAVA10a) [5], the historical evolution of composite structures and their development in Formula 1 is reviewed, providing insights into the design and manufacturing processes. In “Failure prevention in bonded joints on primary load bearing structures” (SAVA07) [8], Savage does a complete research on adhesive bonding and failures prevention on joints. The importance of bonding components with adhesives is reviewed in “dealing with crisis-solving engineering failures in Formula 1 motor racing” (SAVA10b) [9], where the author arguments that adhesive joints show superior performance than other bonding methods. It is also reviewed the importance of the quality of the production process to ensure the long term durability of the bonding.

In the paper “A review of failure theories and simulation models for adhesive joints” (TSER22) [10], the authors review failures theories and models for adhesive joints.

Albiez et al. (ALBI19) [11] experimentally studied the influence of varying geometrical factors on the tensile strength of tubular joints. It was concluded that the joint strength increase with the increase of the overlap length nonlinearly. The results indicated that an increase in the adhesive layer thickness affects negatively the joint strength.

Nguyen and Kedward (KEDW01) [12] developed an analytical model to assess the τ_{xy} stress in a tubular adhesive joint under tension. The results showed that the joints with a 10° chamfer in the adherent had a more uniform stress distribution and a lower stress value compared to without chamfer.

Some research has been done with experimental investigations. In “Evaluation of Bonding Gap Control Methods for an Epoxy Adhesive Joint of Carbon Fiber Tubes and Aluminum Alloy Inserts” (RAZD21) [13], the authors compare two methods for controlling epoxy adhesive bond in carbon fiber composite tubes and aluminum alloy inserts used in a motorsport vehicle’s suspension system. The study contrast a geometrical solution with a method that involves glass beads mixed with epoxy adhesive. More can be found in the work of de Queiroz et al. (QUEI21) [14], where single-lap adhesively bonded joints are experimentally explored using different fiber-reinforced polymer composites.

Information about adhesive joints in Formula Student cars can be found. Papers such as “análisis comparativo de configuraciones de suspensión para un monoplaza tipo FSAE”, (MEL19) [15] and “composite wishbone for FS” (GRAN17) [16], are of great importance for this project and for FS future generations. In these papers, authors design a complete suspension for a FS car. More about adhesive joints in FS can be found in the work of Saman Fanni and Fadi Jweda in “design of carbon fiber composite driveshaft end fittings and adhesive joints for motorsport applications”, (FANN16) [17] and in the work of Antonio Hernández-Ros in “Design and manufacture of a Formula Student suspension (ANTO22) [18].

More information can be found for CAD and FEA, papers such as “a review of finite element analysis of adhesively bonded joints”, (HE21) [19] and “numerical analysis of geometrical modification combinations of the tensile strength of tubular adhesive joints” (ROSA21) [20] are of great relevance. In Rosas et al. work, different geometric changes, such as outer chamfers, inner chamfers and adhesive fillets at overlap ends are numerically analyzed, along with the combined effect of inner chamfers and adhesive fillets.

2. BONDED JOINTS

2.1 Bonded joints introduction

Since 1930, extensive research have been performed to improve the understanding of bonded joints and explore ways to optimize the adhesive-adherent interface. In Volkersen's shear-lag analysis (VOLK38) [21] it was demonstrated that the adhesive deforms in shear while the adherent deforms in tension. Goland and Reissner (GOLA44) [22] were the first to take into account the consequences of the rotation of the adherents, they evaluated the shearing and normal stresses in the bond layer taking into account that the peel and shear stresses were constants across the adhesive thickness.

Hart-smith's method (HART73) [23] is an evolution of Volkersen's shear lag analysis and Goland's and Reissner's theories. The conclusion of his work is that the adhesive should not be the weak link and if peel stresses are likely to occur they should be alleviated by scarfing the adherends or by locally thickening the adhesive layer.

The major factors determining the integrity of an adhesive bond are shown in this section.

2.2 Bonded joints geometries

Throughout the years, new bonded joint geometries have been put into practice. The most common configuration is the single lap joint. The main advantage of this geometry is that it is simple to manufacture and convenient for testing. This geometry loads the adhesive mainly in shear stress. Moreover, the bending moment caused by the non-collinear adherents generates peel stresses (σ_y) at the overlap edges. Also, the shear-lag effect generates τ_{xy} peak stresses (ADAM96) [24].

Many other types of joints, such as doble strap joint, double lap joint or tapered lap joint are often used to decrease the peel stresses, as shown in figure 11.

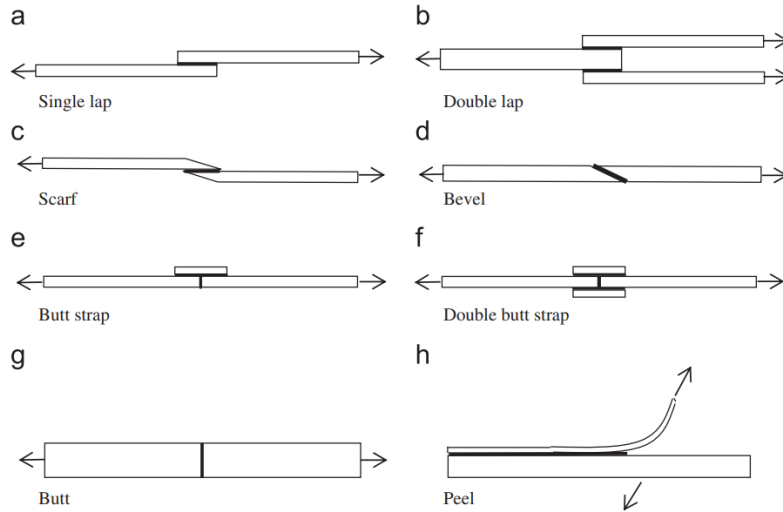


figure 11 Most frequently used joints (XIAO11) [25]

The joint strength depends of the type on joint used. In figure 12 it is shown how the joint strength changes with the laminate thickness and the type of joint used.

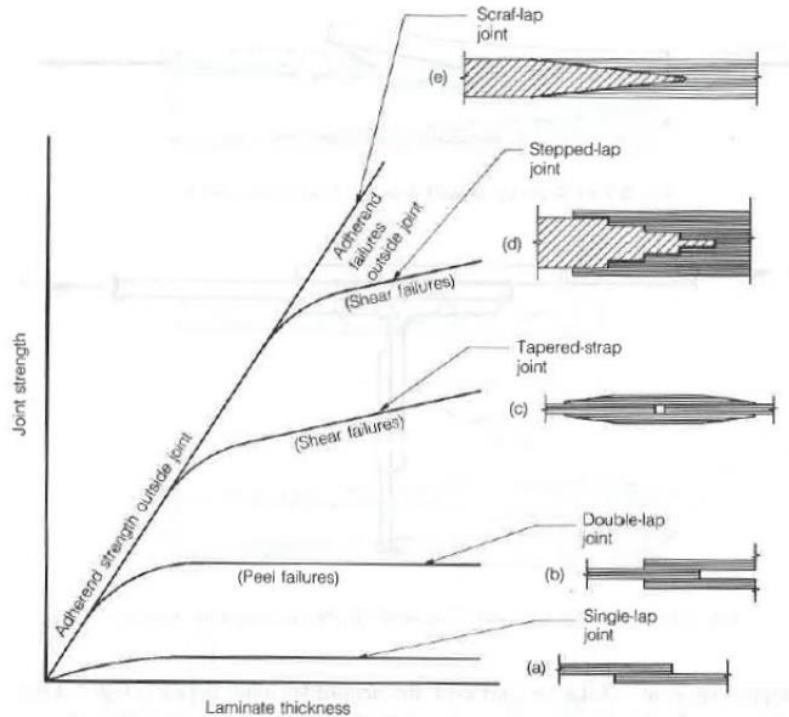


figure 12 Comparison between the joint strength and the laminate thickness for different joints (XIAO11)[25]

2.2.1 Single lap joint (SLJ)

Even though it is a simple geometry, the lap joint problem is three dimensional. The stress behavior of the SLJs is complex due to the bending induced during deformation. A general two dimensional theoretical approach was developed by Zhao and Lu (ZHAO09) [26], proving an explicit closed form solution for calculating elastic stresses in SLJs. The elasticity theory used includes the complete strain-displacement relationship for the adhesive and adherent. The investigation considered various parameters such as the overlap length, the bond line thickness and the spew fillet. One significant finding was that three point bending and tension loading exhibit similar effects on the adhesive, while the four point bending test does not lead to failure because the steel yields before the joints fails.

You et al. (YOU07) [27] investigated the impact of a preformed angle on stress distribution in the mid bond line and the ultimate load of adhesively bonded steel SLJs. Numerical simulations revealed that all the peak stresses in the mid bond line of the adhesively bonded SLJ were reduced as the preformed deflection angle increased from 0 to 15 degrees. figure 13 illustrates the sketches for the SLJ designs with and without a preformed angle of ten degrees.

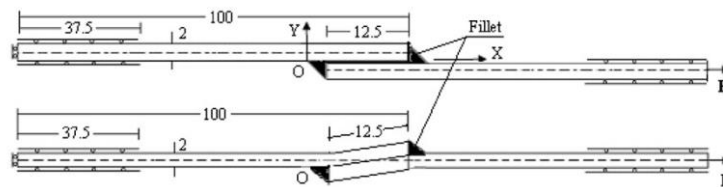


figure 13 Sketch of a SLJ with (upper) and without (lower) a preformed angle of 10 degrees (ZHAN07) [28]

2.3 Methods to predict properties

The initial methods used to predict the adhesive bonding properties began with analytical methods, such as Volkersen's method (VOLK38) [21], which used closed form expressions, overlooking material and geometry details. These methods were unrealistic when more complicated geometries were analyzed.

Finite element methods were introduced in 1974 by Adams and Peppiatt (ADAM74) [29] with a method used for predicting the behavior of adhesive joints requiring only the knowledge of the stress distribution and the use of an adequate failure criterion.

Nowadays, the most popular method is the cohesive zone model (CZM) (CAMP12) [30]. This method relies on fracture properties and allows to model bonded joints that experience high stress variations. The precision of this method depends on the accuracy of the values of cohesive strength in tension and shear.

2.4 Types of adhesives

Choosing the right adhesive depends on the specific requirements of the applications. Properties such as strength, flexibility, chemical resistance and temperature stability must be considered. In this section, the most prevalent adhesives are explained.

2.4.1 Structural epoxy adhesives

This adhesive is known for forming very strong bonds across a wide range of materials, making them suitable for applications where high bond strength is crucial for structural integrity. Structural epoxy adhesives are widely used for joining metal-to-metal and metal-to-polymer structures due to their notable characteristics. They are available in different forms, including one and two-part thixotropic pastes and films. This versatility allows for their use in various applications, accommodating different bonding requirements.

One part adhesives are useful in assembly lines. The main advantage of this adhesive is that it is easier to work with because there is no mixing involved. However, the main drawback is that this adhesive requires a heat treatment for curing properly.

In contrast, some two-part epoxy adhesives can be cured at room temperature, offering convenience in certain applications. The durability of epoxy adhesives at elevated temperatures is generally better when cured at higher temperatures. This adhesive requires the user to mix a resin with a hardener that triggers the polymerization required for curing. When both components are mixed, an exothermic reaction occurs as the molecules begin to cross-link. It's essential to note that increased curing temperatures may potentially lead to low-temperature brittleness, highlighting a trade-off between elevated temperature performance and low-temperature characteristics.

While epoxies offer high shear strength, they have low peel strengths, which can be up to two orders of magnitude lower than their shear strength. This means that they may not perform as well under tensile or peeling stresses compared to shear stresses.



figure 14 Epoxy adhesive example

2.4.2 Anaerobic adhesives

Anaerobic adhesives are single-component materials which cure at room temperature when they are isolated from contact with oxygen.

The low viscosity of the liquid adhesive facilitates capillary action, enabling it to fill gaps in the joint effectively. Anaerobic adhesives are commonly known as "locking compounds" because they are frequently employed to secure and seal fitting parts. These adhesives are formulated based on synthetic acrylic resins, characterized by their high shear strength, as well as good solvent resistance. The ability to cure in the absence of oxygen makes anaerobic adhesives particularly useful in applications where a secure and fast bond is needed, especially in threaded assemblies.



figure 15 Anaerobic adhesive example

2.4.3 Cyanoacrylates adhesives

Cyanoacrylate adhesives, commonly known as "super glues," have a unique curing process by reacting with the alkalinity present in moisture on the bonding surfaces. These adhesives are characterized by limited gap-filling ability, requiring close-fitting joints for optimal performance. The curing time typically takes only a few seconds. This quick action is particularly valuable for bonding parts without the need for complex jigs and fixtures.

While the bonds formed by cyanoacrylate adhesives may not be as strong as those created by epoxies, they are particularly suited to small polymeric components and elastomers. The versatility of these adhesives is reflected in the wide range of products offered by various manufacturers, each tailored with subtle variations for specific needs. This includes adjustments in viscosity to aid in processability and formulations containing rubbers and/or polyurethanes to enhance toughness.



figure 16 Cyanoacrylate adhesive example

2.5 Bonding preparation

The surfaces to be bonded must be prepared to ensure proper adhesion. Surface preparation in adhesive bonding serves the primary objective of removing weak boundary layers that can compromise the quality of the bond. For metal substrates, a common challenge is the presence of a weak and contaminated oxide "scale," needing its removal before bonding. Similarly, polymeric materials may contain plasticizers that can migrate to the surface, while the processing of composite structures introduces issues related to mold release agents. Other contaminants such as dust, dirt, grease, and oils further emphasize the importance of surface cleaning. Additionally, surface pre-treatment aims to optimize the contact between the adhesive and substrates.

This optimization can be achieved through mechanical means, increasing the effective bonding area by enhancing the roughness of the substrate surfaces. Mechanical abrasion methods such as grit blasting eliminate weak surface layers and enhance the bond area by improving substrate texture.

Chemical treatments, like etching and anodizing, promote bonding mechanisms. The use of primers and activators enhances these mechanisms and can modify the adhesive's cure kinetics. Chemical modification of the substrate's surface layers can also be employed to improve the interaction between the adhesive and the substrate.

Pereira et al. (PERE10) [31] studied the impact of manufacturing parameters on the strength of adhesively bonded SLJs with the objective of optimizing surface treatment processes, specifically using sodium dichromate sulphuric acid etch (CSA) and abrasive polishing (AP), showing the improvement of the joint shear strength when compared to acetone cleaning (SW), caustic etch (CE) and Tuckers reagent etch (TR).

2.6 Effects of geometry modifications

The design of the joint influences the distribution of stress within the bond. You et al. (YOU19) [32] investigated the influence of the adhesive gap on the stress distribution in both the mid bond line and the adherent near the interface along the lap zone of adhesively bonded double lap joints. The FEA simulation results indicated that the influence of the gap length on the ultimate load of the joint was minimal, even as the gap length was increased.

In the experimental study conducted by Ki Soo Kim et al. (KIM92) [33], the fatigue and static strength of various joint configurations, including single lap joints, single lap joints with scarf, double lap joints, and double lap joints with scarf, were tested. Additionally, the stresses in these joints were simulated to gain insights into their performance. The study's conclusion indicated that the double lap joint had a significantly higher load-bearing capacity compared to the single lap joint. The researchers found that tapering the composite adherend, a common practice to enhance joints, did not provide benefits in this particular context. This suggests that the double lap joint configuration without tapering, was more effective in terms of load-bearing capacity than the SLJ with tapering.

Won Tae Kim and Dai Gil Lee (WONT17) [34] studied the strengths of various shapes, including hexagonal and elliptical, and compared them to the conventional circular form. The comparison involved single lap and double lap joints. The researchers found that the double lap joint had higher strength than the single lap joint, due to its larger bonding area. Notably, the outer adherend of the double lap joint was identified as effective in preventing bulging of the tube caused by hoop stresses. Furthermore, the study concluded that among all the single lap joints, the hexagonal shape demonstrated the highest strength.

2.6.1 Adhesive thickness

The thickness of the adhesive layer plays a critical role in the effectiveness of a bonded joint. If the adhesive layer is too thin, it can result in poor adhesion due to non-uniform wetting, creating stress concentrations in the joint. This stress can induce a bending moment, causing the joint to rotate and increasing the peel component, which can compromise the integrity of the bond. On the other hand, an excessively thick adhesive layer is impractical as it is challenging to execute without introducing intolerable levels of flaws and porosity.

Stress gradients occur through the adhesive thickness. In the work of Philip J. and in the work of Sancaktar et al. this gradient is analyzed (HIPO84) [34] (SANC03) [35].

2.6.2 Tapering the adhesive

The taper refers to the gradual reduction of thickness or thickness along the surface of the adhesive. The purpose of tapering is to relieve stress concentration, especially in adhesive joints where uneven stress distribution can lead to issues like peeling or joint rotation. In figure 17 it is shown the peel stress relief achieved by tapering the bonded joint.

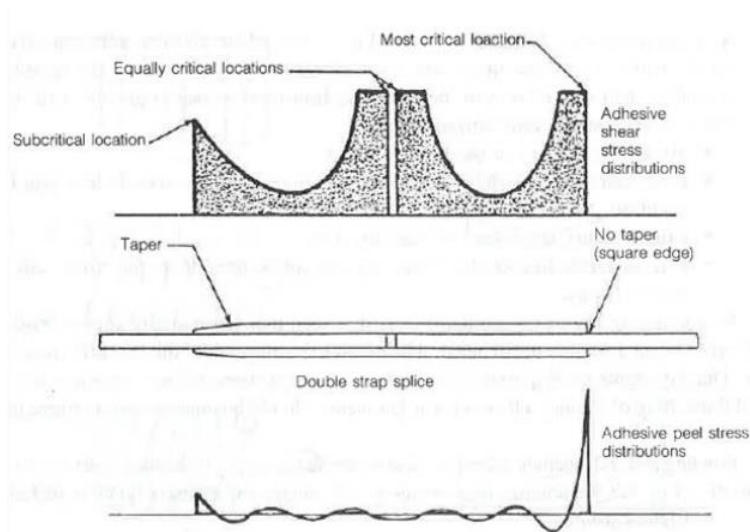


figure 17 Peel stress relief achieved by tapering the bonded joint (SAV10a) [6]

To calculate the optimum taper for a bonded component, the equation shown in equation 1 is applied.

$$taper\ angle = \tan^{-1} \left(\frac{2 + l}{t_1 - 1} \right)$$

equation 1 Taper angle formula

Where t_1 is the laminate thickness and l is the bonding length (all dimensions in mm)

2.6.3 Bond overlap

Short bond overlaps are more efficient than longer ones. In the work of Hosseinzadeh et al. (HOSS07) [36] the stress distribution for different overlap lengths was studied. The results of this work are present in and in figure 18 and in figure 19.

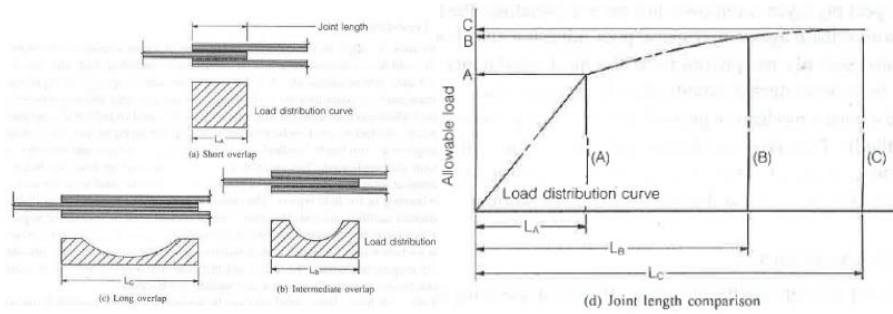


figure 18 Load distribution curve for different joint lengths (HOSS07) [36]

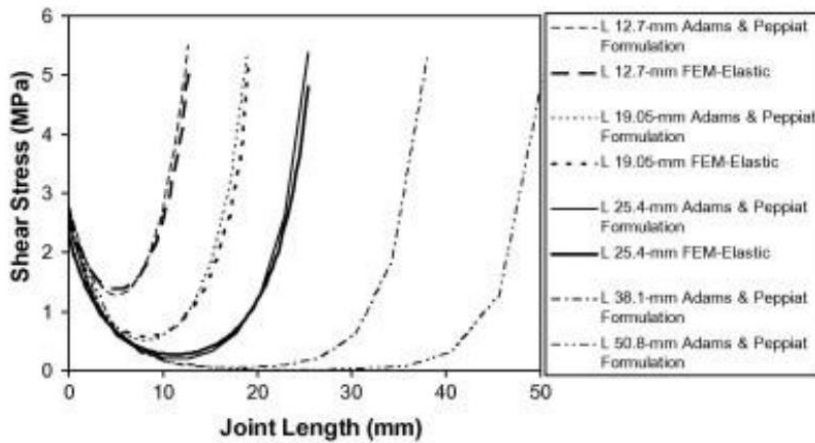


figure 19 Comparison of the stress distribution for different overlap lengths (HOSS07) [36]

In the work of the National Physical Laboratory (MANU07) [37] it was shown that increasing the thickness of the joint will increase the joint strength proportionally, but increasing the joint length will not always increase the joint strength.

The effective length is the distance that maximizes the joint strength per unit of distance. Increasing the joint length will result in increasing the joint strength if the joint length is lower than the effective length. If the joint length is higher, the joint strength remains constant. This is the consequence of the stress concentration at the overlap length. In the work of Ramin et al. (RAMI18) [37] it was shown that increasing the overlap length created a stress free area in the middle of the overlap and the stressed area remained constant. In figure 20 the distribution of shear stress as a function of the normalized overlap length is shown.

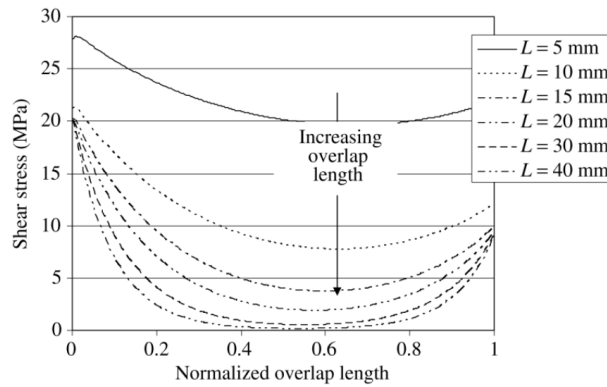


Figure 6 - Distribution of shear stress as a function of normalized overlap length. [13]

figure 20 Distribution of shear stress as a function of the normalized overlap length (RAMI18)[37]

2.6.4 Overlap stress distribution

The overlap stress distribution refers to the pattern of shear stresses along the length of the overlap region. Numerous analytical and experimental studies have revealed that this distribution exhibits peaks at the ends of the overlap. The stress peaks and the stress distribution are similar for tension and torsion load cases. Despite the differences in stress types, the stress distribution remain comparable between tension and torsion loading scenarios, indicating similar behavior in terms of shear stress distribution along the overlap length.

Maximizing the area over which the load is distributed is essential for optimizing the joint's strength. A larger bonding surface helps distribute the load more uniformly, reducing the risk of localized stress concentrations.

In Adams and Peppiat's work (ADAM74) [25], stress distribution for tensional and torsional load cases were studied. The results of this work are shown in figure 21. The same stress distribution curve is found for both loading cases, except that the torsional case have higher stresses at the ends of the lap joint.

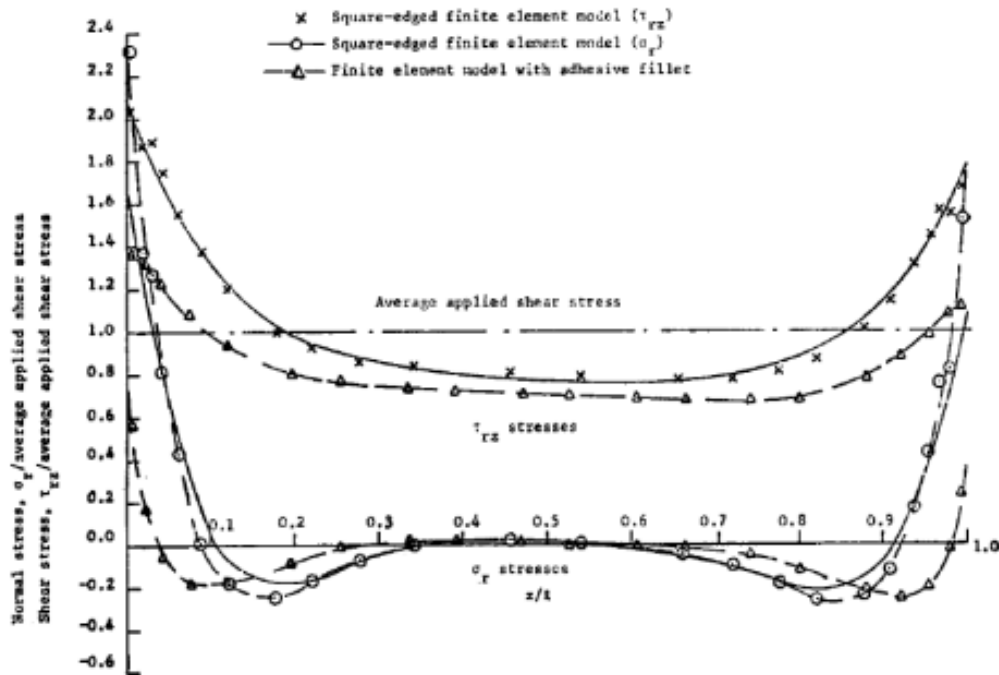


figure 21 Shear and normal stress distributions in tubular lap joints subjected to tensile load (ADAM74) [25]

2.7 Effect of environmental conditions

Structural adhesives are usually thermoset materials, which will be affected by environmental conditions and exhibit time dependent characteristics. Environmental parameters, such as temperature, humidity and exposure to various substances can contribute to changes in the adhesive properties over time.

2.7.1 Temperature effects

Grand et al. (GRAN09) [38] developed some experiments and FEA analysis to evaluate the impact of temperature variations in joints. Test were conducted at -40°C , 20°C and 90°C . Figure 22 shows the stress-strain curves for sheet steel along with the adhesive strain to failure at the corresponding temperatures. It was demonstrated that the failure criterion proposed at room temperature remains valid at both low and high temperatures. It was also observed that the failure envelope shifts upwards and downwards as the temperature increases or decreases, respectively.

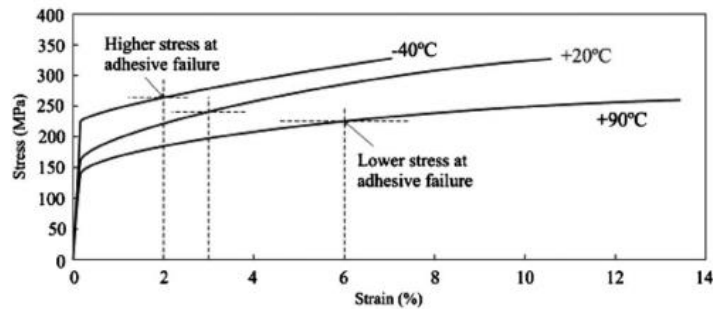


figure 22 Stress-strain curves for sheet steel at -40,+20 and +90°C along with the adhesive strain to failure at the corresponding temperatures (GRAN09) [38]

2.6.2 Humidity effects

It has been observed that the strength of adhesive joints decreases over time when exposed to a humid environment. The presence of water impacts both the chemical and physical characteristics of adhesives, as well as the nature of the interfaces between the adhesive and adherends.

Liljedahl et al. (LILJ06) [39] explored the use of CZM to predict long term durability of adhesively bonded joints exposed to humid environments. Joints were subjected to high relative humidity conditions and immersed in both tap and deionized water for a year before being tested until failure. The cohesive zone parameters determined the residual strength of the joint. In the model, the degradation of these parameters was directly linked to the concentration of moisture, highlighting the influence of environmental exposure on the long term performance of adhesively bonded joints.

2.8 FEA analysis

The FEA analysis offers a significant benefit allowing the determination of mechanical properties in an adhesively bonded joint with nearly any geometrical shape under different load conditions. When applying FEA to adhesively bonded joints is important to accommodate the meshing to both the small dimension of the adhesive layer and the larger dimension of the adherent. Furthermore, failures of adhesively bonded joints typically occur within the adhesive layer. Therefore, it becomes essential to model the adhesive layer by a finite element mesh several orders of magnitude more refined in a very small region than in the rest of the joint.

In order to save computer time, it is important to build the finite element model with a limited number of elements and nodes, simplifying the model.

The work by Adams (ADAM74) [25] is considered as seminal work in the area of FEA, leading to the development of FEA in adhesive bonding. In his work, the FEA for different adhesively bonded joints, such as lap joints, tubular lap joints, butt joints, bevel and scarf joints, were analyzed. The author also introduced non-linear FEA into adhesive bonding.

2.9 Loading regimes

The properties of adhesives dictate that their mechanical response to compression and shear loading regimes is typically much better than their response to tensile loading. The adhesives tend to exhibit superior performance in compression and shear compared to tensile strength. The peel and cleavage strengths of an adhesive can be notably lower, sometimes up to two orders of magnitude than its shear strength. Therefore, it is important to avoid subjecting adhesives to tensile loading whenever possible. Figure 23 illustrates the most common loading regimes.

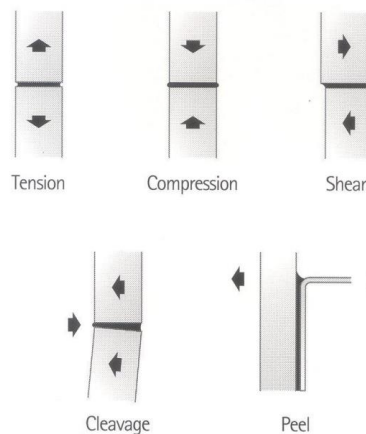


figure 23 Possible loading regimes for bonded joints (SAV10) [6]

The strength and durability of a joint is a complex function of the stress concentrations set up by the applied loads and operating conditions. In a SLJ the shear stress varies along the length of the joint with peak concentrations at the ends. In contrast, the peel stress acts at right angles to the lap joint and is also maximized at the ends. The peel stress tends to distort the joint and weaken it. Similarly, any deflections of the structure under load increase the peel component and may lead to premature failure. Unsupported lap joints are one of the weakest configurations and are rarely used. Figure 24 shows the response of a bond to mechanical loads.

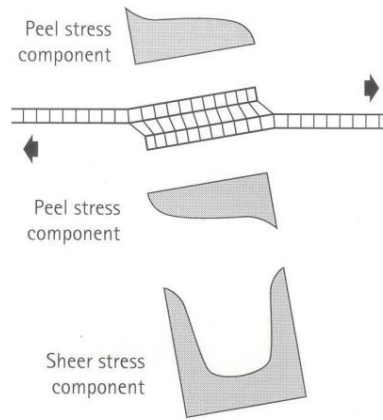


figure 24 Response of a bond to mechanical load (SAVA10a) [6]

The adhesive strength refers to the force required to cleanly separate the adhesive from the surface of the adherend. It is a measure of the bond's resistance to tensile stress without failure. Adhesive strength is a critical parameter in determining the effectiveness of an adhesive in creating a durable and reliable bond between materials. High adhesive strength is desirable in applications where the bonded components experience tensile loading or forces pulling them apart. Figure 25 shows the forces that act within a bonded joint.

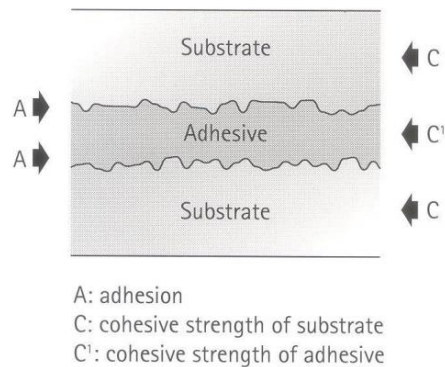


figure 25 Forces acting within a bonded joint (SAVA10a) [6]

2.9.1 Fatigue loading analysis

Fatigue loading is a frequent cause of failure in adhesively bonded joints. Under the presence of fatigue loading, the adhesives exhibits a lower resistance to crack growth compared to under monotonic loading conditions. Most studies neglect initiation and focus upon growth of cracks of microscopic proportions, which determines the life of the component. Experimental evidence suggests that applying a design safety factor of 3 (or more) to a joint will eliminate purely mechanical fatigue problems and the bond will be “inherently safe” (SAVA10a) [6].

Jen and Ko studied the effect of bonding dimensions on fatigue strength (JEN10) [40]. FEA was used to determine the local stress states at the interface between the adhesive and the adherend to gain insights into how the bonding dimensions influenced the fatigue performance of adhesively bonded joints. The study focused on three parameters, the maximum interfacial peeling, the maximum interfacial shear stress and a linear combination of interfacial peeling stress and shear stress. The study showed the correlation between these parameters and the fatigue life data, providing valuable information for optimizing the design of such bonding.

2.10 Types of failure

2.10.1 Adhesive failure

In the worst case scenario the adhesive is observed to be completely separated from the face of one substrate, which means that the weakest aspect of the joint is the boundary layer between the bonded parts and the adhesive. The joint is prone to sudden failure, occurring at a load much lower than predicted. The causes of such failure can typically be attributed to either the unsuitability of the adhesive material for bonding or incorrect surface preparation due to contamination (SAVA10b) [10]. An example of adhesive failure is presented in figure 26.



figure 26 Adhesive failure (SAVA10b) [10]

2.10.2 Cohesive failure

In this type of failure the adhesive itself breaks. The failure is characterized by remains of the adhesive being found on both substrates. This type of failure occurs when the adhesive is subjected to excessive stress from external actions such as temperature, ageing or off axis loading due to misalignment or deflection. An example of cohesive failure is presented in figure 27.



figure 27 Cohesive failure (SAVA10b) [10]

2.10.3 Substrate failure

The preferred failure mode in adhesive joints is substrate failure. The bond is not the life-limiting factor of the joint, and it should not significantly influence its long-term durability. It is recommended to design all stressed joints in a way that ensures ultimate failure occurs in the substrate rather than the adhesive bond. This approach allows for a more predictable and controllable failure mechanism, facilitating easier maintenance or repair and ensuring that the overall structural integrity is maintained over the long term. By designing for substrate failure, the joint can be engineered to maximize its service life and reliability. Figure 28 shows an example of substrate failure and figure 29 illustrates the most common defects in bonded joints, such as void and porosity.



figure 28 Substrate failure (SAVA10) [10]

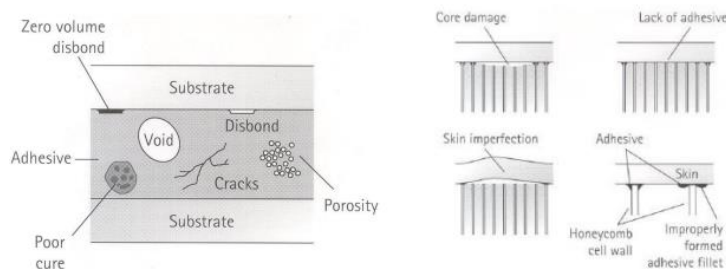


figure 29 Common defects in bonded joints ((SAVA10) [10])

3. MATERIAL SELECTION

This chapter illustrates the process followed for the material selection using the software Ansys Granta EduPack, which is a set of teaching resources to support materials education. This software incorporates thousands of materials datasheets and facilitates the generation of graphical representations based on material properties. The data and tools are divided into three levels, being level three the one with the most information. Figure 30 illustrates the different industries in which Ansys Granta Edupack can be used.



figure 30 Ansys Granta interface

3.1 Sorting stages

The database chosen for this selection process is known as level 3 aerospace. The motorsport and the aerospace industry share significant similarities due to their common requirements for high performance and lightweight materials. This database contains more than four thousand different materials.

Database:	Level 3 Aerospace
Table	MaterialUniverse
Subset	Personalizado

Table 1 Database chosen in the material selection process

The different stages implemented to select potential materials are outlined in this chapter. Four stages have been applied, involving material families and mechanical properties. The number of potential materials have been reduced from 4249 to 3.

3.1.1 Stage 1: material family

The first stage correspond to the selection of the material family. Steel and aluminum are chosen due to its great ratio of mechanical properties to weight. More advanced materials, such as titanium or magnesium are disregarded due to their high cost and their complexities associated with machining them.

Steel

Steel stands as one of the most frequently used materials in engineering. It constitutes an alloy of iron and carbon, containing less than 2% carbon and 1% manganese, alongside trace amounts of other elements. The most common steel grade are carbon steels, alloy steels, stainless steels and tool steels.

Given that this design will constantly encounter exposure to air and occasional rainfall, the material chosen must withstand corrosion. Consequently, stainless steels are chosen in stage 1. Duplex, martensitic and age-hardened stainless steels are chosen based on its excellent mechanical properties. Ferritic steels are dismissed due to its fragility and austenitic steels are also excluded due their inferior mechanical properties compared to duplex stainless steel.

Stainless steels are known for their remarkable corrosion resistance and mechanical properties. It contains at least 10.5% of chromium, which forms a thin protective oxide layer on the surface of the steel. Stainless steels are available in different grades offering different properties based on their alloy composition and heat treatment. The most common grades are austenitic, ferritic, martensitic, duplex and age-hardened.

- **Duplex stainless steel:**

This steel combines features from both austenitic and ferritic grades, offering benefits from both families. It has two-phase microstructure, its structure has roughly 50% austenite and 50% ferrite. This stainless steel is known for its great strength

- **Martensitic stainless Steel**

It is a high-strength stainless steel known for its hardness. This steel contains higher carbon content, improving its robust mechanical properties. Despite its susceptibility to corrosion, proper heat treatment enhances its performance.

- **Age-hardened stainless steel:**

Age-hardened stainless steel offers excellent corrosion resistance and durability It is commonly used in aerospace components like aircraft structures. It's also used in high-stress applications such as fasteners.

Aluminum

Aluminum alloys consist primarily of aluminum, with other additional elements such as copper, manganese, silicon, magnesium and zinc. These alloys are categorized into seven distinct families, shown in table 2.

series	Corrosion resistance	Mechanical properties	applications
1XXX	good	poor	decoration
2XXX	poor	good	Aerospace
3XXX	Good	normal	Automotive components
4XXX	good	normal	Automotive components
5XXX	good	good	Naval industry
6XXX	good	great	Construction aerospace
7XXX	great	great	Aerospace Motorsport






Table 2 Aluminum series

Considering corrosion resistance and mechanical properties, series 6XXX and 7XXX have been chosen for this design.

The image below displays the materials selected for this analysis, which include duplex, martensitic, and precipitation-hardened stainless steels, as well as the 6000 series and 7000 series for aluminum.

Etapas 1:

Árbol

-  [MaterialUniverse:\Metals and alloys\Ferrous\Stainless steels\Duplex (semi-austenitic)\Wrought] 11
-  [MaterialUniverse:\Metals and alloys\Ferrous\Stainless steels\Martensitic\Wrought] 27
-  [MaterialUniverse:\Metals and alloys\Ferrous\Stainless steels\Precipitation hardened\Wrought] 39
-  [MaterialUniverse:\Metals and alloys\Non-ferrous\Aluminum\Wrought\6000 series (Mg and Si-alloyed)] 56
-  [MaterialUniverse:\Metals and alloys\Non-ferrous\Aluminum\Wrought\7000 series (Zn-alloyed)] 60

Paso de registros:

193 de 4249

3.1.2 Stage 2: material properties.

This stage filters materials based on their properties, focusing on two main characteristics, its yield strength and its cost.

Considering the limited budget of the ISC Racing Team, a maximum cost of 10 EUR/kg of material is set.

Yield strength is crucial as it signifies the stress at which a material begins to deform plastically. In the current design of the IFS05, a maximum yield strength of 30 MPa is set, with a safety coefficient of three. Hence, a minimum yield strength requirement of 30 MPa is established. Additionally, to avoid over-dimensioning the design, a high limit constraint of 500 MPa is implemented.

Etapa 2: **Límite** [Resumen](#)

Attribute:	Constants
Price (EUR/kg)	2 a 10
Yield strength (elastic limit) (MPa)	30 a 500

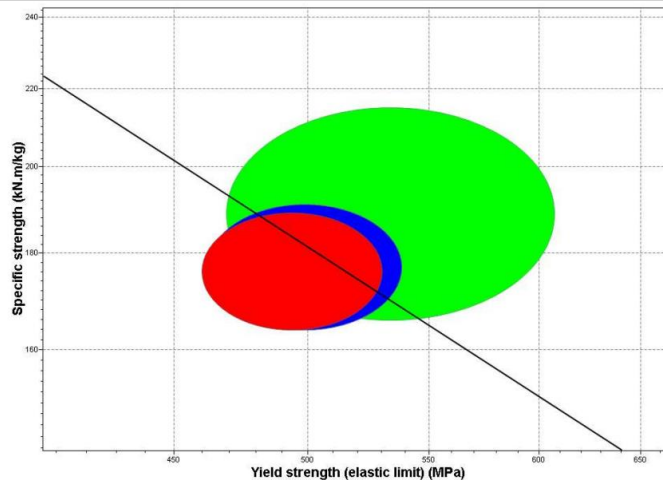
Paso de registros: 1401 de 4249

3.1.3 Stage 3. First graphical representation

This stage involves filtering through a graphical representation, where two mechanical properties are compared and optimized to find a balance between them. The goal is to maximize the values of these properties ensuring equilibrium among them. The two mechanical properties selected are specific strength, yield strength and fracture toughness. The straight line chosen to maximize both properties has a slope that values 1.

Specific strength refers to a mechanical characteristic that evaluates the material strength relative to its density, indicating the strength-to-weight ratio. Materials with notable specific strength, such as titanium, aluminum, magnesium, and steel, are frequently use in aerospace applications, where prioritizing weight reduction is crucial. In these contexts, elevated specific strength empowers designs to withstand various loads while simultaneously minimizing overall weight, thus bolstering performance and efficiency.

Etapa 3: Yield strength (elastic limit) (MPa), Specific strength (kN.m/kg)



pendiente	Valor índice	de	Index equation
-1	≥ -	-	

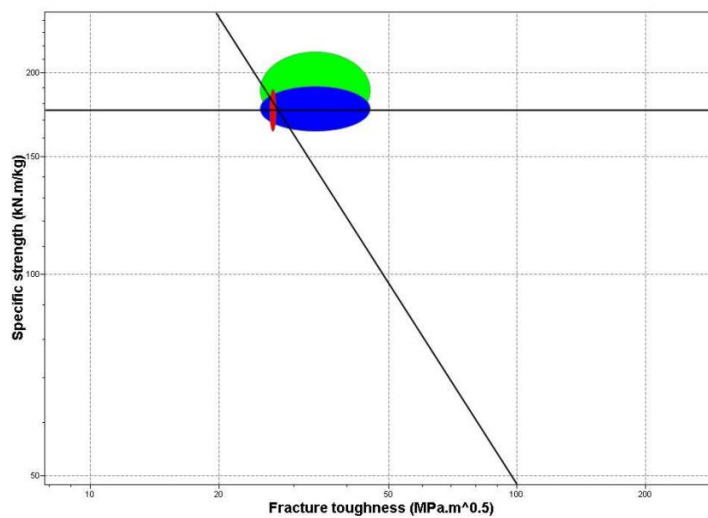
Paso de registros: 805 de 4249

3.1.4 Stage 4: Second graphical representation

This section reiterates the processes conducted in the previous stage but focuses on other mechanical properties, which are specific strength and fracture toughness.

Fracture toughness is the ability of the material to withstand cyclic loading without premature failure over time. This design will be used for two consecutive years in a racecar, with an average of more than one hundred kilometers per year. It is crucial to ensure that the design can withstand for years without early failure due to fatigue.

Etapa 4: Fracture toughness (MPa.m^{0.5}), Specific strength (kN.m/kg)



Paso de registros: 3760 de 4249

3.2 Selection results

With these four stages, the number of possible materials has been reduced from 4269 to 3, all of which are aluminum alloys. Table 3 provides a summary of the stages utilized:

<u>1</u>	Material Universe	Metals and alloys\Ferrous\Stainless steels \Duplex (semi-austenitic)\Wrought
		Metals and alloys\Ferrous\Stainless steels \Martensitic\Wrought
		Metals and alloys\Ferrous\Stainless steels \Precipitation hardened\Wrought
		Metals and alloys\Non-ferrous\Aluminum \Wrought\6000 series (Mg and Si-alloyed)
		Metals and alloys\Non-ferrous\Aluminum \Wrought\7000 series (Zn-alloyed)
<u>2</u>	Price (EUR/kg)	2 a 10
	Y Yield strength (elastic limit) (MPa)	30 a 500
<u>3</u>	Specific strength (kN.m/kg)	
	Yield strength (elastic limit) (MPa)	
<u>4</u>	Specific strength (kN.m/kg)	
	Fracture toughness (MPa.m ^{0.5})	

Table 3 Material selection process summary

Orden de rango: 3 de 4269

Table 4 contains the optimal material for this application. The three of them are aluminum alloys of the 7XXX series. Based on the analysis, aluminum 7075 T6 is chosen for its widespread availability, cost-effectiveness, and ease of machining.




Rango	Material
1	 Aluminum, 7075, T6
2	 Aluminum, 7150, T61511
3	 Aluminum, 7150, T7751

Table 4 Optimal materials for this application

Aluminum 7075 T6

This alloy is a high-strength, heat treatable wrought alloy. It contains zinc, magnesium, chromium and copper, all of which harden the alloy. It also includes small amounts of silicon, manganese and titanium.

The T6 temper designation means that it has undergone solution heat treatment and artificial aging to attain optimal mechanical properties. Even though this alloy exhibits impressive strength it also has its disadvantages, such as being difficult to weld.

Despite this, it is a perfect choice for structural parts that undergo high stresses and is widely used in industries such as aerospace, naval, automotive and military (META23) [40].

4. ADHESIVE SELECTION

The process for selecting the appropriate adhesive for this design is outlined in this section. Following what was explained previously about the different types of adhesives, it becomes evident that the ideal adhesive for this design is a two-part thixotropic structural adhesive. This choice is driven by the demanding performance requirements of the bonding operation and the materials involved.

Using the Bonding Product Selector provided by 3M, and specifying the following characteristics, the product selector recommends three adhesives, which are compared in table 5.

Characteristics:

- First substrate: aluminum
- Second substrate: carbon fiber
- Joint primarily subjected to: shear stress

ADHESIVE		viscosity at 24°C [Pa s]	mixture life at 24°C [min]	Peel strength at 24°C [N/cm]	shear strength [Mpa]		
					-55°C	24°C	82°C
	DP 420 NS	180000	20	133	31	31	9
	DP490	90000	90	60	25	31	14
	7240	120000	45	92	18	27	12

Table 5 Comparison between different adhesives

Although there may not be significant differences in terms of shear strengths at different temperatures, there is a significant variation in peel strength. Given its superior peel strength, the adhesive 3M Scotch Weld DP420NS is chosen for this design. This adhesive is known for its great resistance to both peel and shear stresses across a wide range of temperatures. Additionally it provides great fatigue resistance and its mixture life of 20 minutes allows to work properly on the design.

5. GUIDE FOR MANUFACTURING

This guide follows the procedure shown in Composite Wishbones for FS (GRAN17) [17].

5.1 Required items

To ensure optimal bonding for this design, the following items are essential:

- 3 spatulas
- grit blasting machine
- sandpaper (120/240)
- dremmel machine
- masking tape
- isopropyl alcohol
- water
- paper towels
- scales
- nitrile gloves
- mixing pots
- mixing sticks
- 3M Scotch-Weld Structural Epoxy adhesive DP420NS
- Vacuum cleaner
- Fine dust mask

5.2 CFRP tube preparation procedure

1. While sanding the interior of the tube with sandpaper (120/240) and a Dremel tool, use a vacuum simultaneously to eliminate the grit from the tube. In case the Dremel tool can not be introduced easily inside the tube, it is recommended to wrap flexible sandpaper around a screwdriver, both tools are shown in figure 31. Use a fine dust mask to protect the respiratory system at all times.



figure 31 Tools used for sanding the interior of the CFRP tube

2. Remove any residue from the component with a 50:50 mixture of isopropyl alcohol and water, using a lint-free cloth. It is recommended to wrap the lint-free cloth around a screwdriver to ensure that all the residues are removed. Repeat this process until the lint-free cloth remains clean.
3. Dry the parts in a recirculating air oven for 30 minutes at 50-60°C.
4. Ensure bonding is completed within 2 hours of preparation.

5.3 Aluminum end-fittings procedure

1. Use tape to mask off non-bonding surfaces.
2. Roughen the bonding surfaces using a grit blasting machine.



figure 32 Grit blasting machine used

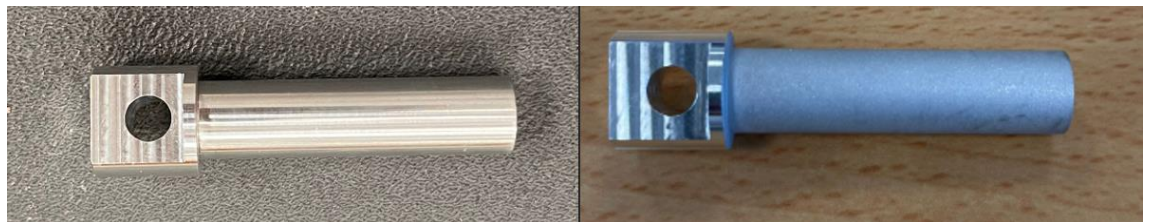


figure 33 End-fitting before (left) and after (right) blasting

3. Clean the bonding surface with a 50:50 mixture of isopropyl alcohol and water, using lint-free cloth.

5.4 Bonding procedure

1. Clean the cap of the adhesive to remove any residue.
2. Thoroughly mix the paste according to the manufacturer's instructions (2:1 by volume base to hardener or 2:0.97 by weight).

3. Apply the adhesive to the bonding surfaces using a clean, degreased spatula.
4. Assemble the components.
5. Remove any excess adhesive using a paper towel, either dry or lightly soaked in isopropanol.
6. Cure at 65° for two hours.
7. Cure at room temperature (25°C) for 24 hours.

Figure 34 illustrates the preparation of the bonding process and figure 35 shows the components bonded.



figure 34 Bonding process



figure 35 Component bonded

6. CAD DESIGNS

The tested design is shown in annex A. This design differs notably from the non-testing end-fitting design. However, these differences do not noticeably impact the stress distribution throughout the adhesive. The testing end-fitting design features a pin hole to facilitate secure handling by the testing equipment. It lacks threading., aiming to minimize manufacturing costs without modifying the results.

The size of the carbon fiber tube can not be changed as the suspension and dynamics department design that size for the bar loads. Therefore, in order to simulate how does the adhesive with, the size of the diameter of the end-fitting which is in contact with the adhesive is changed.

Four designs are presented

- **EF-1:** is the one chosen for the testing machine. It has the less milling operations to do the testing. It is the easiest and cheapest to manufacture.
- **EF-2:** its design is very similar to EF-1 but changing the adhesive diameter to 11.7 mm to have an adhesive thickness of 0.15 mm
- **EF-3:** follows the same design philosophy than EF-2 but changing the adhesive diameter to 10.80 mm to have an adhesive thickness of 0.6mm
- **EF-4:** is the design of the testing end-fitting, shown in figure 36.
- **EF-5:** the most optimum design without taking manufacturing cost as a variable.

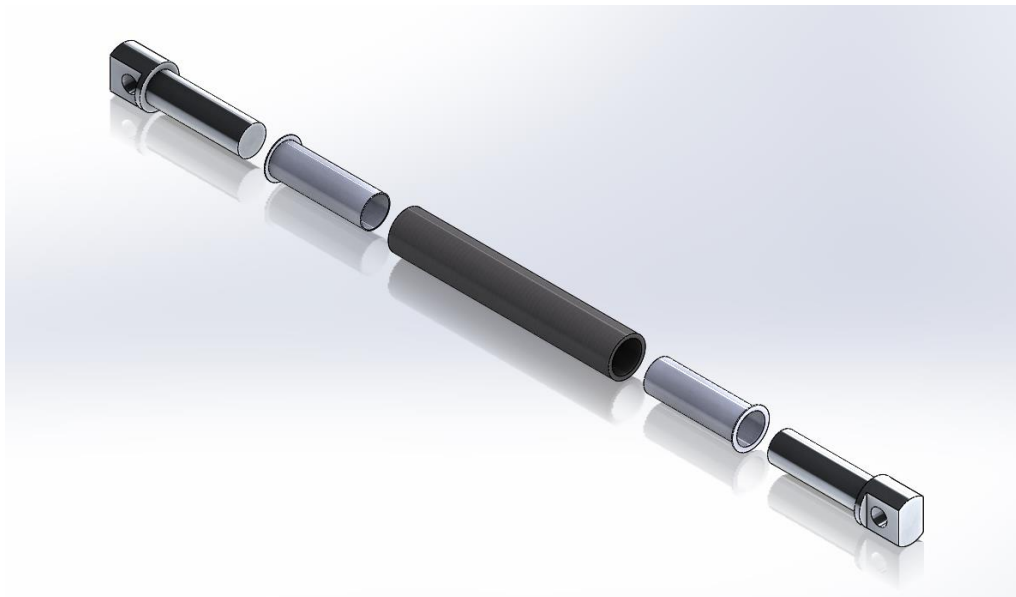


figure 36 Exploded view of EF-4

7. SIMULATIONS

7.1 simulation characteristics

Ansys Mechanical has been selected for this analysis. Seven distinct static structural simulations are conducted, each with different adhesive geometries. The variables chosen are the adhesive length and the adhesive thickness. The simulation parameters remain consistent across all the simulations.

The stress through the adhesive follows a “u” shape with peak stresses at the edges. The optimal design will have peak stresses values of 10.33 MPa at the edges.

The simulations analyzed in this chapter are the following:

- To achieve the optimal **adhesive length** knowing how does the stress vary modifying the end-fitting length:
 - **EF-1-30** design 1 with end-fitting length of 30 mm an adhesive thickness of 0.30mm.
 - **EF-1-37.5** design 1 with end-fitting length of 37.5 mm an adhesive thickness of 0.30mm.
 - **EF-1-45** design 1 with end-fitting length of 45 mm an adhesive thickness of 0.30mm.

- To know how much the stress varies with the **adhesive thickness**:
 - **EF-2-45-0.15** design 1 with end-fitting length of 45mm an adhesive thickness of 0.15mm
 - **EF-3-45-0.6** design 1 with end-fitting length of 45mm an adhesive thickness of 0.60mm

- To know how much does the previous simulations vary with the **testing boundary conditions**.
 - **EF-4-45** design 4 with end-fitting length of 45mm an adhesive thickness of 0.3mm.

- To achieve the **optimal design**:
 - **EF-5-45** design 5 with end-fitting length of 45mm with variable adhesive thickness.

7.1.1 Engineering data

This chapter displays the mechanical properties of the materials utilized.

Aluminum 7075 T6

Figure 37 and figure 38 show the properties of the aluminum 7075 T6.

Properties of Outline Row 4: aluminum 7075 T6			
	A	B	C
1	Property	Value	Unit
2	Material Field Variables	Table	
3	Density	2800	kg m ⁻³
4	Isotropic Elasticity		
5	Derive from	Young's Modulus and Po...	
6	Young's Modulus	76000	MPa
7	Poisson's Ratio	0.33	
8	Bulk Modulus	7.451E+10	Pa
9	Shear Modulus	2.8571E+10	Pa
10	Uniaxial Test Data	Tabular	
11	Scale	1	
12	Offset	0	MPa
13	Tensile Yield Strength	572	MPa
14	Tensile Ultimate Strength	572	MPa

figure 37 Aluminum 7075 T6 properties

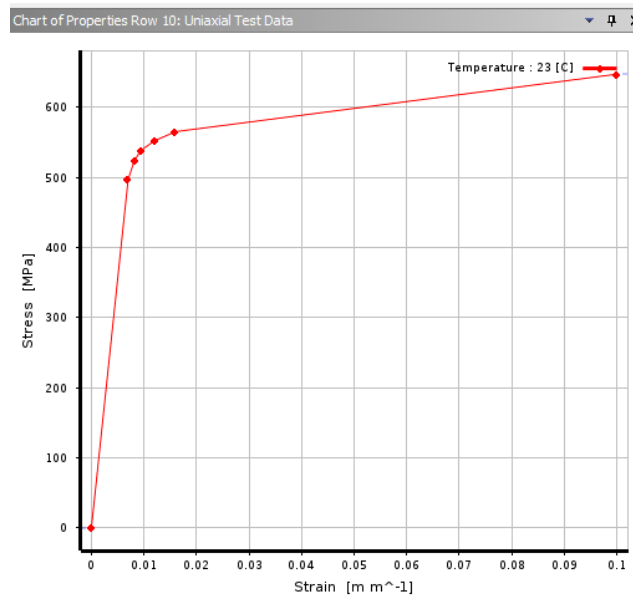


figure 38 Aluminum 7075 uniaxial test data

3M Scotch Weld DP420NS

The parameters have been supplied by 3M. Figure 39 and figure 40 display the characteristics of the structural adhesive used in the simulation.

Properties of Outline Row 3: Adhesive 3M DP420NS			
	A	B	C
1	Property	Value	Unit
2	Material Field Variables	Table	
3	Density	1086	kg m ⁻³
4	Isotropic Elasticity		
5	Derive from	Young's Modulus and Po...	
6	Young's Modulus	1.9543E+09	Pa
7	Poisson's Ratio	0.3957	
8	Bulk Modulus	3.123E+09	Pa
9	Shear Modulus	7.0013E+08	Pa
10	Multilinear Isotropic Hardening	Tabular	
11	Scale	1	
12	Offset	0	Pa

figure 39 3M Scotch Weld DP420 NS properties

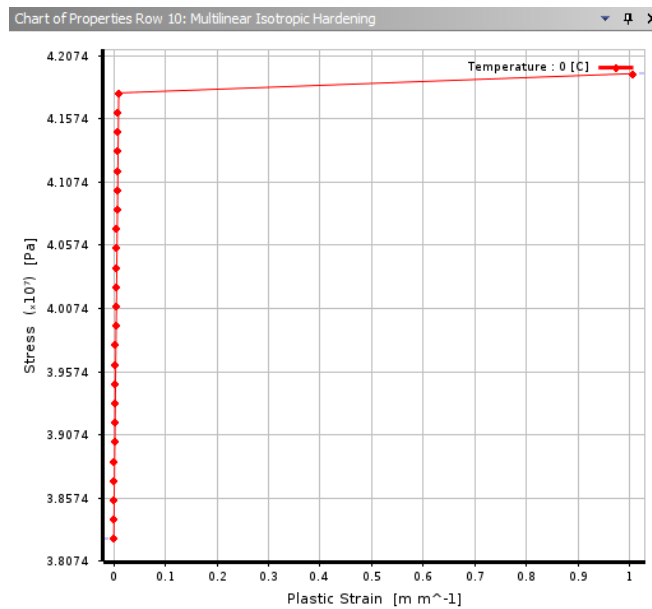


figure 40 3M Scotch Weld DP420 NS multilinear isotropic hardening data

Carbon fiber

Figure 41 and figure 42 present the Carbon fiber tube parameters provided by ClipCarbono, the carbon fiber tube provider.

Properties of Outline Row 5: carbon fiber			
	A	B	C
1	Property	Value	Unit
2	Material Field Variables	Table	
3	Density	1.6	g cm ⁻³
4	Orthotropic Elasticity		
5	Young's Modulus X direction	70000	MPa
6	Young's Modulus Y direction	70000	MPa
7	Young's Modulus Z direction	5000	MPa
8	Poisson's Ratio XY	0.1	
9	Poisson's Ratio YZ	0.05	
10	Poisson's Ratio XZ	0.05	
11	Shear Modulus XY	5000	MPa
12	Shear Modulus YZ	5000	MPa
13	Shear Modulus XZ	500	MPa
14	Uniaxial Test Data	Tabular	
15	Scale	1	
16	Offset	0	MPa
17	Orthotropic Stress Limits		
18	Tensile X direction	720	MPa
19	Tensile Y direction	720	MPa
20	Tensile Z direction	90	MPa
21	Compressive X direction	-570	MPa
22	Compressive Y direction	-570	MPa
23	Compressive Z direction	-70	MPa
24	Shear XY	100	MPa
25	Shear YZ	100	MPa
26	Shear XZ	200	MPa

figure 41 CFRP tube properties

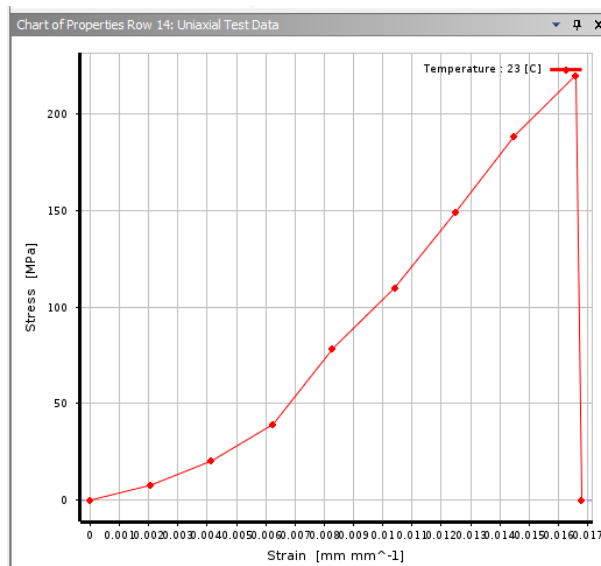


figure 42 uniaxial test data

7.1.2 Simulation parameters

In each simulation, the adhesive is specified as the contact material, while either the carbon fiber tube or the aluminum end fitting is chosen as the target.

Meshing

Achieving a quality mesh is essential for obtaining accurate results and achieving rapid convergence in simulations. In meshing contacts, it is critical to ensure nodes are shared between the contacting surfaces to accurately capture interaction and behavior. Figure 43 illustrates the meshing of the assembly.

The structural adhesive provider advised meshing the adhesive thickness with a minimum of two elements, as shown in figure 44.

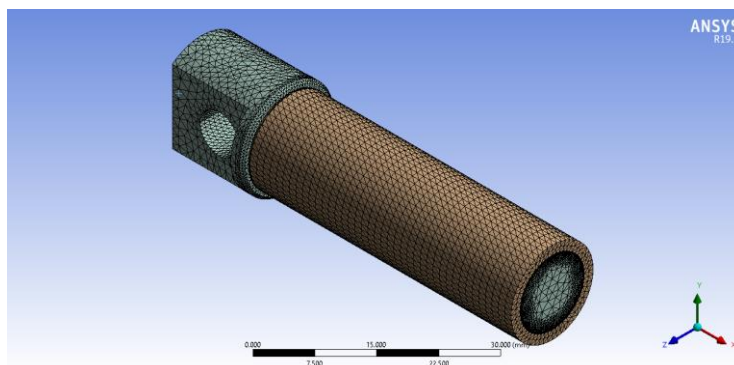


figure 43 Meshing view of the assembly

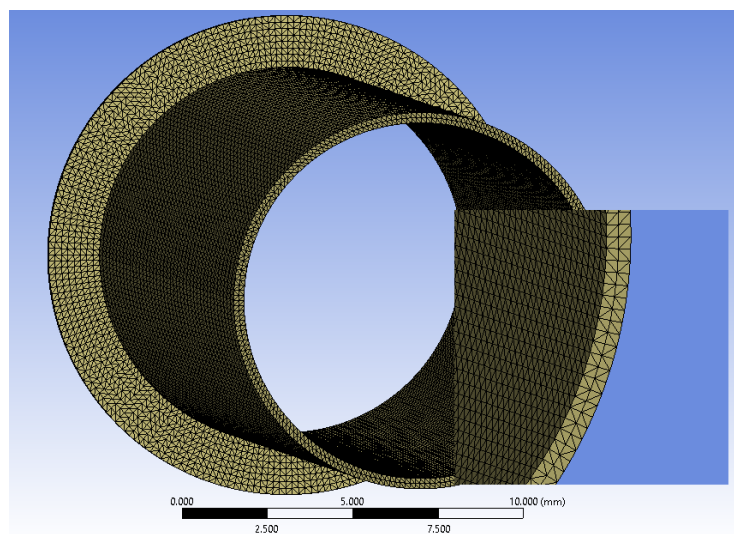


figure 44 Adhesive meshing detail

Static elements

To simplify the simulation and reduce the simulation times, it is assumed that the furthest face from the pin hole is fixed and the force is applied in the pin hole, where the machine's retaining pin operates. This simplification will be verified with simulations. Figure 45 shows where the force is applied and figure 46 the fixed face.

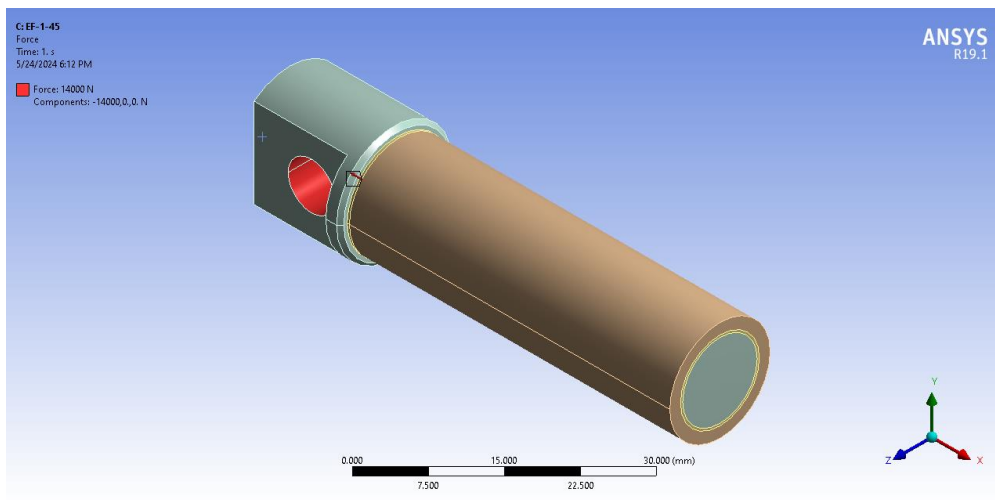


figure 45 Force applied in the end-fitting

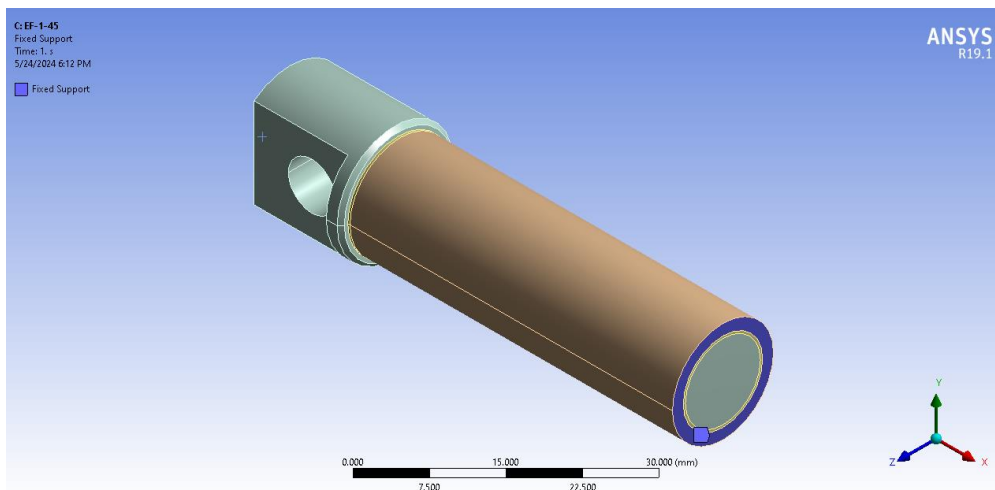


figure 46 Carbon fiber fixed face

The force is applied in the pin-hole, it has -x direction and has a value of 14377 N. This force is the maximum load for the case with maximum load for any suspension bar. It corresponds to the low-forward rear suspension arm. Figure 47 shows the operating force under fatigue (only in tension), buckling, compression and tension for each suspension

bar for 22 different loading scenarios. Figure 48 shows the maximum operating load for each suspension bar for the previous working regimes previously mentioned.

	Up-Fore	Up-Aft	Low-Fore	Low-Aft	Push/Pull	Tie/Toe	
	2197	-1659	-6925	1590	2455	2105	
1	0	0	0	0	0	0	
2	160	91	281	-1,382	1,187	96	
3	-218	264	1,057	-864	232	-236	
4	1,595	1,616	-89	-7,735	2,614	211	
5	160	91	281	-1,382	1,187	96	
6	2,197	-1,659	-6,925	1,590	2,455	2,105	
7	-279	1,955	4,434	-6,699	1,343	-1,032	
8	4,241	-468	-9,371	-3,966	3,741	2,708	
9	732	-199	-2,309	655	-492	475	
10	438	-1,142	-2,473	2,215	1,001	831	
11	160	91	281	-1,382	1,187	96	
12	160	91	281	-1,382	1,187	96	
13	215	-240	-965	704	-129	227	
14	2,790	2,916	-517	-12,776	3,418	276	
15	160	91	281	-1,382	1,187	96	
16	2,966	-2,343	-9,731	2,878	2,821	2,869	
17	6,262	-783	-14,377	-4,806	4,632	4,003	
18	-435	2,603	5,878	-8,535	1,382	-1,427	
19	802	455	1,404	-6,908	5,937	479	
20	488	-1,378	-3,002	2,927	942	970	
21	1,750	-438	-5,297	1,136	-811	1,132	
22	1,110	-811	-3,399	616	1,366	1,056	
	-279	-1659	-9371	-7735	-492	-1032	N
	6262	2916	5878	2927	5937	4003	N
	6262	2916	5878	2927	5937	4003	N
	-435	-2343	-14377	-12776	-811	-1427	N

Highest Operating Force

figure 47 Suspension case loads for each suspension bar

-279	-1659	-9371	-7735	-492	-1032	N	Fatigue (only in tension)
6262	2916	5878	2927	5937	4003	N	Buckling
6262	2916	5878	2927	5937	4003	N	Comp
-435	-2343	-14377	-12776	-811	-1427	N	Tens

figure 48 Maximum loads for each suspension bar

7.2 Simulation results

This section presents the results of various simulations that explore how changes in the adhesive geometry affects the stress values. For each simulation, the minimum, maximum and average stress of the adhesive values are presented, as well as an isometric and lateral view of the stress distribution.

Two adhesive parameters will be investigated, namely adhesive length and adhesive thickness.

7.2.1 Adhesive length simulation

The following simulations examine the stress distribution along the adhesive length, each conducted with a different adhesive length setting. The first simulation focuses on an adhesive length of 30mm, followed by the second simulation with a length of 45mm. The third simulation explores the adhesive length set to 37.5mm.

The maximum, minimum and average results of the adhesive stress distribution for each simulation are shown in table 6.

		Equivalent Von-Mises Stress (Mpa)		
		Minimum	Maximum	Average
ADHESIVE LENGTH (mm)	30	3.3736	41.913	20.882
	37.5	2.0554	47.332	20.389
	45	1.3294	44.971	17.601

Table 6 Adhesive length simulations results

EF-1-30

This simulation illustrates the stress distribution along the adhesive. This design has an adhesive length of 30mm and an adhesive thickness of 0.3mm.

The results of this simulations are presented in figure 49 and figure 50.

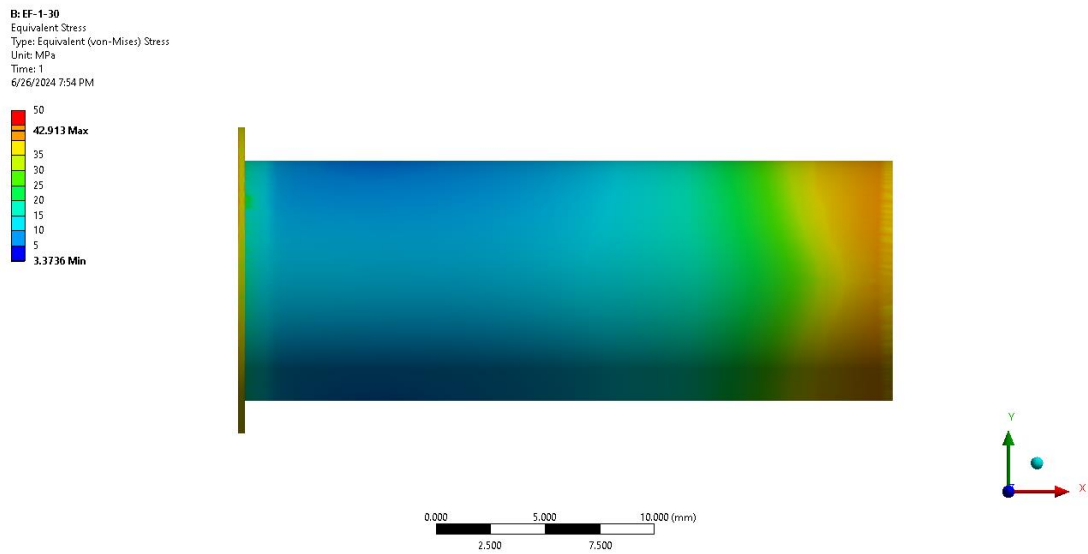


figure 49 Stress distribution for EF-1-30. Lateral view.

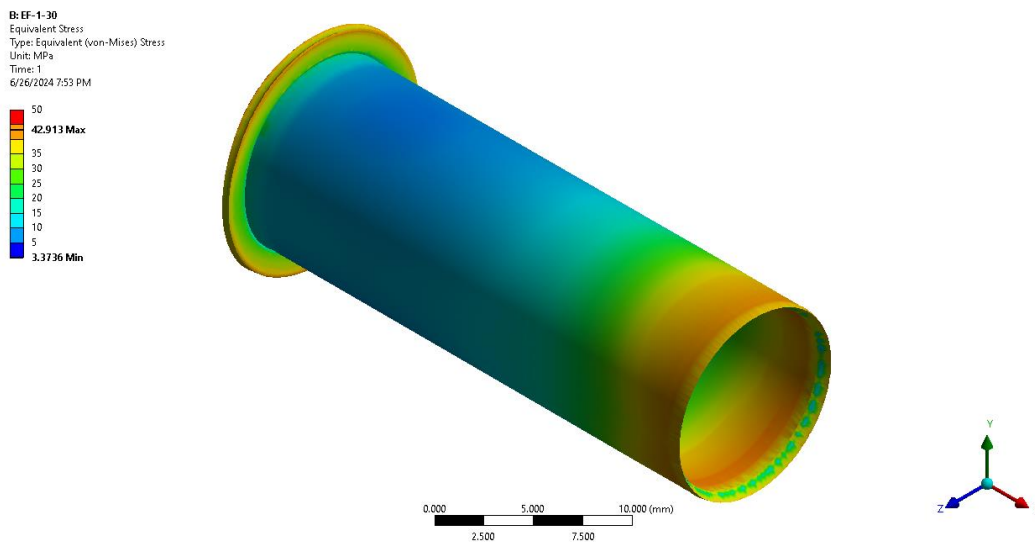


figure 50 Stress distribution for EF-1-30. Isometric view.

EF-1-45

This simulation corresponds to an adhesive length of 45 mm and an adhesive thickness of 0.3mm.

The results of this simulation are presented in figure 51 and figure 52.

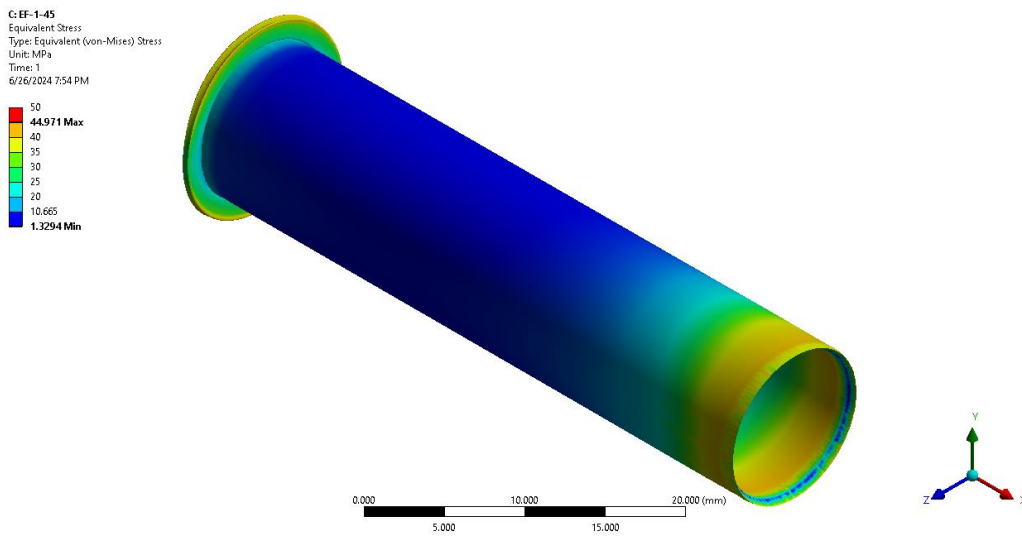


figure 51 Stress distribution for EF-1-45. isometric view

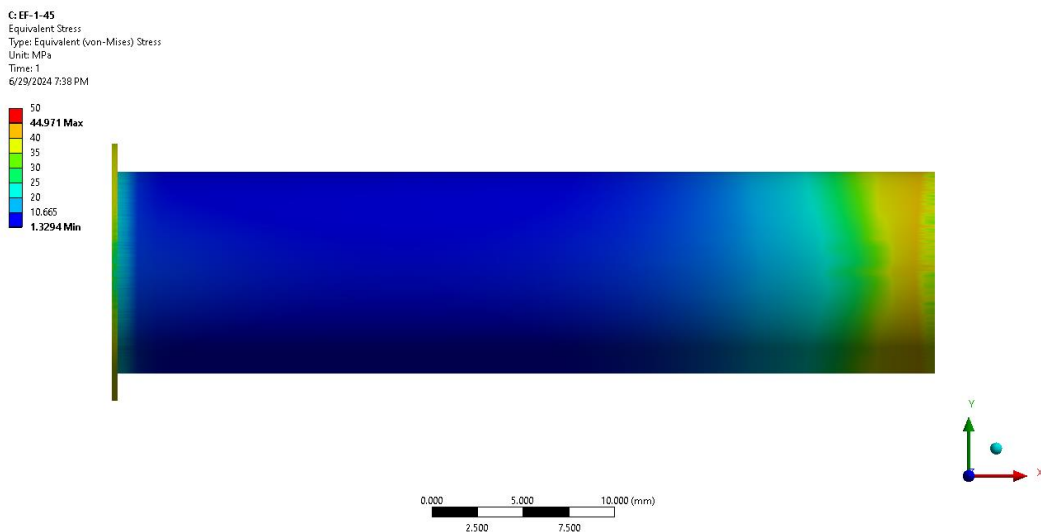


figure 52 Stress distribution for EF-1-45. lateral view

EF-1-37.5

This simulation corresponds to an adhesive length of 37.5 mm and an adhesive thickness of 0.3mm.

Figure 53 and figure 54 presents the stress distribution for the previous design with adhesive length equal to 37.5 mm and adhesive thickness equal to 0.3 mm.

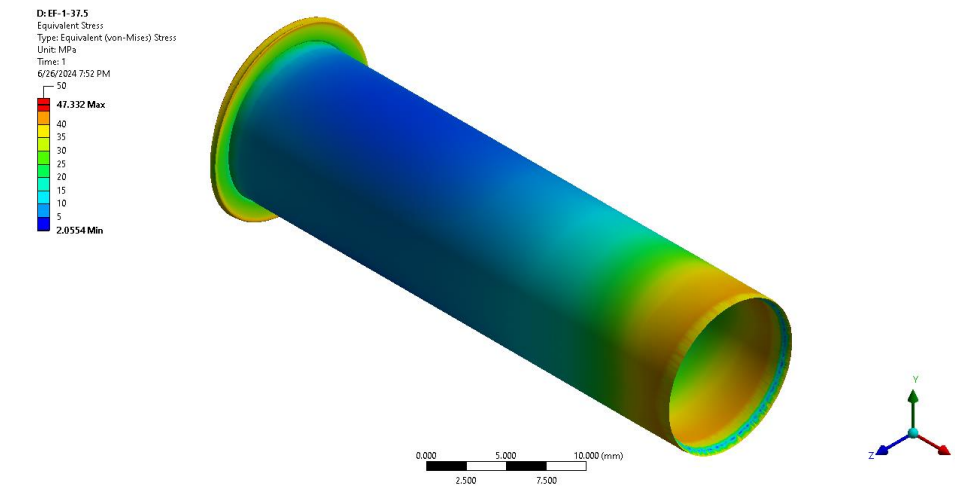


figure 53 Stress distribution for EF-1-37.5. isometric view

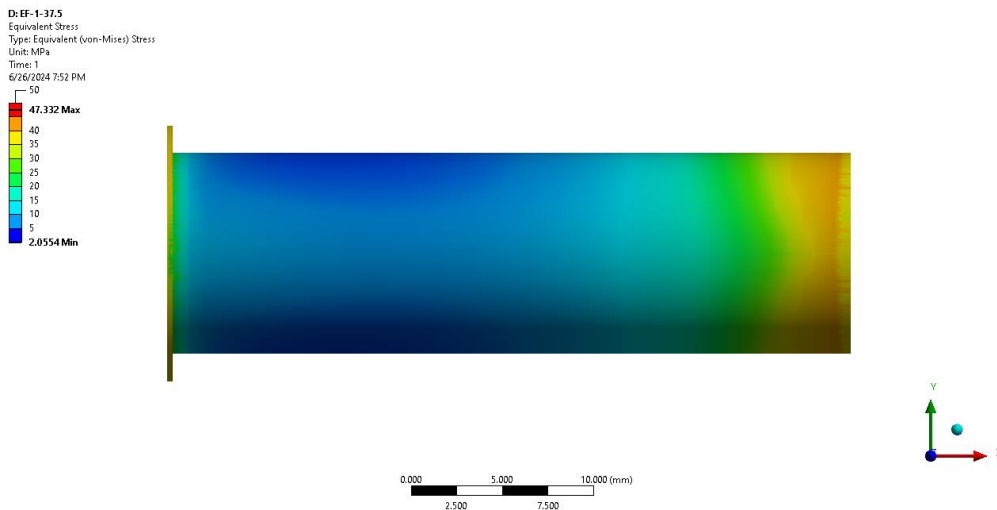


figure 54 Stress distribution for EF-1-37.5. Lateral view

7.2.2 Adhesive thickness simulations

In this section, three different adhesive thicknesses—0.15 mm, 0.30 mm, and 0.60 mm—are simulated to analyze their influence on the stress distribution along the adhesive. The simulations presented in this section are the following:

- EF-2-45-0.15
- EF-3-45-0.6

The maximum, minimum and average results of the adhesive stress distribution for each simulation are shown in table 7.

		Equivalent Von-Mises Stress (Mpa)		
		Minimum	Maximum	Average
ADHESIVE THICKNESS (mm)	0.15	0.6307	48.354	16.546
	0.3	1.3294	44.971	17.601
	0.6	1.9628	44.699	14.37

Table 7 Adhesive thickness simulations results

EF-2-45-0.15

This simulation corresponds to the design number two, which has an end-fitting external diameter of 11.70 mm and an adhesive thickness of 0.15 mm. The results of this simulation are shown in figure 55 and figure 56.

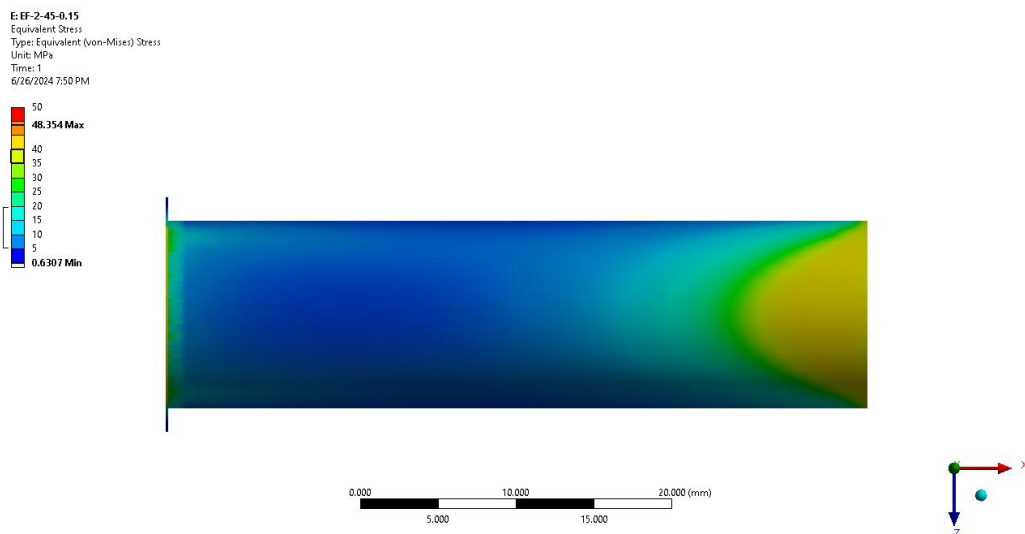


figure 55 EF-2-45-0.15 Stress distribution. Lateral view

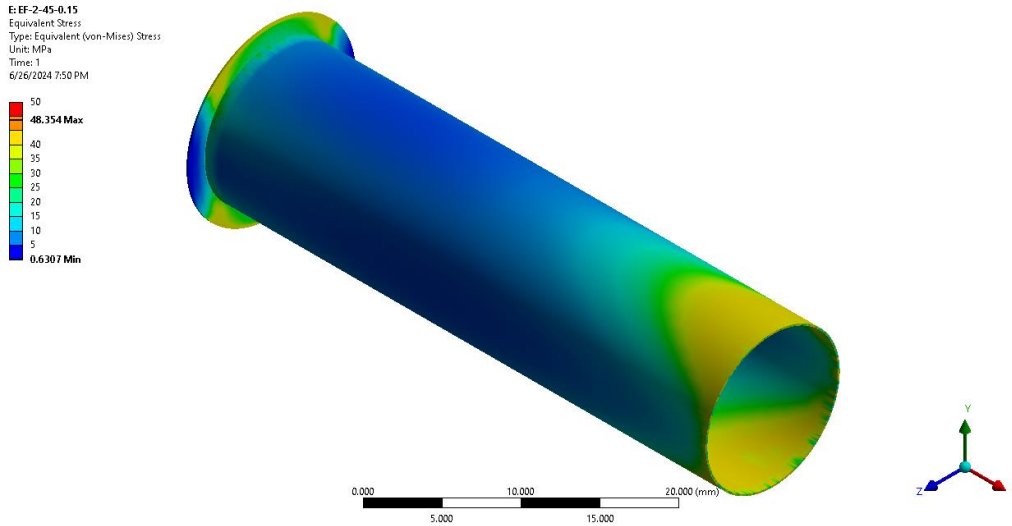


figure 56 EF-2-45-0.15 Stress distribution. Isometric view

EF-3-45-0.6

This simulation corresponds to the design number two, which has an end-fitting external diameter of 10.40 mm and an adhesive thickness of 0.15. Figure 57 and figure 58 presents the results for this simulation.

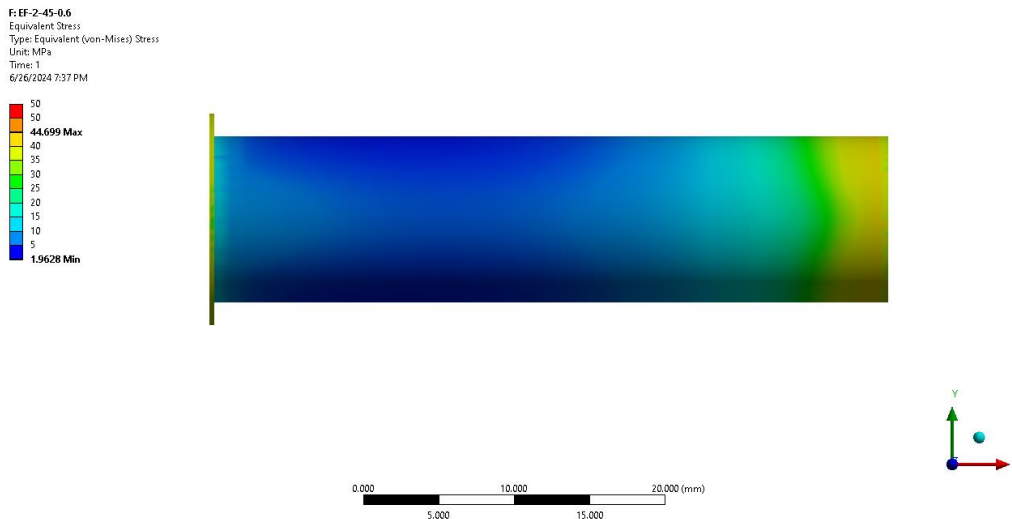


figure 57 EF-3-45-0.6. Lateral view

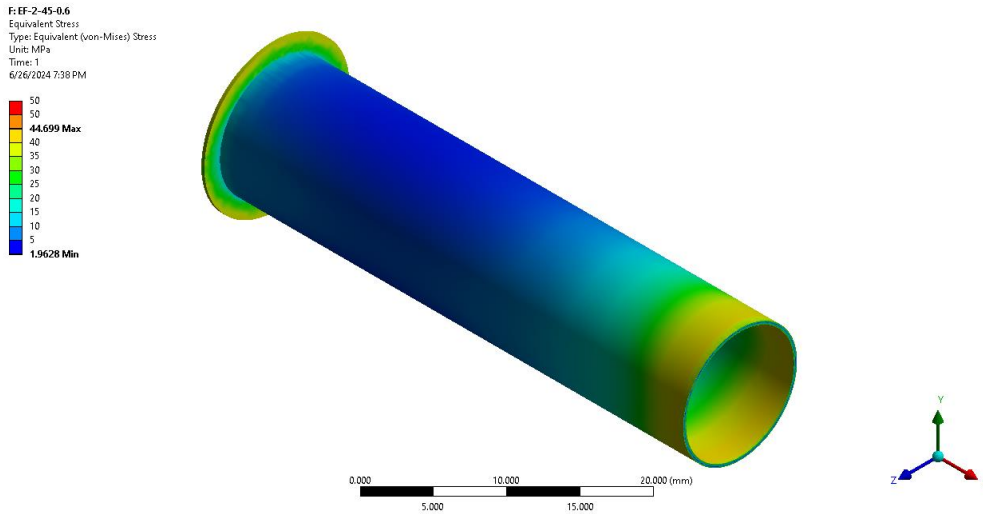


figure 58 EF-3-45-0.6. Lateral view

7.2.3 Testing boundary conditions simulation

In this simulation, the testing assembly, shown in figure 59 is modeled to achieve a realistic correlation between simulation and actual testing. The goal is to know if there is significant difference between considering the section wall of the carbon fiber as fixed and simulate half of the assembly, simplifying the simulation and reducing the simulation time.



figure 59 Testing assembly modeled in CAD

EF-4-45

This simulation presents the Von-Mises stress distribution for the same design as presented in EF-1-45, but with other boundary conditions. This simulation aims to replicate the way the testing machine works. Table 8 shows the differences between the values for the simplified model and the non-simplified one. Figure 60 and figure 61 illustrates a graphical representation of the stress distribution along the adhesive.

	Minimum	Maximum	Average
EF-1-45	1.3294	44.971	17.601
EF-4-45	4.3596	41.721	18.291
Difference	3.0302	-3.25	0.69

Table 8 Differences between EF-1-45 and EF-4-45. Values in MPa

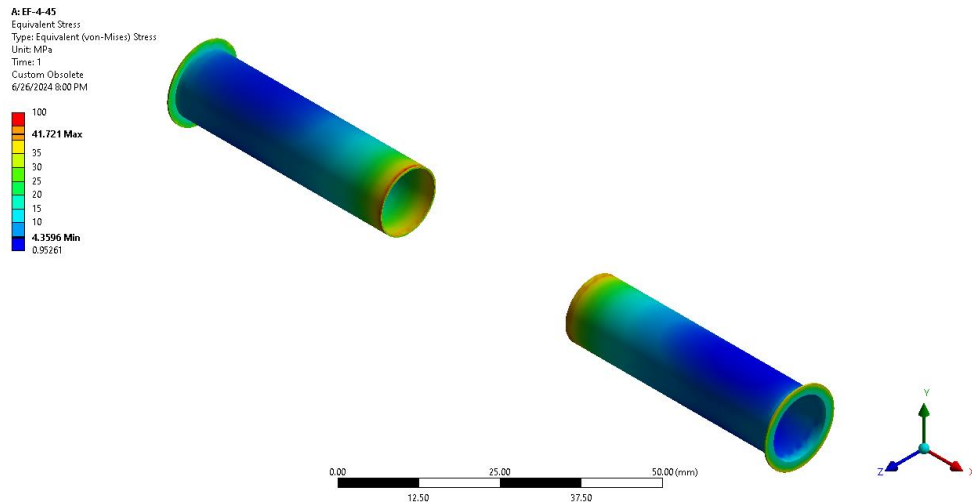


figure 60 Stress distribution for EF-4-45. Isometric view

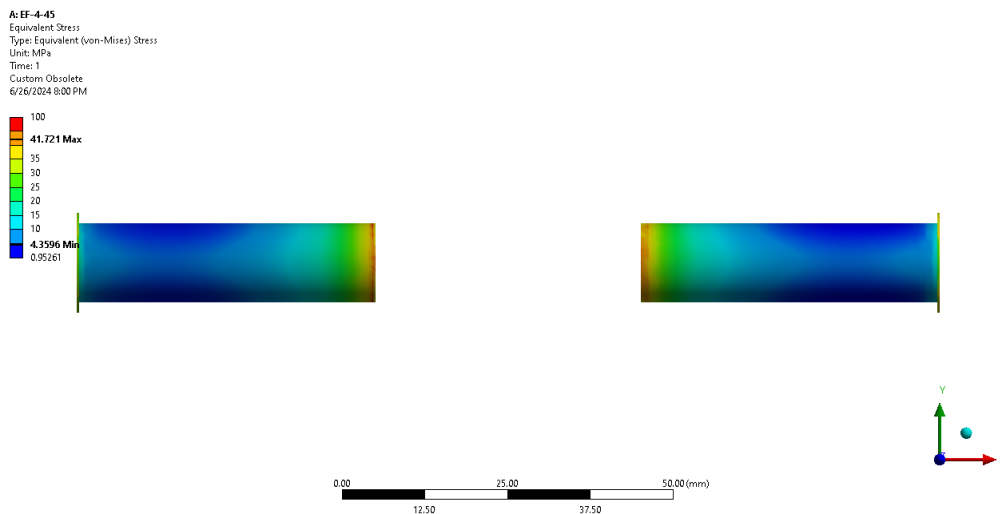


figure 61 Stress distribution for EF-4-45. Lateral view

7.2.4 Optimum design

EF-5-45

This design is the non-testing end-fitting with adhesive length equal to 45mm and variable adhesive length, which is increased at the edges to reduce peak stresses.

Table 9 presents the results for this simulation, showing the maximum, minimum and average stress values within the adhesive. Figure 62 and figure 63 illustrate the stress distribution view.

Tabular Data				
	Time [s]	Minimum [MPa]	Maximum [MPa]	Average [MPa]
1	1.	0.14691	8.884	5.8672

Table 9 EF-5-45 Simulation results

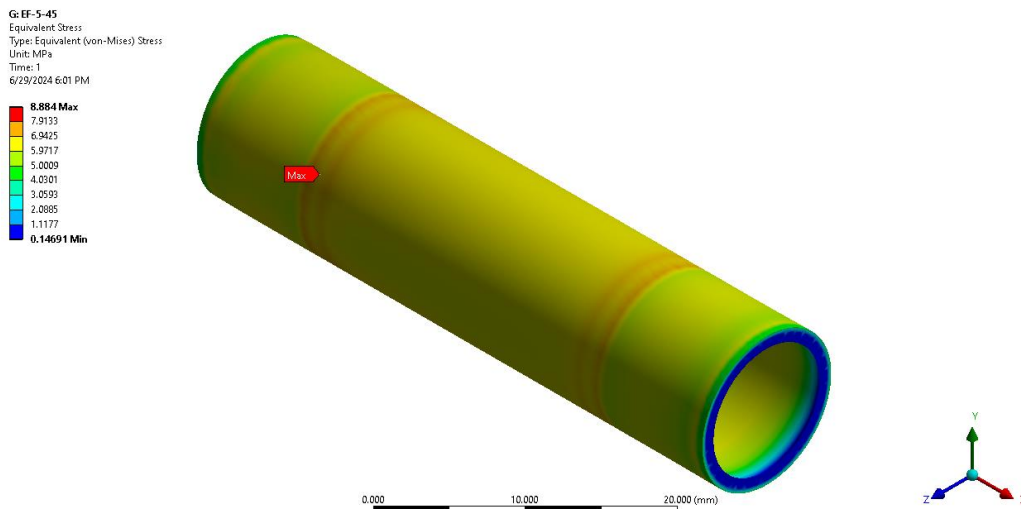


figure 62 Stress distribution for EF-5-45. Isometric view

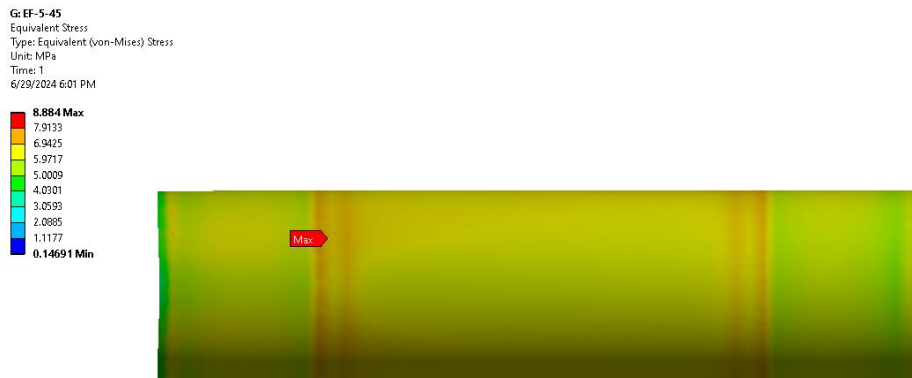


figure 63 Stress distribution for EF-5-45. Lateral view

7.3 Simulations conclusions

This section presents the conclusions of the simulation.

Influence of the adhesive length

Figure 64 and table 10 presents the results for the adhesive length simulation. offers a visual representation of the stress distribution within the adhesive. It illustrates how the stress distribution in the middle part significantly decreases as the adhesive length increases. Additionally, the table shows that the peak stresses near the lateral faces remain largely unchanged, indicating that increasing the adhesive length does not substantially alleviate the peak stresses at the edges.

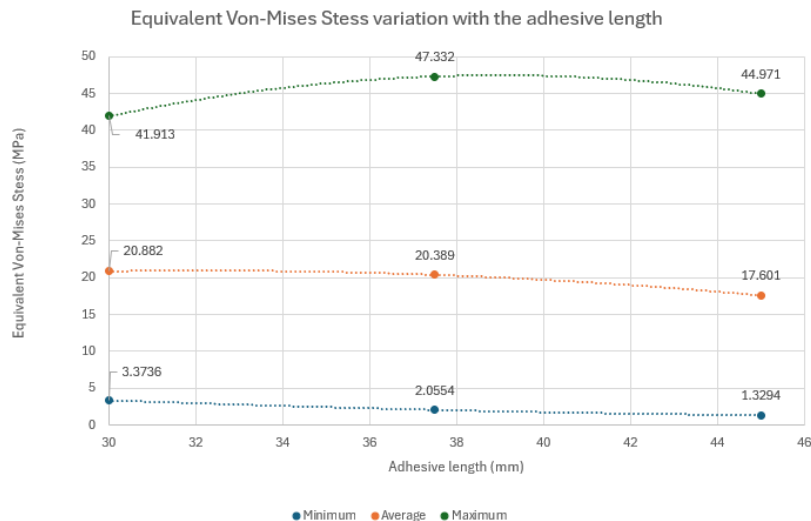


figure 64 Equivalent Von-Mises Stress variation with the adhesive length

There is no significant difference between the stresses for adhesive lengths of 30 mm and 37.5 mm. However, a substantial difference is observed between the lengths of 37.5 mm and 45 mm. As the adhesive length increases, the minimum stress value decreases, following a linear relationship. In contrast, the average stress value shows a polynomial distribution, with a notable reduction at 40 mm. The peak stress value follows a parabolic distribution, reaching a maximum of 48 MPa.




Simulation name	Adhesive length (mm)	Lateral view
EF-1-30	30	
EF-1-37.5	37.5	
EF-1-45	45	

Table 10 Adhesive length comparison. Visual representation

Adhesive thickness:

The adhesive thickness does have an influence on the stress distribution. Figure 65 depicts how the minimum, maximum and average stress values evolve with the adhesive thickness. Table 11 provides a visual representation of stress values for different adhesive thickness.

For this design the most optimum adhesive thickness is combining 0.3 mm at the center of the end-fitting and 0.6 mm at the edges to reduce peak stresses.

The minimum stress value shows a direct linear relationship with adhesive thickness. Conversely, both the average and maximum stress values exhibit a parabolic relationship. The average stress peaks at 0.3 mm and reaches its minimum at the 0.6 mm.

For this design the most optimum adhesive thickness is the combination of 0.3 mm at the center of the end-fitting and 0.6 mm at the edges to reduce peak stresses.

The results obtained from this simulations do correlate with the work of Hipol in “analysis and optimization of a tubular lap joint subjected to torsion” (HIPO84)[32], in which the

author analyzes the stress gradient that occurs through the adhesive. The author concludes that an excessively thick adhesive layer may introduce intolerable levels of flaws and porosity.

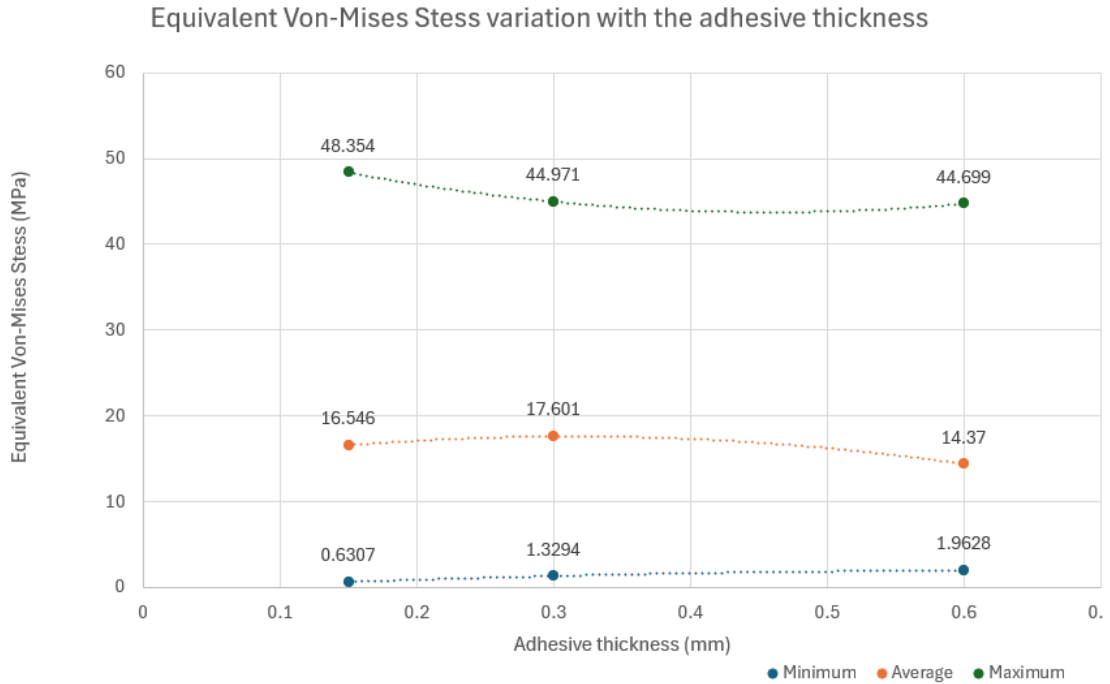


figure 65 Equivalent Von-Mises Stress variation with the adhesive thickness




Adhesive thickness (mm)	Lateral view
0.15	
0.30	
0.60	

Table 11 Adhesive thickness comparison. Visual representation

Boundary conditions simplification

The model can be simplified by assuming that the carbon fiber tube wall remains fixed, allowing simulation of the adhesive behavior in just one end-fitting.

Table 12 illustrates that the minimum stress value does drastically increase when simulating EF-4-45. However, the minimum stress value does not constrain this design as long as it is under 10 MPa. The maximum stress value does get reduced, which is beneficial for our design. Finally, the average value do slightly increase, however the increase is in the lower values.

Figure 66 provides a graphical representation illustrating the differences in stress distribution between EF-1-45 and EF-4-45. Table 12 presents the minimum, maximum, and average stress values for these simulations, along with the differences between these values.

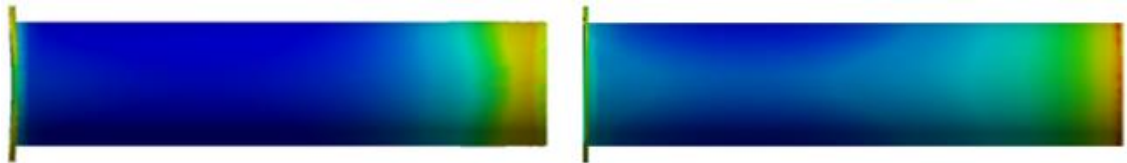


figure 66 Boundary conditions simplification stress distribution

	Minimum	Maximum	Average
EF-1-45	1.3294	44.971	17.601
EF-4-45	4.3596	41.721	18.291
Difference	3.0302	-3.25	0.69

Table 12 Differences between EF-1-45 and EF-4-45

8. TESTING

Testing will be done to check the simulation accuracy. If the test correlates with the simulation, the simulation can be verified and use the same parameters for further projects.

The testing machine that will be used is the Ibertest Elib 20, shown in figure 67. This electromechanical testing machine is specifically designed for tensile testing according to ISO 6892, IS 1608, and EN 10002-1 standards.



figure 67 Testing machine used

Figure 68 illustrates the parameters selected for the test. A speed of 1 mm/min was chosen to ensure a static test. The maximum load capacity of the load cell is 20,500 N.

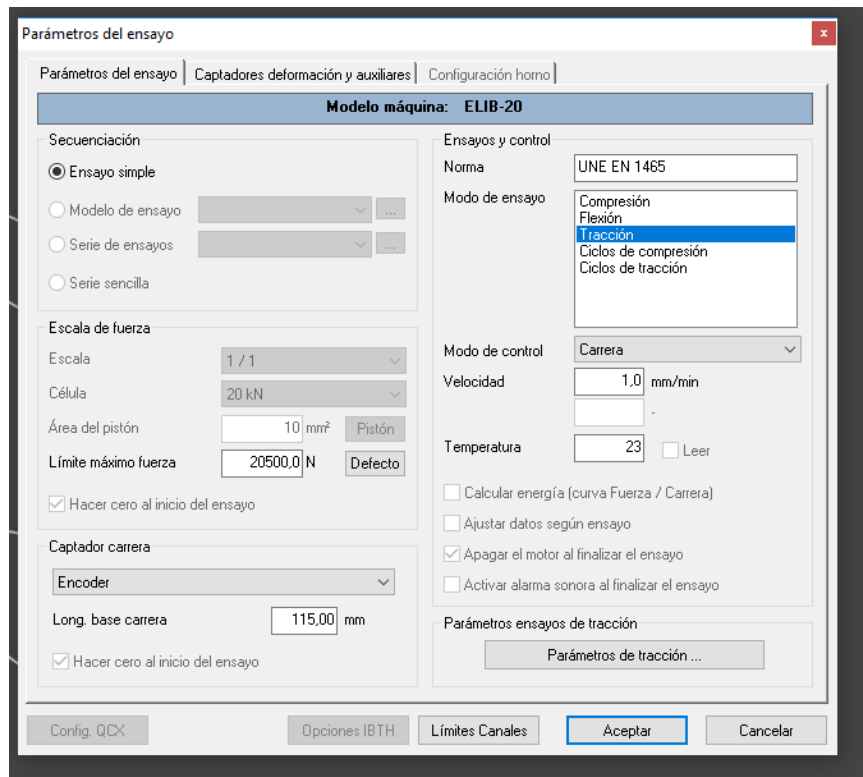


figure 68 Testing parameters

8.1 Testing results

Two test are done on EF-1-45. The testing specimen is connected to the machine by two M6 steel pins. Figure 69 shows the machine preparation before testing.



figure 69 Testing machine preparation

Figure 70 presents the results for the first test. It can be seen that the force and the stroke of the test have a linear relation. The test ended when the machine reached 10705 N, however the end-fitting remains adhered to the carbon fiber when reaching this force.

Figure 73 plots the results for the second test. The test finalized when 13012 N was reached. The end-fitting remains again adhered to the carbon fiber when the test ended.

The testing assemblies after testing can be seen in figure 71 for the first test and in figure 72 for the second test.

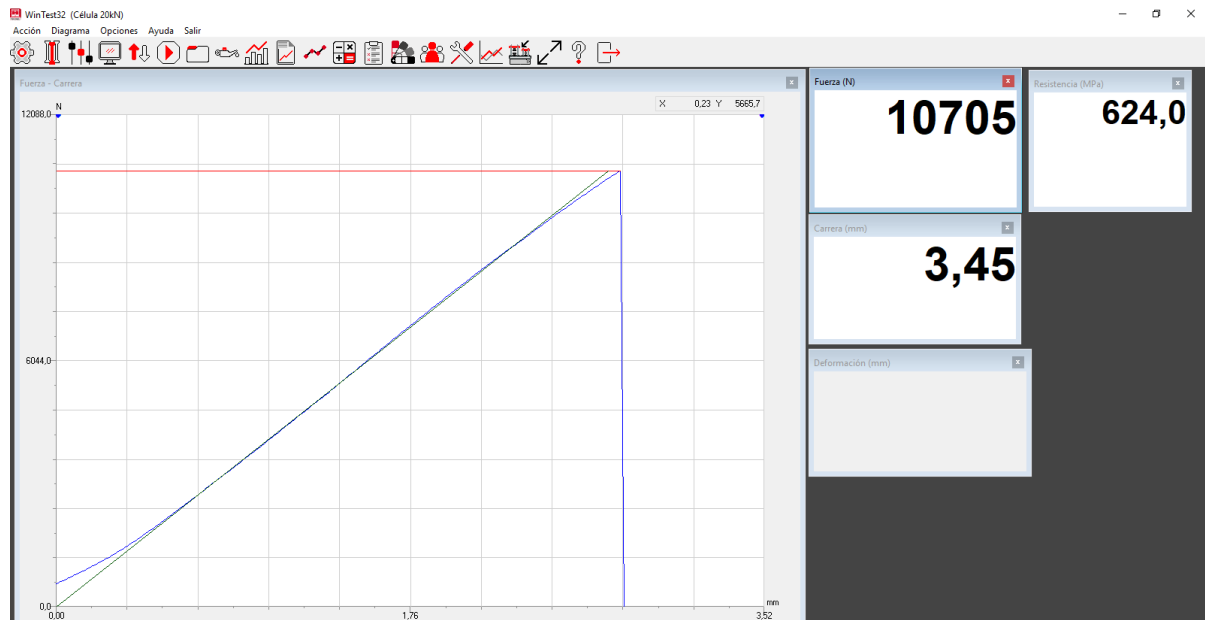


figure 70 First test results



figure 71 First testing assembly after testing

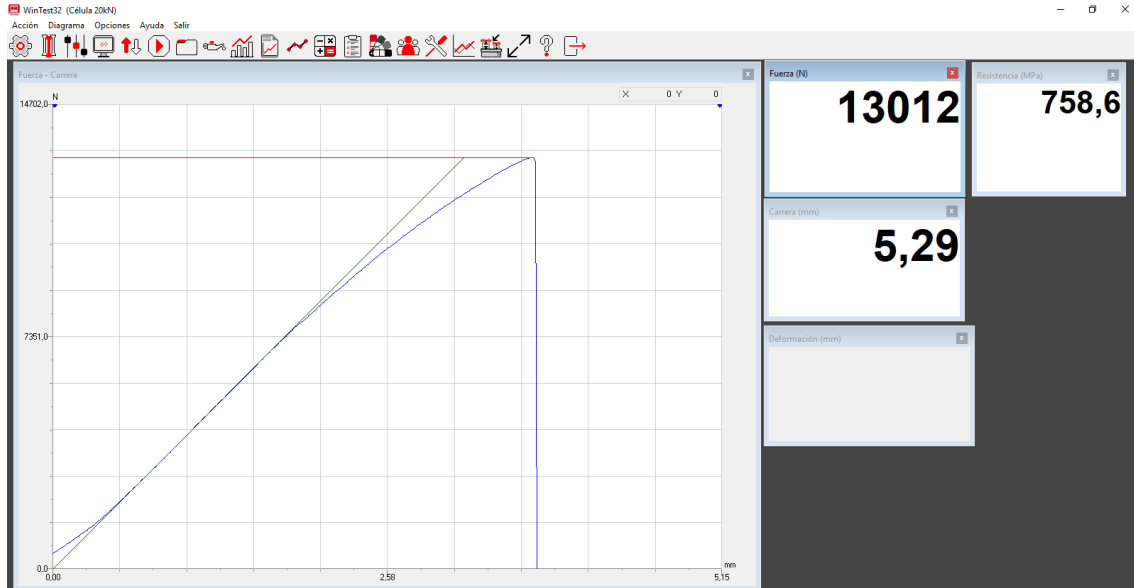


figure 72 Second test results



figure 73 Second testing assembly after testing

8.2 Simulation validation results

The tested suspension arm undergoes simulation with identical contour conditions, which are fixed in one pin hole as shown in figure 74 and tensile load in the other pin hole, represented in figure 75. The suspension arm is subjected to the load that caused the carbon fiber tube to detach from the end-fitting, 13,012 N. The goal is to determine if the simulation predicts adhesive failure at this load, validating the model.

The results of this simulation are presented in figure 76, in which the stress distribution in the adhesive is plotted.

A: EF-4-45
Fixed Support
Time: 1 s
7/3/2024 11:06 PM

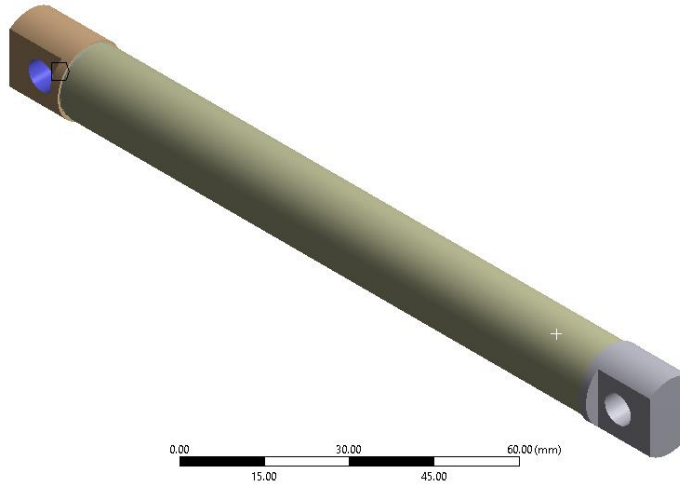


figure 74 Fixed support

A: EF-4-45
Force
Time: 1 s
7/3/2024 11:06 PM

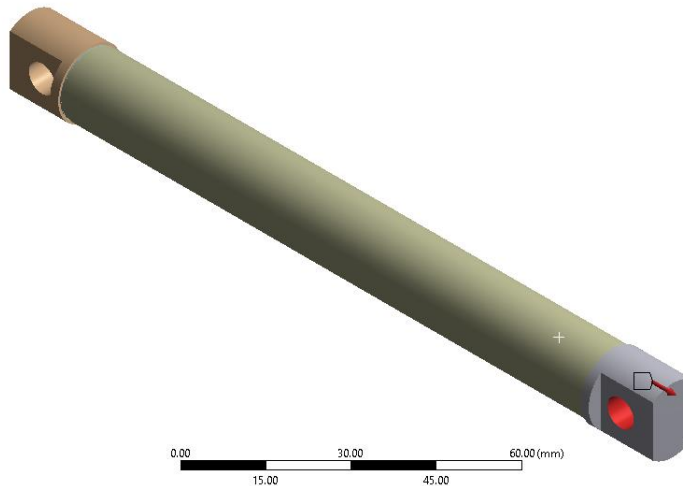


figure 75 Force applied

A: EF-4-45
Equivalent Stress
Type: Equivalent (von-Mises) Stress
Unit: MPa
Time: 1
Custom Obsolete
7/3/2024 10:54 PM



figure 76 Simulation correlation with testing

8.3 Testing conclusions

The simulation results plotted in figure 76 indicates a maximum stress value of 44.839 MPa. However, this value is disregarded as it is considered an anomaly due to meshing issues and does not correlate with the rest of the simulation results. The actual maximum stress is found at the edge of the adhesive. As it can be observed in the plot, the maximum stress is 32.315 MPa at one end-fitting and 27.416 MPa at the other end-fitting.

The maximum stress is very close to the maximum shear stress of 31MPa, meaning that the model predicted the load at which the adhesive was going to fail.

When the suspension arm was tested one end-fitting failed at this load, while the other remained adhered, as presented in figure 77. These results correlate with the experimental testing, validating the accuracy of the simulation model.



figure 77 Suspension arm before testing

9. FUTURE PROJECTS

This chapter outlines proposals for future projects to pursue:

1. Develop a computational code to calculate the maximum, minimum, and average values of the Von-Mises stress distribution for this design with adhesive length and adhesive thickness as variables.
2. Develop methodology to improve the bonding process ensuring concentricity between the aluminum end-fitting and the carbon fiber tube and control the glue gap by using glue rails and shim dots.
3. Use the information of this project to design the end-fitting of a carbon fiber rowing paddle
4. Use the information of this project to design the end-fitting of a bicycle seat post with a carbon fiber spaceframe.
5. Simulate the adhesive performance under fatigue loads and do testing to validate the simulations.

10. References

- [SAVA10a] Savage, G. (2010). Formula 1 composites engineering. *Engineering Failure Analysis**, 17(1), 92-115. <https://10.1016/j.engfailanal.2009.04.014>
- [SAVA07] Savage, G. (2007). Failure prevention in bonded joints on primary load bearing structures. *Engineering Failure Analysis**, 14(2), 321-348. <https://10.1016/j.engfailanal.2005.11.013>
- [SAVA10b] Savage, G. (2010). Dealing with crisis – solving engineering failures in formula 1 motor racing. *Engineering Failure Analysis**, 17(4), 760-770. <https://10.1016/j.engfailanal.2009.08.009>
- [TSER22] Tserpes, K., Barroso-Caro, A., Carraro, P. A., Beber, V. C., Floros, I., Gamon, W., Kozłowski, M., Santandrea, F., Shahverdi, M., Skejić, D., Bedon, C., & Rajčić, V. (2022). A review on failure theories and simulation models for adhesive joints. *The Journal of Adhesion**, 98(12), 1855-1915. <https://10.1080/00218464.2021.1941903>
- [RZAD21] Rządkowski, W., Tracz, J., Cisowski, A., Gardyjas, K., Groen, H., Palka, M., & Kowalik, M. (2021). Evaluation of bonding gap control methods for an epoxy adhesive joint of carbon fiber tubes and aluminum alloy inserts. *Materials**, 14(8), 1977. <https://10.3390/ma14081977>
- [DEQU21] de Queiroz, H. F. M., Banea, M. D., & Cavalcanti, D. K. K. (2021). Adhesively bonded joints of jute, glass and hybrid jute/glass fibre-reinforced polymer composites for automotive industry. *Applied Adhesion Science**, 9(1). <https://10.1186/s40563-020-00131-6>
- [FAB23] Fab, T. (2023). Composites in the automotive industry. *Tech Fab**, 1.
-

- [FARI21] Farish, M. (2021). Thinking outside the box: lightweight battery enclosures.
- [PARK24] Parker, L. (2024). What is an F1 monocoque?
- [MEMO23] Memon, O. (2023). Simple flying. Retrieved from <https://simpleflying.com/composite-materials-airbus-a350-gamechanger/#:~:text=Most%20of%20the%20>
- [ICON23] ICON. (2023). ICON A5 aircraft. (ICON). Retrieved from <https://icona5-aircraft.com/#: https://icona5-aircraft.com/#>
- [MELE19] Melero Herranz, & Víctor. Análisis comparativo de configuraciones de suspensión para un monoplaza tipo FSAE. <https://doi.org/10.35537/10915/88833>
- [GRAN17] Granell, I. Composite wishbones for FS school of engineering, computing and mathematics.
- [FANN16] Fanni, S., & Jweda, F. (2016). Design of carbon fibre composite driveshaft end fittings and adhesive joint for motorsport applications. KTH, Skolan för teknikvetenskap (SCI).
- [BRIA23] Briales, A. H.-R. (2023). Design and manufacture of a Formula Student Suspension. Madrid: Universidad Pontificia Comillas.
- [HE11] He, X. (2011). A review of finite element analysis of adhesively bonded joints. *International Journal of Adhesion and Adhesives*, 31(4), 248-264. <https://10.1016/j.ijadhadh.2011.01.006>
- [ROSA21] Rosas, M. F. M. O., Campilho, R. D. S. G., & Moreira, R. D. F. (2021). Numerical analysis of geometrical modification combinations of the
-

- tensile strength of tubular adhesive joints. **Procedia Structural Integrity**, 33, 115-125. <https://10.1016/j.prostr.2021.10.016>
- [VOLK38] Volkersen, O. (1938). The rivet load distribution in lap-joints with members of constant thickness subjected to tension. **Luftfahrtforschung**, 15, 41-47.
- [GOLA44] Goland, M., & Reissner, E. (1944). The stresses in cemented joints.
- [HART73] Hart-Smith, L. J. (1973). No title. **Adhesive-Bonded Single-Lap Joints**.
- [ADAM96] Adams, R. D., & Davies, R. (1996). Strength of joints involving composites. **The Journal of Adhesion**, 59(1-4), 171-182.
- [ZHAO09] Zhao, B., & Lu, Z. (2009). A two-dimensional approach of single-lap adhesive bonded joints. **Mechanics of Advanced Materials and Structures**, 16(2), 130-159.
- [YOU07] You, M., Yan, Z., Zheng, X., Yu, H., & Li, Z. (2007). A numerical and experimental study of gap length on adhesively bonded aluminum double-lap joint. **International Journal of Adhesion and Adhesives**, 27(8), 696-702.
- [CAMP12] Campilho, R. D., Banea, M. D., Neto, J., & Da Silva, L. (2012). Modelling of single-lap joints using cohesive zone models: Effect of the cohesive parameters on the output of the simulations. **The Journal of Adhesion**, 88(4-6), 513-533.
- [KIM92] Kim, K. S., Kim, W. T., & Jun, E. J. (1992). Optimal tubular adhesive-bonded lap joint of the carbon fiber epoxy composite shaft. **Composite Structures**, 21(3), 163-176.
-

- [HIPO84] Hipol, P. J. (1984). Analysis and optimization of a tubular lap joint subjected to torsion. **Journal of Composite Materials**, 18(4), 298-311.
- [SANC03] Sancaktar, E., & Nirantar, P. (2003). Increasing strength of single lap joints of metal adherends by taper minimization. **Journal of Adhesion Science and Technology**, 17(5), 655-675.
- [HOSS07] Hosseinzadeh, R., Shahin, K., & Taheri, F. (2007). A simple approach for characterizing the performance of metallic tubular adhesively-bonded joints under torsion loading. **Journal of Adhesion Science and Technology**, 21(16), 1613-1631.
- [MANU07] Manual, N. (2007). No title. **Design and Testing of Bonded and Bolted Joints**.
- [GRAN09] Grant, L., Adams, R. D., & da Silva, L. F. (2009). Experimental and numerical analysis of single-lap joints for the automotive industry. **International Journal of Adhesion and Adhesives**, 29(4), 405-413.
- [LILJ06] Liljedahl, C., Crocombe, A. D., Wahab, M. A., & Ashcroft, I. A. (2006). Damage modelling of adhesively bonded joints. **International Journal of Fracture**, 141, 147-161.
- [PERE10] Pereira, A. M., Ferreira, J. M., Antunes, F. V., & Bártolo, P. J. (2010). Analysis of manufacturing parameters on the shear strength of aluminium adhesive single-lap joints. **Journal of Materials Processing Technology**, 210(4), 610-617.
- [JEN10] Jen, Y., & Ko, C. (2010). Evaluation of fatigue life of adhesively bonded aluminum single-lap joints using interfacial parameters. **International Journal of Fatigue**, 32(2), 330-340.
-

- [JEN09] Jen, Y., Ko, C., & Lin, H. (2009). Effect of the amount of adhesive on the bending fatigue strength of adhesively bonded aluminum honeycomb sandwich beams. **International Journal of Fatigue**, 31(3), 455-462.
- [ADAM87] Adams, R. D., & Harris, J. A. (1987). The influence of local geometry on the strength of adhesive joints. **International Journal of Adhesion and Adhesives**, 7(2), 69-80.
- [ADAM74] Adams, R. D., & Peppiatt, N. A. (1974). Stress analysis of adhesive-bonded lap joints. **Journal of Strain Analysis**, 9(3), 185-196.
- [CORN53] Cornell, R. W. (1953). Determination of stresses in cemented lap joints.
- [DEMO24] demográfico, M. p. (2024). Emisiones de gases de efecto invernadero en España. Ministerio para la transición ecológica y el reto demográfico.
- [IKAB23] ikabon. (2023). Challenges in machining carbon fiber and how to overcome them. **iKabon**, 1.
- [METF23] MetalFacts. (2023). Aluminum 7075 T6. **Metal Facts**, 1.

ANNEX I SUSTAINABLE DEVELOPMENT GOALS

The sustainable development goals are a calls for action by all countries to tackle climate change and to improve education, health, reduce inequality.

This agenda was adopted by all United Nation Member States in 2015 and contains 17 Sustainable Development Goals (SDGs), which are shown in figure 78.



figure 78 Sustainable Development Goals

Sustainable Development Goals aligned with this project

This project aligns with the objectives outlined in this section, which are shown in figure 79.



figure 79 Alignment with the Sustainable Development Goals

The manufacturing guide presented in this project takes the health and safety of the manufacturer seriously, aligning with Objective **Number 3, "Good Health and Well-Being."** Manufacturing a suspension arm as described in this work involves machining carbon fiber and using structural adhesive. Machining carbon fiber generates dust particles that pose serious health risks if they come into contact with the skin or are inhaled, potentially causing long-term health problems, skin irritation, and respiratory issues. It is crucial to take the necessary safety precautions when machining carbon fiber (ikabon, 2023).

Structural adhesives also pose significant health risks when used inappropriately, potentially causing skin and eye irritation, respiratory problems, and reproductive effects. The adhesive manufacturer warns users with the CLP hazard symbols mentioned in figure 80 that using this adhesive can be hazardous to the ozone layer and can cause serious health problems.



figure 80 CLP hazard symbols

Secondly, it aligns with goal **number 4 "Quality education"**. This project will serve as a complete guide for future Formula Student team members, and contribute to their education as engineers. To achieve quality education for all reaffirms the belief that education is the most powerful vehicle for sustainable development.

This project clearly contributes to goal **number 9 "industry, innovation and infrastructure"**. This work focuses on creating a guide for designing and manufacturing a suspension system, which have a direct implication in the motorsport industry, but the results from this project can be used in a wide range of products where metal and composites materials need to be joined. A clear example is the development of aircrafts made of aluminum and composites. This work can also be used for the manufacturing of carbon fiber rowing paddles.

Objective **number 12, "Responsible Consumption and Production,"** has a clear influence on this project. Following the guide developed in this project will result in reduced material consumption of metal and adhesives. Achieving economic growth and sustainable development requires changing the way products are manufactured and resources are consumed. Developing a simulation model that correlates with empirical testing eliminates the need to test the suspension arm for every design iteration, drastically reducing the consumption and production of the materials used and reduce waste.

Finally, it aligns with the objective **number 13 "climate action"**, which follows the same principle as the previous objective explained. Reducing adhesive usage and waste have

an impact on our environment. Spain is experiencing drastic effects of climate change, and Greenhouse emissions are more than 15% higher than in 1990. Global warming is causing irreversible consequences in our country (demográfico, 2024). figure illustrates the Greenhouse emissions evolution in Spain through out the years measured in Mt of CO₂.

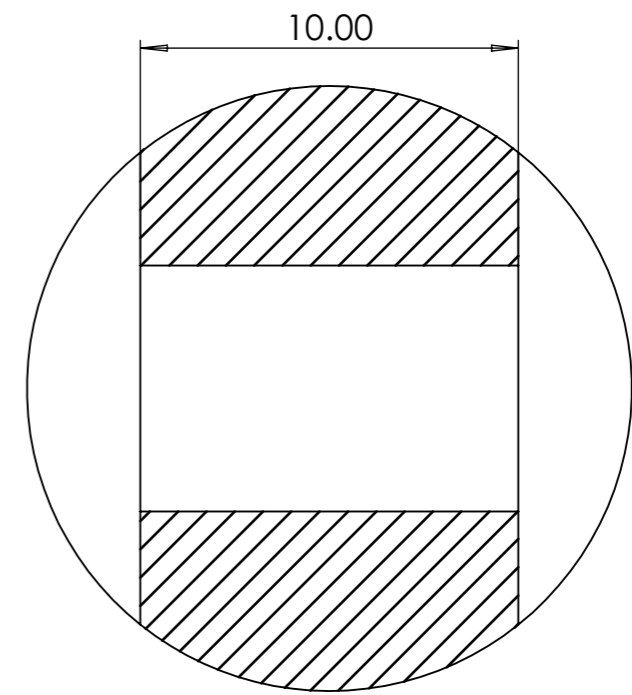
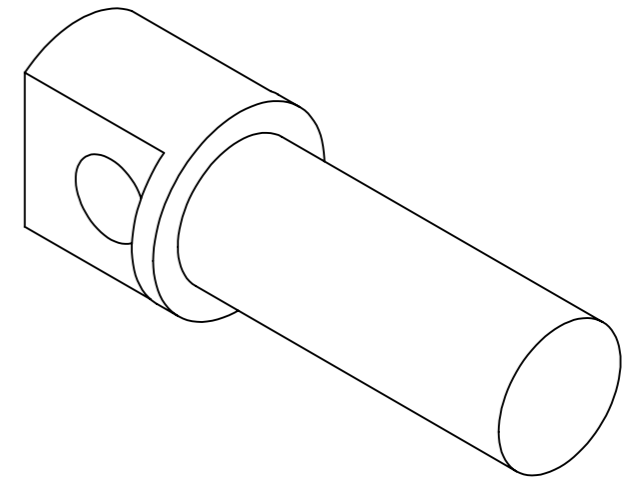
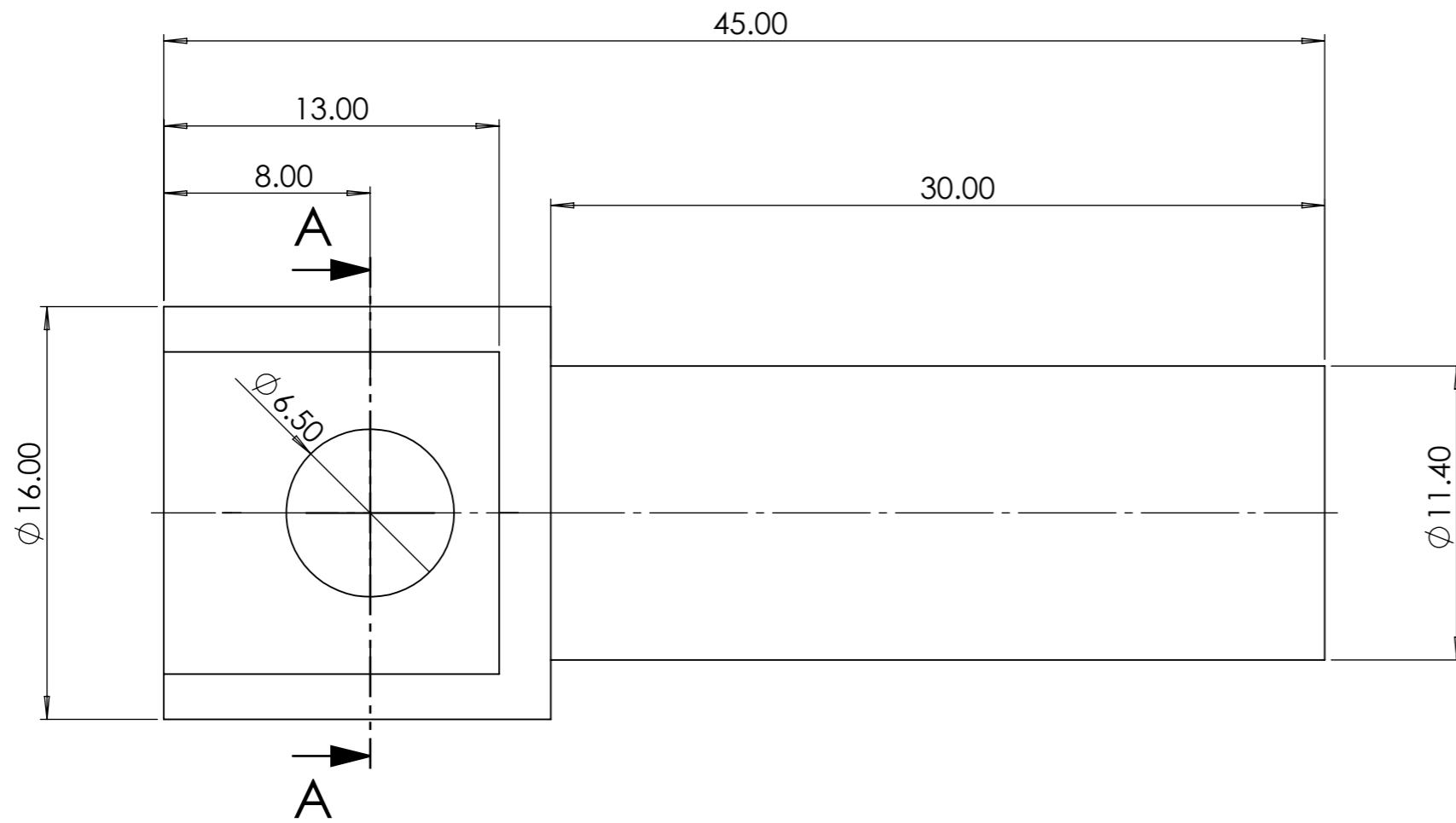
1990	2005	2008	2010	2013	2014	2015	2016	2017	2018
289,4	443,4	413,0	358,9	324,7	326,8	338,3	326,9	340,3	334,3
MtCO ₂ eq									

figure 81 Greenhouse emissions in Spain per years in Mt CO₂


ANNEX II DRAWINGS

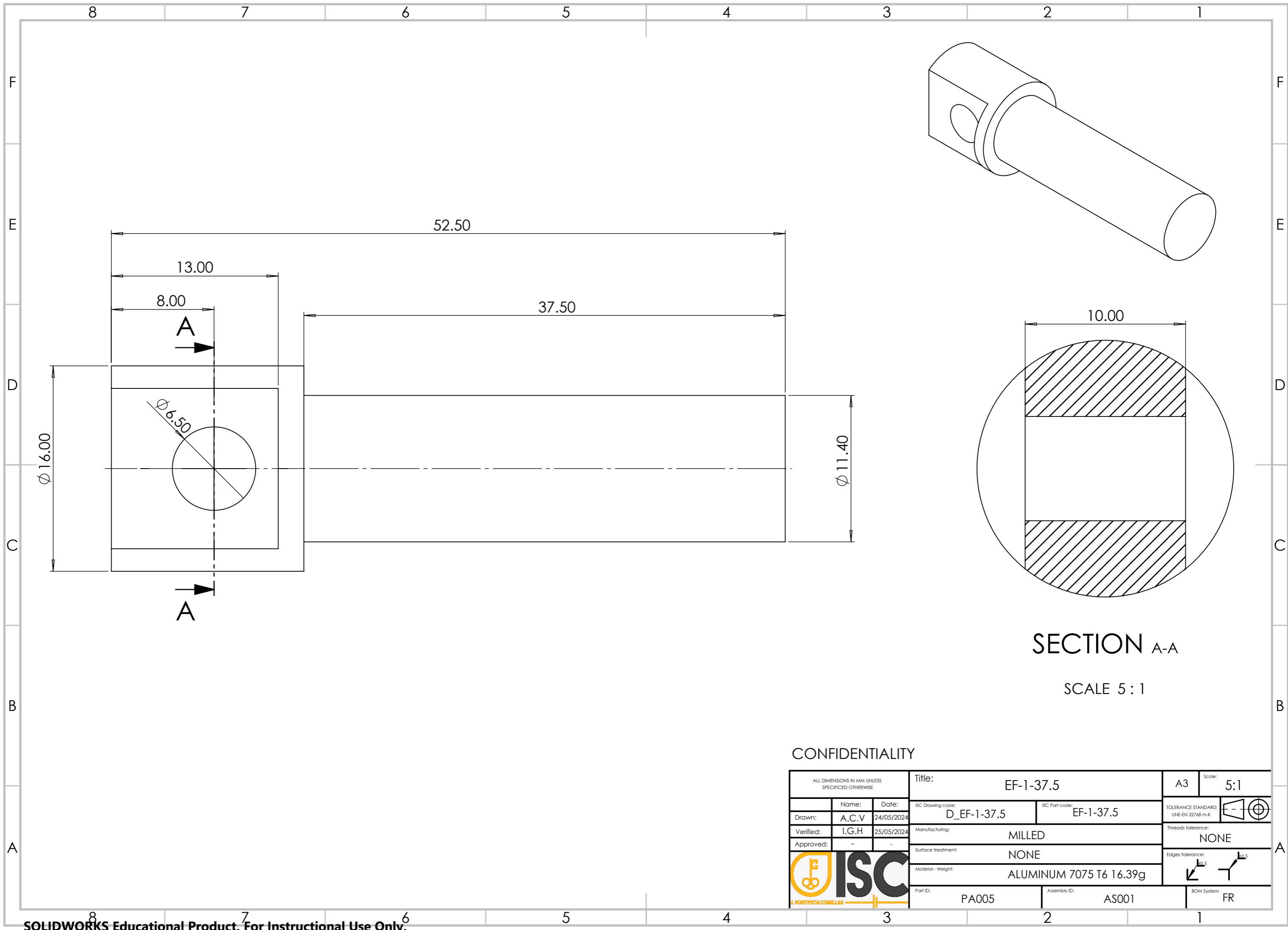
This annex presents the drawings for the following designs:

- EF-1-30
- EF-1-37.5
- EF-1-45
- EF-2-45-0.15
- EF-3-45-0.60
- EF-5-45



CONFIDENTIALITY


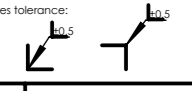
ALL DIMENSIONS IN MM UNLESS SPECIFIED OTHERWISE			Title: EF-1-30		A3	Scale: 5:1
Drawn:	Name: A.C.V	Date: 24/05/2024	ISC Drawing code: D_EF-1-30	ISC Part code: EF-1-30	TOLERANCE STANDARD: UNE-EN 22768 m-K	
Verified:	I.G.H	25/05/2024	Manufacturing: MILLED		Threads tolerance: NONE	
Approved:	-	-	Surface treatment: NONE		Edges tolerance: ± 0.5	
			Material - Weight: ALUMINUM 7075 T6 14.31g		BOM System: FR	
			Part ID: PA005	Assembly ID: AS001		

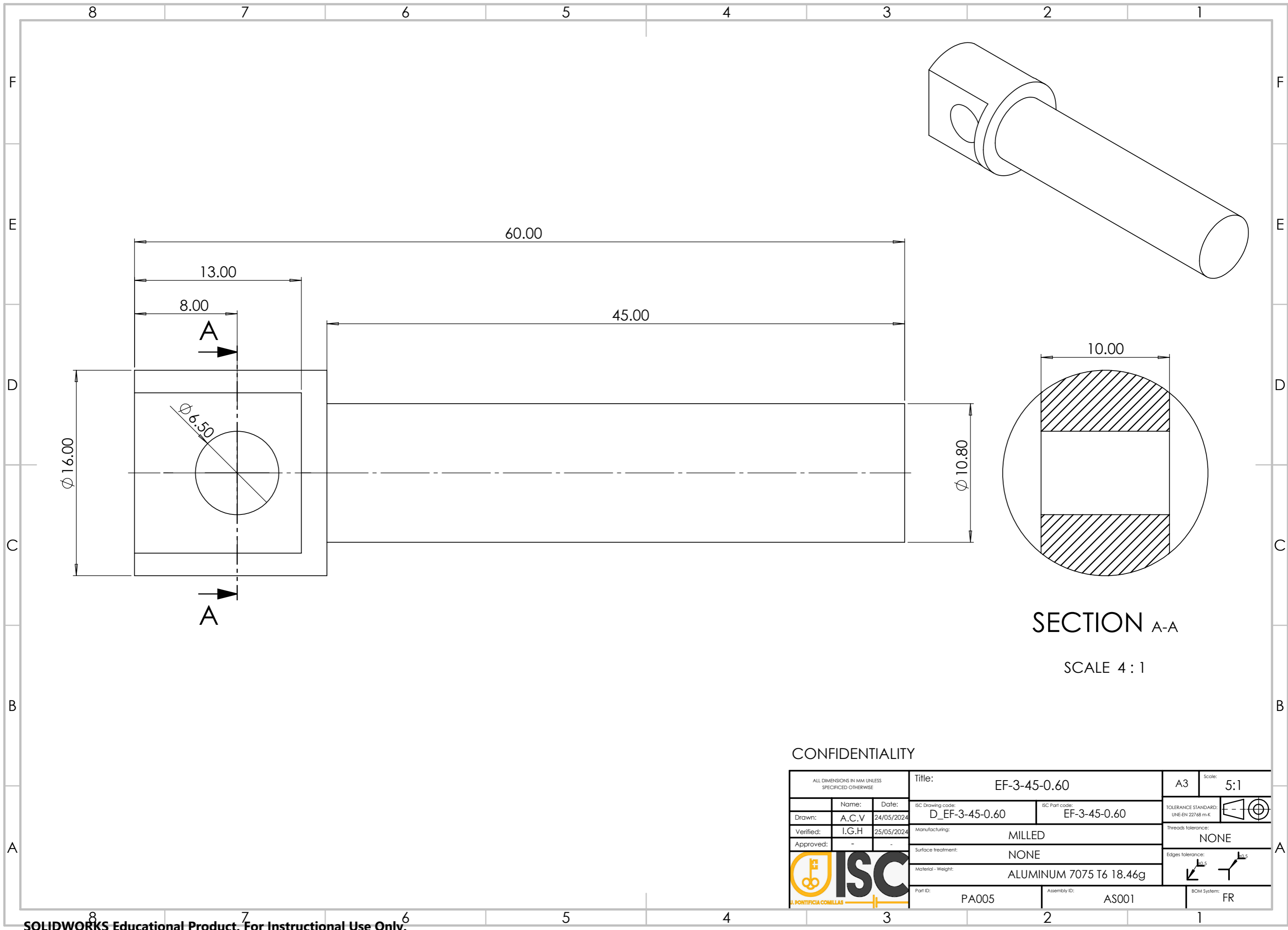


SECTION A-A

SCALE 5 : 1

CONFIDENTIALITY


ALL DIMENSIONS IN MM UNLESS SPECIFIED OTHERWISE			Title: EF-1-37.5		A3	Scale: 5:1
Drawn:	Name: A.C.V	Date: 24/05/2024	ISC Drawing code: D_EF-1-37.5	ISC Part code: EF-1-37.5	TOLERANCE STANDARD: UNE-EN 22768 m-K	
Verified:	I.G.H	25/05/2024	Manufacturing: MILLED		Threads tolerance: NONE	
Approved:	-	-	Surface treatment: NONE		Edges tolerance: ± 0.5	
			Material - Weight: ALUMINUM 7075 T6 16.39g			
			Part ID: PA005	Assembly ID: AS001	BOM System: FR	

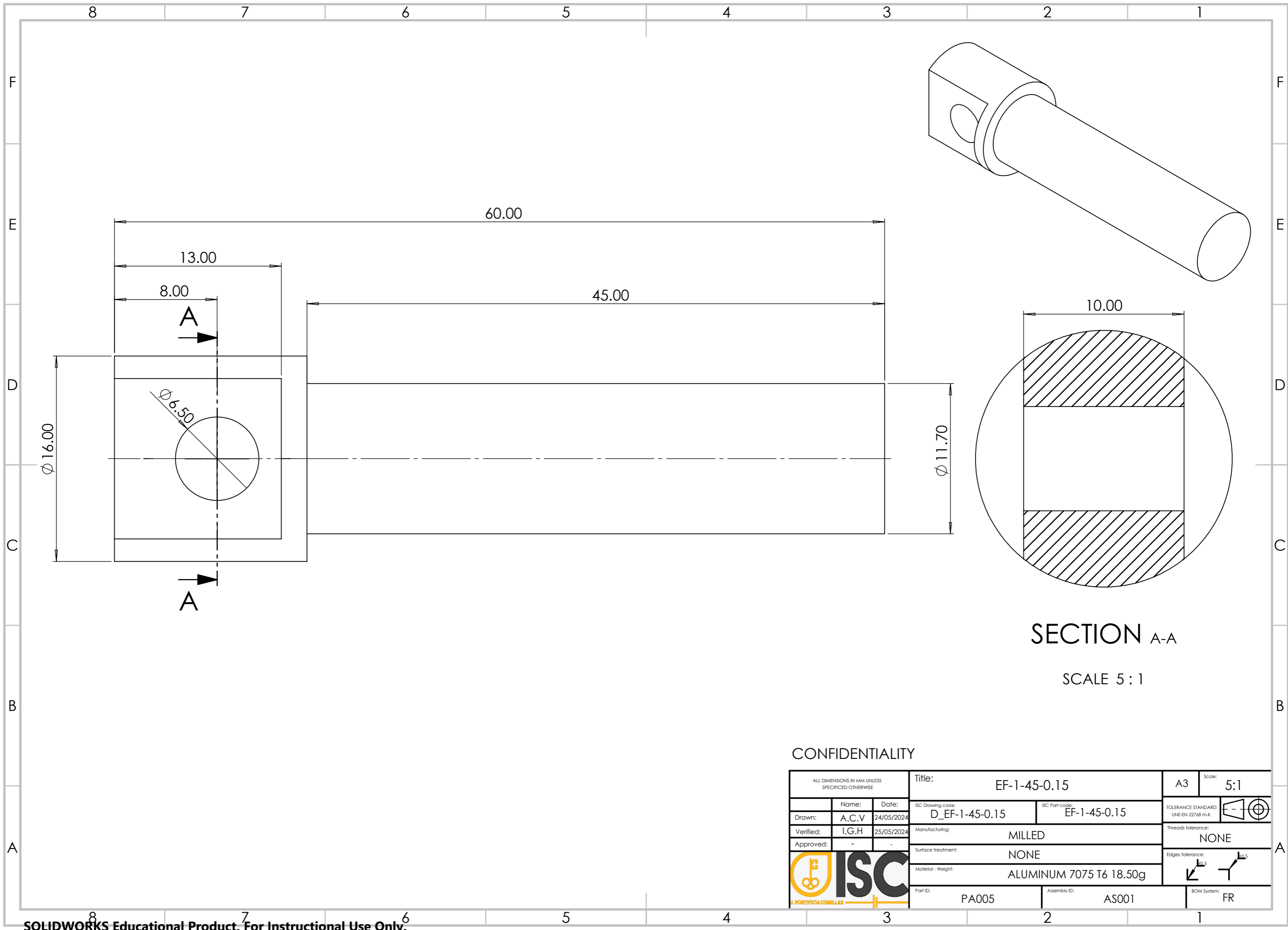


SECTION A-A

SCALE 4 : 1


CONFIDENTIALITY

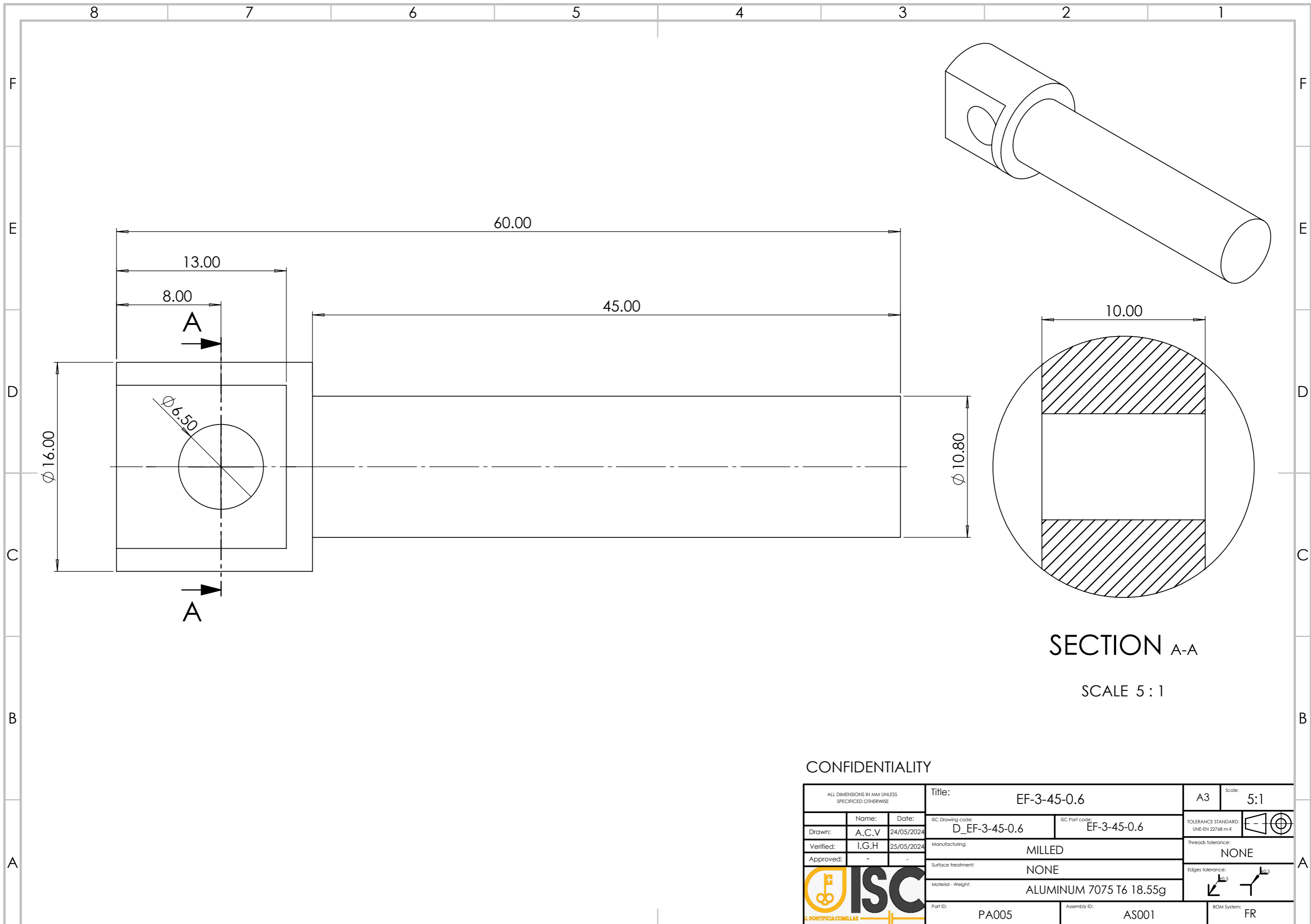
ALL DIMENSIONS IN MM UNLESS SPECIFIED OTHERWISE			Title: EF-3-45-0.60		A3	Scale: 5:1
Drawn:	Name: A.C.V	Date: 24/05/2024	ISC Drawing code: D_EF-3-45-0.60	ISC Part code: EF-3-45-0.60	TOLERANCE STANDARD: UNE-EN 22768 m-K	
Verified:	I.G.H	25/05/2024	Manufacturing: MILLED		Threads tolerance: NONE	
Approved:	-	-	Surface treatment: NONE		Edges tolerance: $\sqrt{R_0.5}$ $\sqrt{R_0.5}$	
			Material - Weight: ALUMINUM 7075 T6 18.46g		BOM System: FR	
			Part ID: PA005	Assembly ID: AS001		



SECTION A-A
SCALE 5 : 1


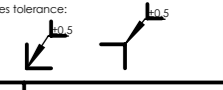
CONFIDENTIALITY

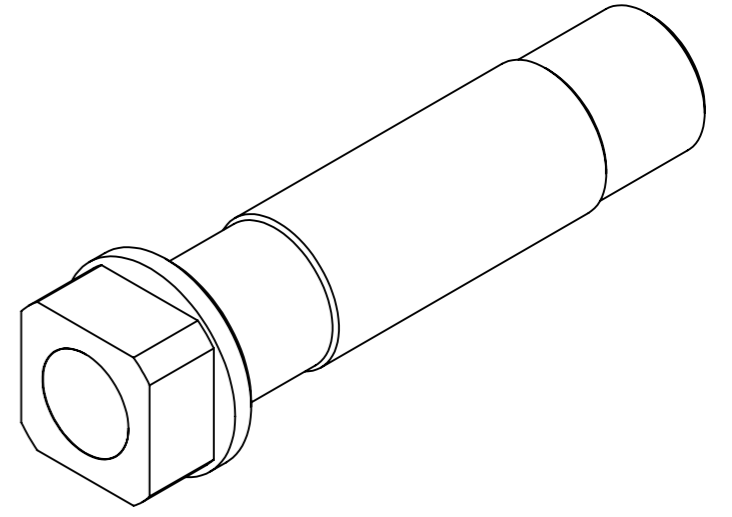
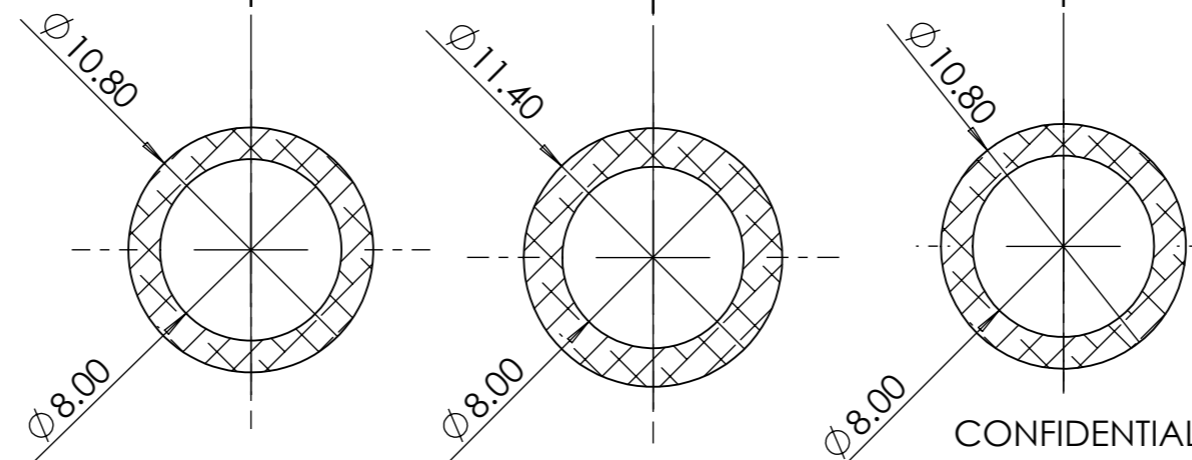
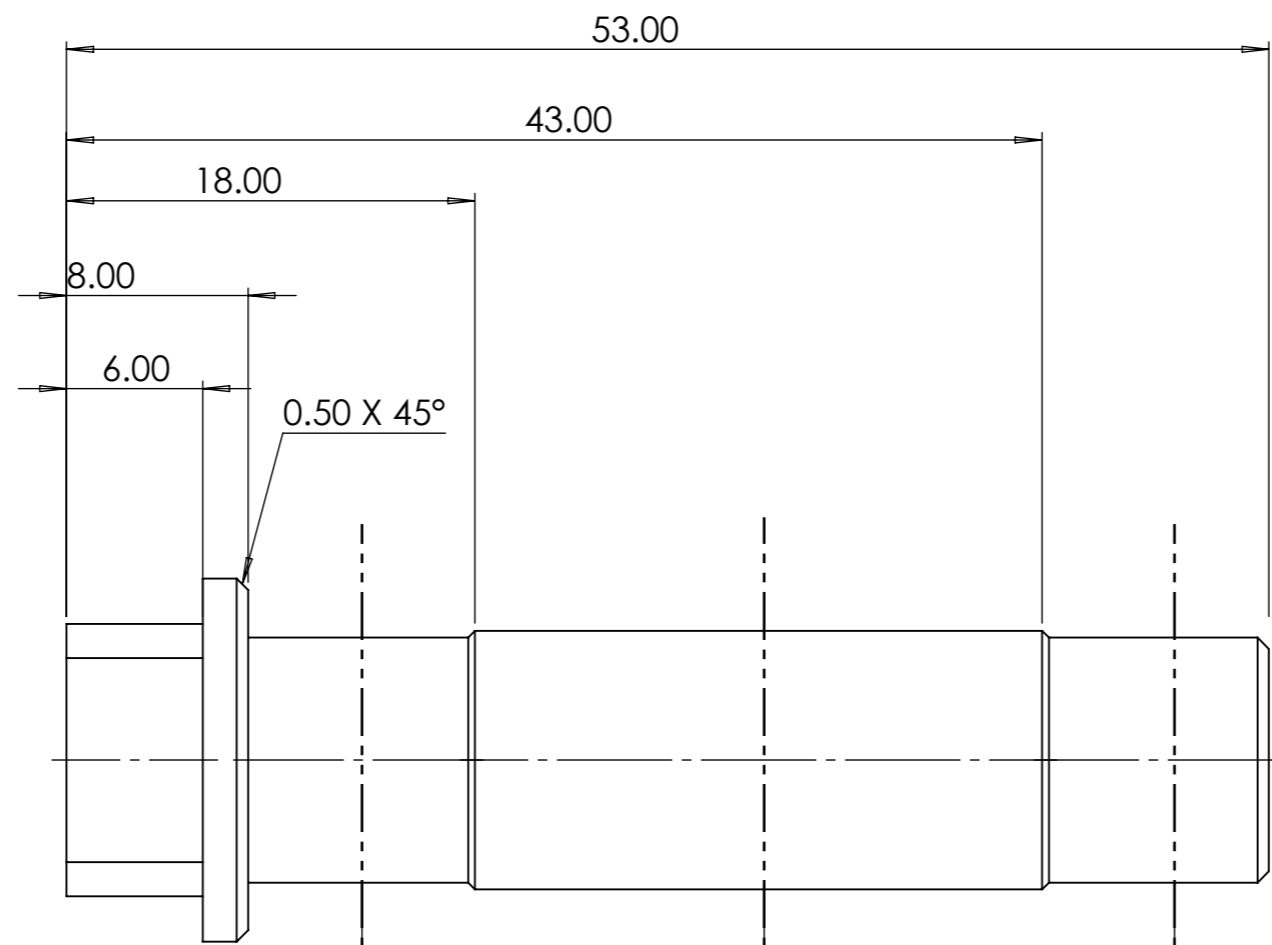
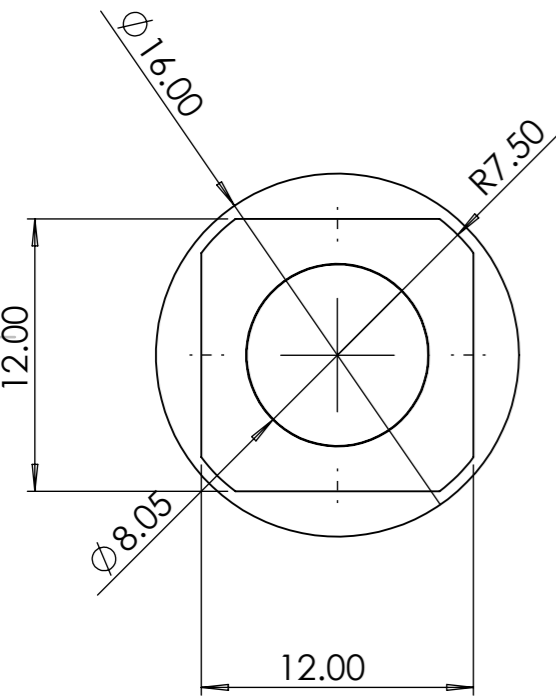
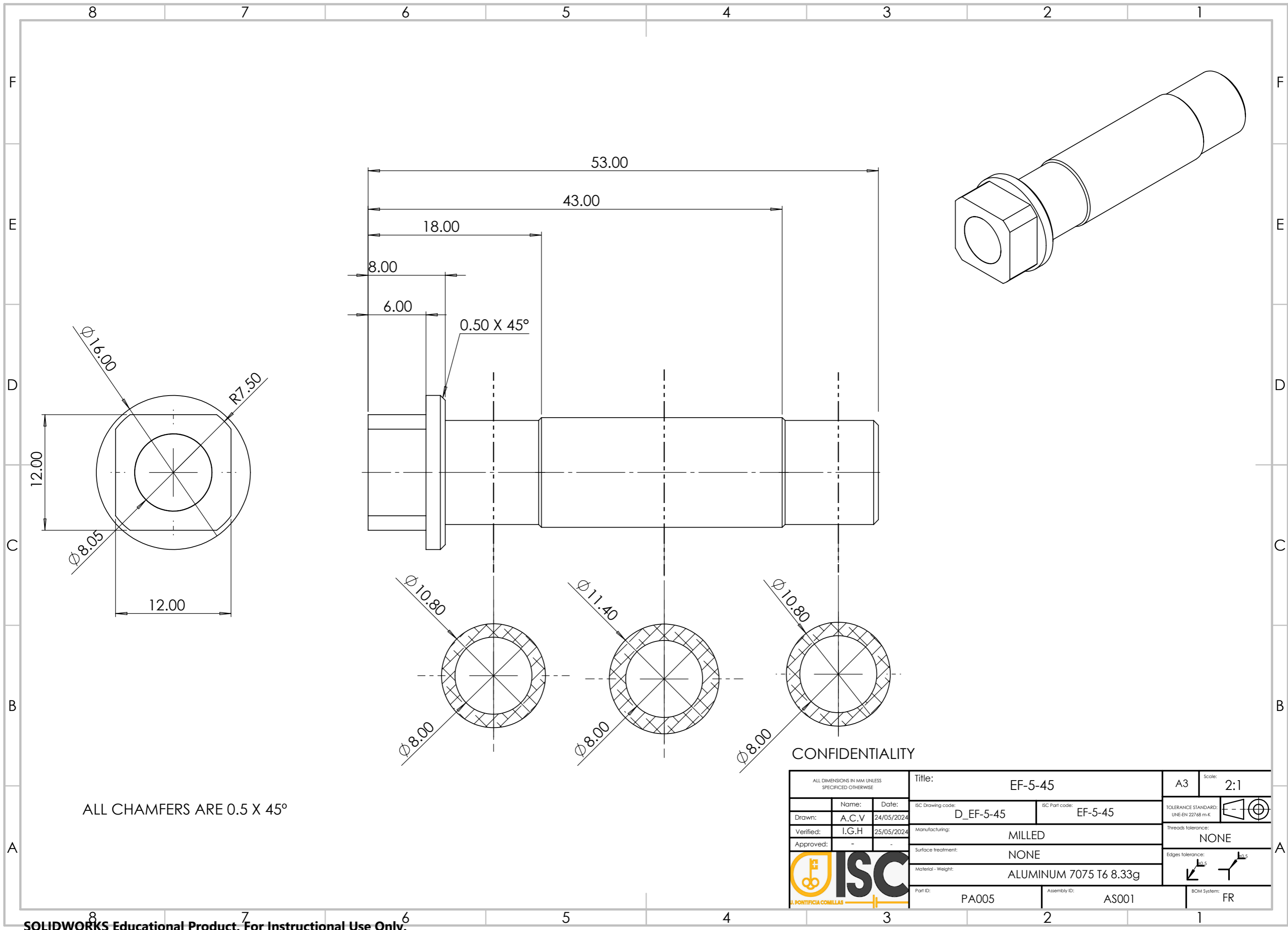
ALL DIMENSIONS IN MM UNLESS SPECIFIED OTHERWISE			Title: EF-1-45-0.15		A3	Scale: 5:1
Drawn:	Name: A.C.V	Date: 24/05/2024	ISC Drawing code: D_EF-1-45-0.15	ISC Part code: EF-1-45-0.15	TOLERANCE STANDARD: UNE-EN 22768 m-K	
Verified:	I.G.H	25/05/2024	Manufacturing: MILLED		Threads tolerance: NONE	
Approved:	-	-	Surface treatment: NONE		Edges tolerance: $\sqrt{0.5}$ $\sqrt{0.5}$	
			Material - Weight: ALUMINUM 7075 T6 18.50g		BOM System: FR	
			Part ID: PA005	Assembly ID: AS001		



SECTION A-A
SCALE 5 : 1

CONFIDENTIALITY

ALL DIMENSIONS IN MM UNLESS SPECIFIED OTHERWISE			Title: EF-3-45-0.6		A3	Scale: 5:1
Drawn:	Name: A.C.V	Date: 24/05/2024	ISC Drawing code: D_EF-3-45-0.6	ISC Part code: EF-3-45-0.6	TOLERANCE STANDARD: UNE-EN 22768 m-K	
Verified:	I.G.H	25/05/2024	Manufacturing: MILLED		Threads tolerance: NONE	
Approved:	-	-	Surface treatment: NONE		Edges tolerance: ± 0.5	
			Material - Weight: ALUMINUM 7075 T6 18.55g			
			Part ID: PA005	Assembly ID: AS001	BOM System: FR	



ALL CHAMFERS ARE 0.5 X 45°

CONFIDENTIALITY

ALL DIMENSIONS IN MM UNLESS SPECIFIED OTHERWISE			Title: EF-5-45		A3	Scale: 2:1
Drawn: A.C.V	Date: 24/05/2024	ISC Drawing code: D_EF-5-45	ISC Part code: EF-5-45		TOLERANCE STANDARD: UNE-EN 22768 m-K	
Verified: I.G.H	Date: 25/05/2024	Manufacturing: MILLED		Threads tolerance: NONE		
Approved: -	-	Surface treatment: NONE		Edges tolerance: ±0.5		
Material - Weight: ALUMINUM 7075 T6 8.33g		Part ID: PA005		Assembly ID: AS001		BOM System: FR

ANNEX III DATASHEETS

This annex presents the datasheet of:

- 3M DP420NS structural adhesive
- Carbon fiber tube provide by Clipcarbono
- Aluminum 7075 T6

Atributos de puntos

Color B	234		
Color G	234		
Color R	234		
Shape factor	15		
SIN List indicator (0-1, 1 = high risk)	0		
Tangent modulus	1,19e3		MPa

Atributos de rango

Acoustic velocity	4,96e3	-	5,21e3	m/s
Al (aluminum)	* 87,2	-	91,4	%
Bulk modulus	67	-	74	GPa
CO2 footprint, primary production (typical grade)	* 7,89	-	9,21	kg/kg
CO2 footprint, primary production (virgin grade)	* 12,7	-	14	kg/kg

Sources

Estimated from sources including Voet, van der and Oers, van, 2003; Hammond and Jones, 2008; Ecoinvent v3.7.1; Norgate, Jahanshahi, Rankin, 2007; Tharumarajah and Koltun, 2007

CO2 footprint, recycling	* 2,44	-	2,69	kg/kg
Coarse machining CO2 (per unit wt removed)	* 0,152	-	0,168	kg/kg
Coarse machining energy (per unit wt removed)	* 2,02	-	2,24	MJ/kg
Compressive strength	* 460	-	530	MPa
Cr (chromium)	0,18	-	0,28	%
Cu (copper)	1,2	-	2	%
Density	2,77e3	-	2,83e3	kg/m ³
Elastic stored energy (springs)	1,46e3	-	1,94e3	kJ/m ³
Electrical conductivity	32,5	-	33,8	%IACS
Electrical resistivity	5,1	-	5,3	μohm.cm
Elongation	2	-	10	% strain
Embodied energy, primary production (typical grade)	* 110	-	128	MJ/kg
Embodied energy, primary production (virgin grade)	* 180	-	198	MJ/kg

Sources

Estimated from sources including Institute for Prospective Technological Studies, 2005; Hekkert, 2000; Norgate, Jahanshahi, Rankin, 2007; Hammond and Jones, 2008; Ecoinvent v3.7.1; Sullivan and Gaines, 2010; Dhingra, Overly, Davis, 1999; Fthenakis, Wang, Kim, 2009

Embodied energy, recycling	* 31	-	34,3	MJ/kg
Extrusion, foil rolling CO2	* 1,57	-	1,74	kg/kg
Extrusion, foil rolling energy	* 20,9	-	23,1	MJ/kg
Extrusion, foil rolling water	* 10,5	-	15,8	l/kg
Fatigue strength at 10 ⁷ cycles	152	-	168	MPa
Fe (iron)	0	-	0,5	%
Fine machining CO2 (per unit wt removed)	* 1,2	-	1,32	kg/kg
Fine machining energy (per unit wt removed)	* 16	-	17,6	MJ/kg
Flexural modulus	* 69	-	76	GPa
Flexural strength (modulus of rupture)	* 460	-	530	MPa
Fracture toughness	26,6	-	26,8	MPa.m ^{0.5}
Galvanic potential	* -0,78	-	-0,7	V

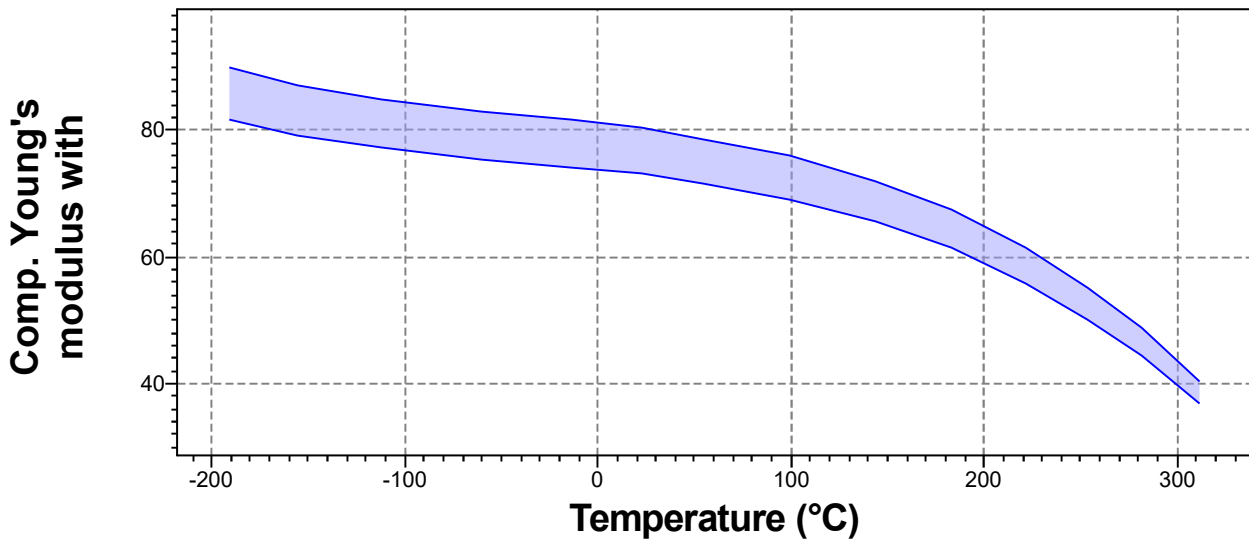
Grinding CO2 (per unit wt removed)	* 2,36	- 2,61	kg/kg
Grinding energy (per unit wt removed)	* 31,4	- 34,8	MJ/kg
Hardness - Brinell	145	- 165	HB
Hardness - Vickers	152	- 168	HV
Latent heat of fusion	384	- 393	kJ/kg
Machining speed	76,2		m/min
Maximum service temperature	80	- 100	°C
Mechanical loss coefficient (tan delta)	* 1e-4	- 0,002	
Melting point	475	- 635	°C
Metal powder forming CO2	* 1,66	- 1,83	kg/kg
Metal powder forming energy	* 20,7	- 22,9	MJ/kg
Metal powder forming water	* 22,6	- 33,9	l/kg
Mg (magnesium)	2,1	- 2,9	%
Minimum service temperature	-273		°C
Mn (manganese)	0	- 0,3	%
Non-conventional machining CO2 (per unit wt removed)	* 11,6	- 12,8	kg/kg
Non-conventional machining energy (per unit wt removed)	* 155	- 171	MJ/kg
Other	0	- 0,15	%
Poisson's ratio	0,325	- 0,335	
Price	* 5,94	- 8,02	EUR/kg
Price per unit volume	* 1,65e4	- 2,27e4	EUR/m ³
Recycle fraction in current supply	42,8	- 47,3	%
Roll forming, forging CO2	* 0,796	- 0,879	kg/kg
Roll forming, forging energy	* 10,6	- 11,7	MJ/kg
Roll forming, forging water	* 6,09	- 9,13	l/kg
Shear modulus	26	- 28	GPa
Si (silicon)	0	- 0,4	%
Specific heat capacity	913	- 979	J/kg.°C
Specific stiffness	24,6	- 27,2	MN.m/kg
Specific strength	164	- 189	kN.m/kg
Tensile strength	530	- 580	MPa
Thermal conductivity	131	- 137	W/m.°C
Thermal distortion resistance	5,51	- 5,9	MW/m
Thermal expansion coefficient	22,9	- 24,1	µstrain/°C
Thermal shock resistance	266	- 317	°C
Ti (titanium)	0	- 0,2	%
Toughness (G)	9,38	- 10,3	kJ/m ²
Vaporization CO2	* 1,16e3	- 1,28e3	kg/kg
Vaporization energy	* 1,55e4	- 1,71e4	MJ/kg
Vaporization water	* 6,46e3	- 9,69e3	l/kg
Water usage	* 1,08e3	- 1,19e3	l/kg
Wire drawing CO2	* 5,83	- 6,44	kg/kg
Wire drawing energy			

	* 77,7	- 85,9	MJ/kg
Wire drawing water	* 29,3	- 43,9	l/kg
Yield strength (elastic limit)	460	- 530	MPa
Young's modulus	69	- 76	GPa
Zn (zinc)	5,1	- 6,1	%

Datos de rangos funcionales

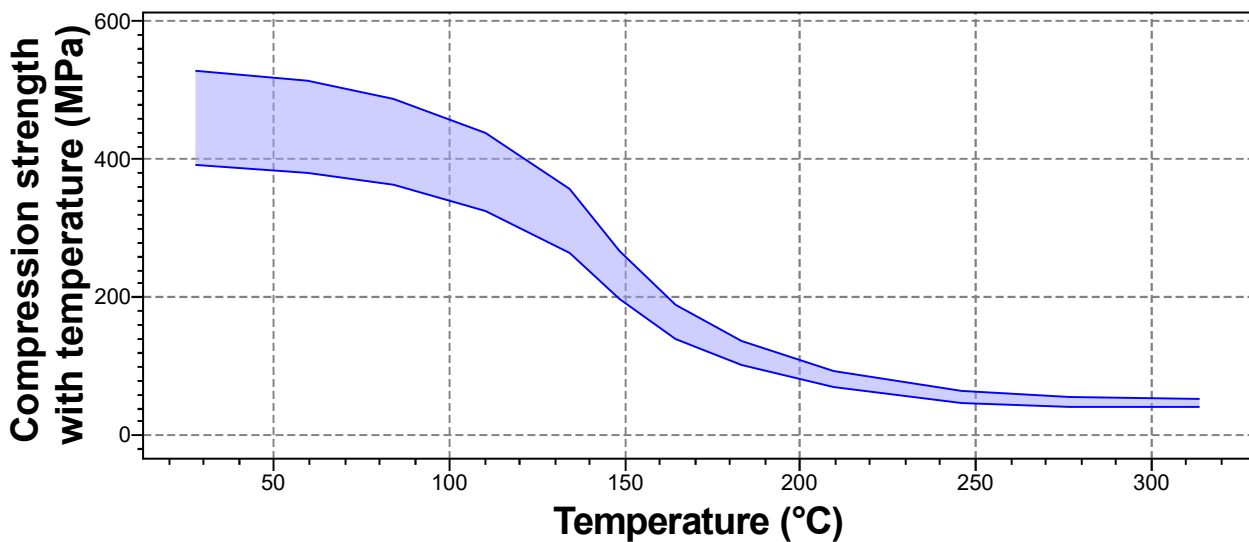
Comp. Young's modulus with temperature	73	- 80,3	GPa
--	----	--------	-----

[Parámetros:](#) Temperature = 23°C



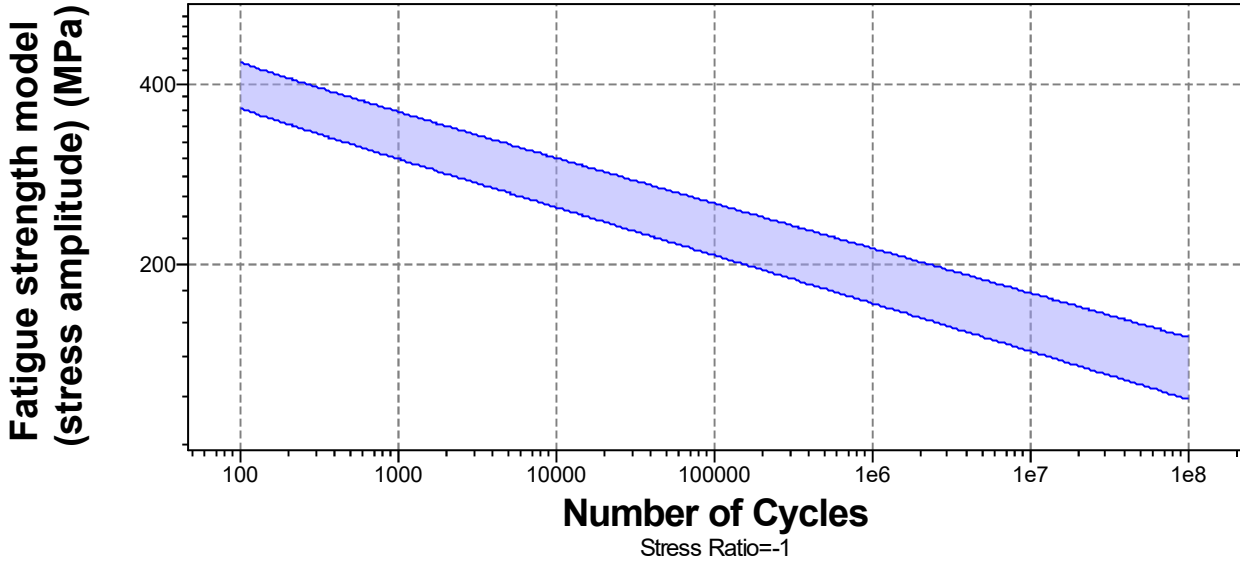
Compression strength with temperature	Fuera de rango	MPa
---------------------------------------	----------------	-----

[Parámetros:](#) Temperature = 23°C



Fatigue strength model (stress amplitude)	143	- 179	MPa
---	-----	-------	-----

[Parámetros:](#) Stress Ratio = -1, Number of Cycles = 1e7cycles

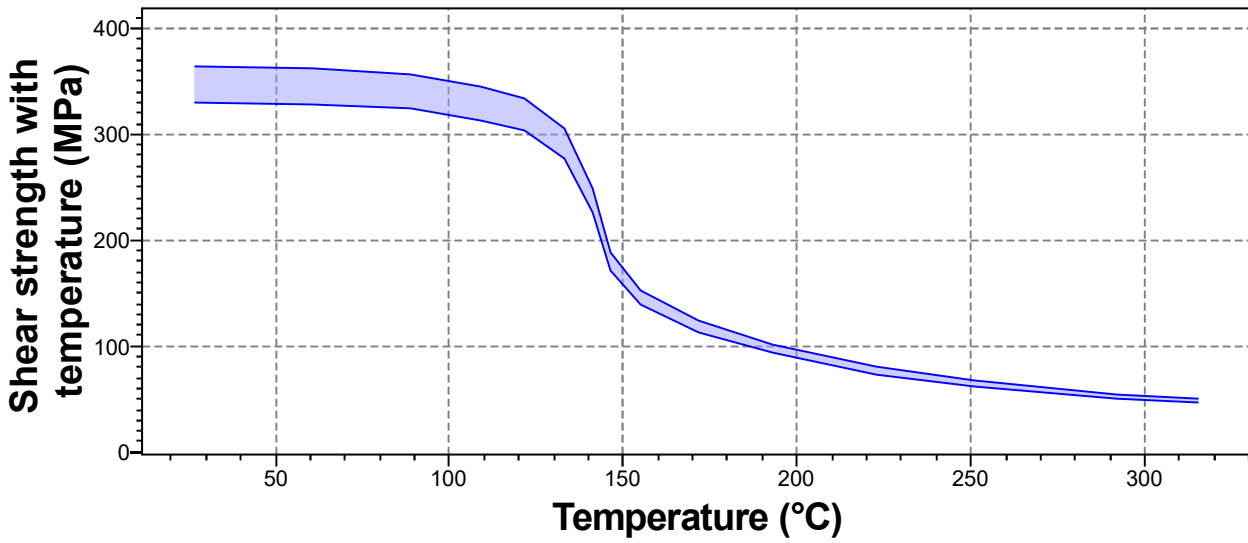


Shear strength with temperature

Fuera de rango

MPa

Parámetros: Temperature = 23°C



Tensile strength with temperature

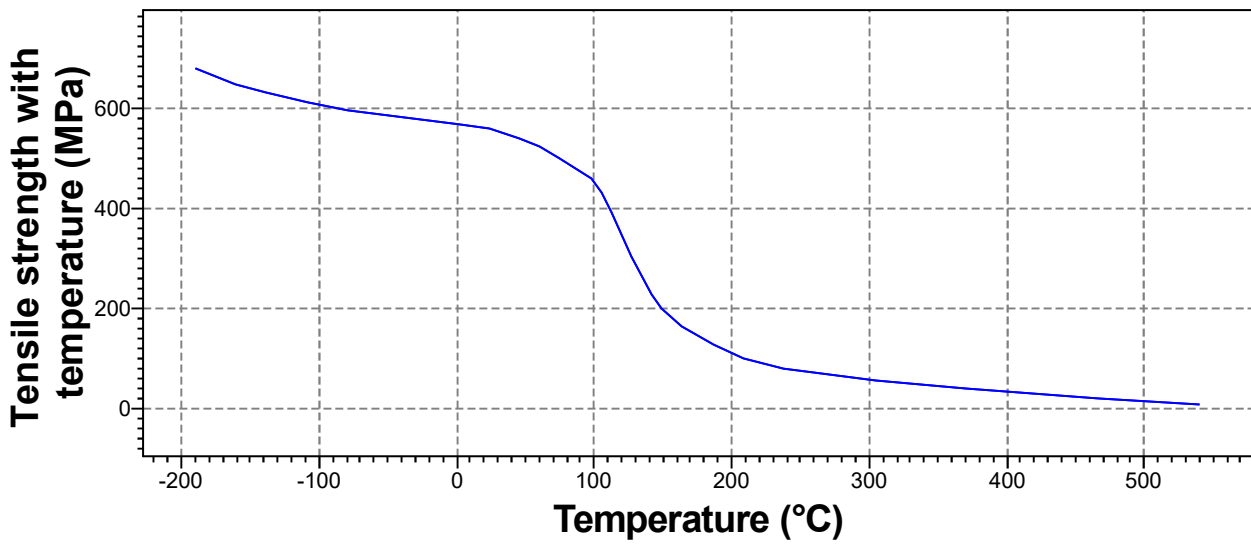
557

-

557

MPa

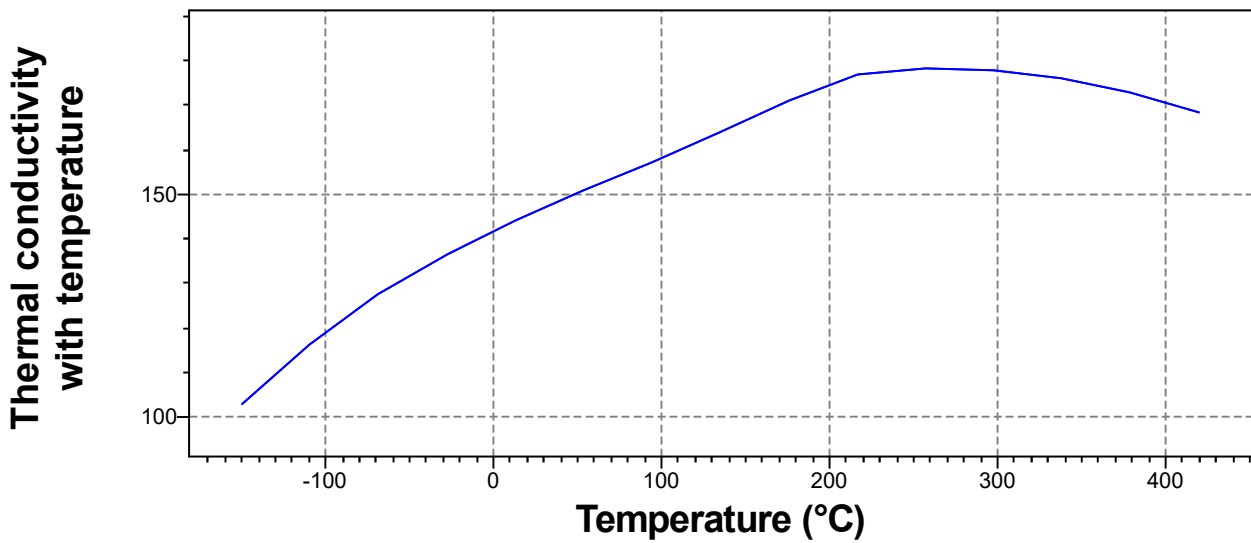
Parámetros: Temperature = 23°C



Thermal conductivity with temperature

146 - 146 W/m.°C

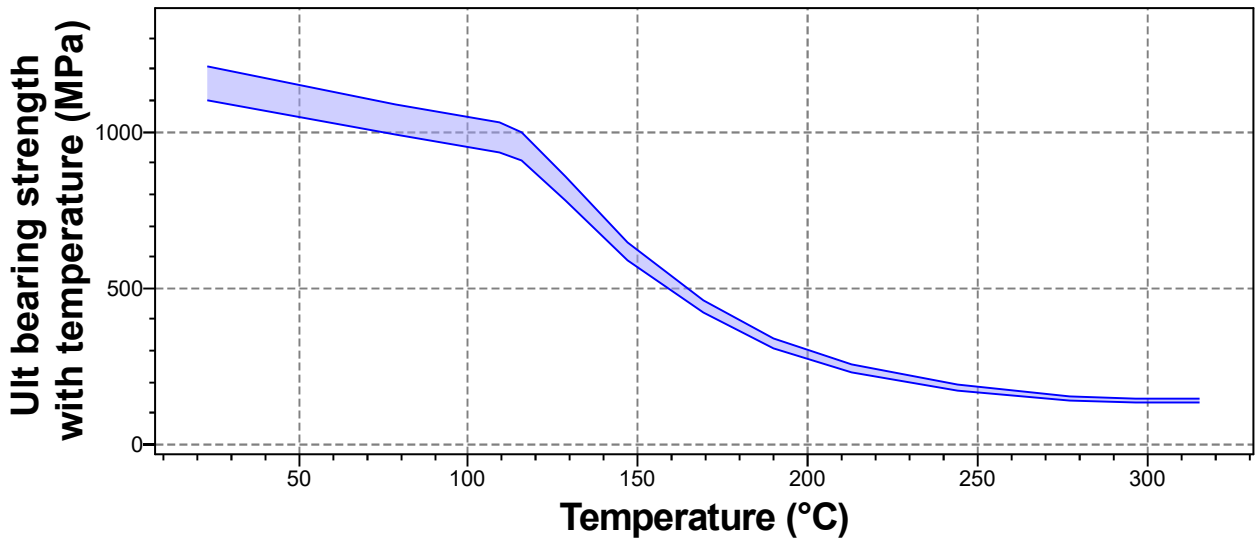
[Parámetros:](#) Temperature = 23°C



Ult bearing strength with temperature

Fuera de rango MPa

[Parámetros:](#) Temperature = 23°C

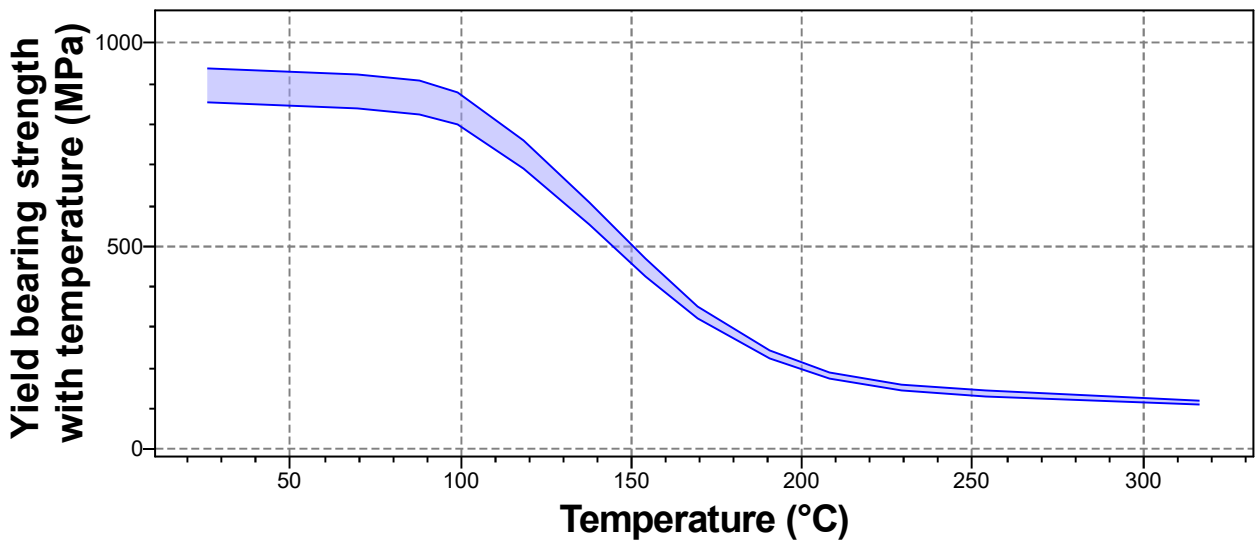


Yield bearing strength with temperature

Fuera de rango

MPa

Parámetros: Temperature = 23°C



Yield strength with temperature

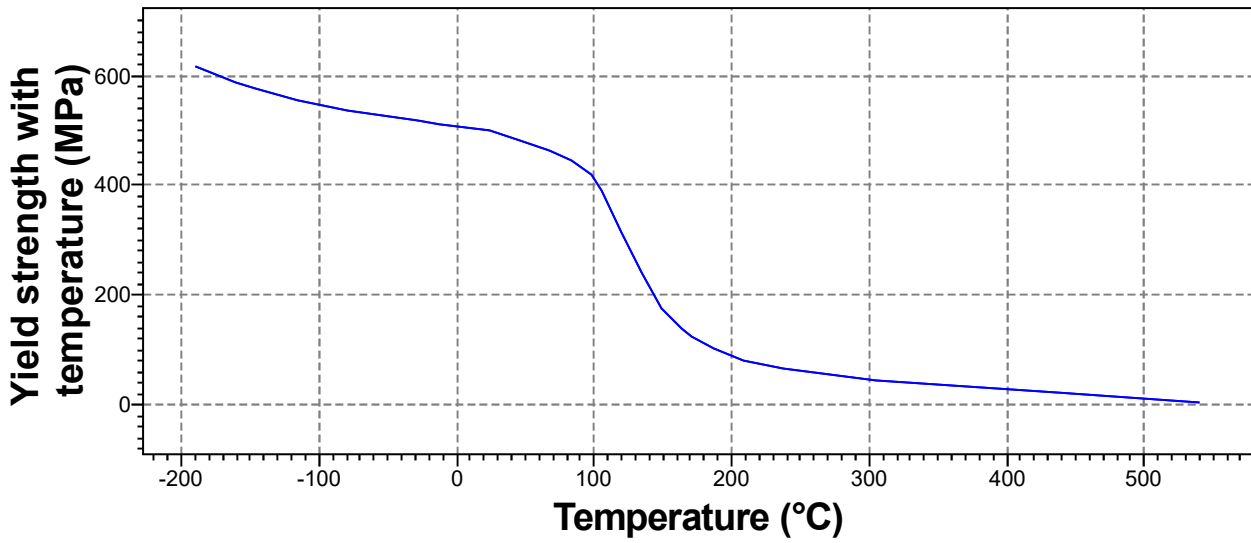
499

-

499

MPa

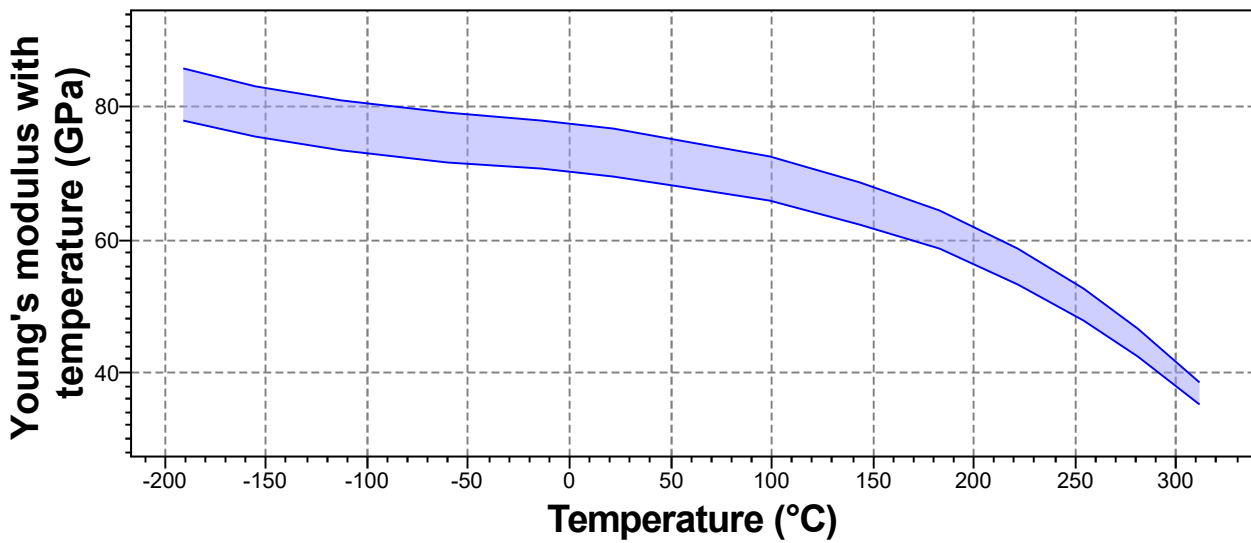
Parámetros: Temperature = 23°C



Young's modulus with temperature

69,6 - 76,6 GPa

[Parámetros:](#) Temperature = 23°C



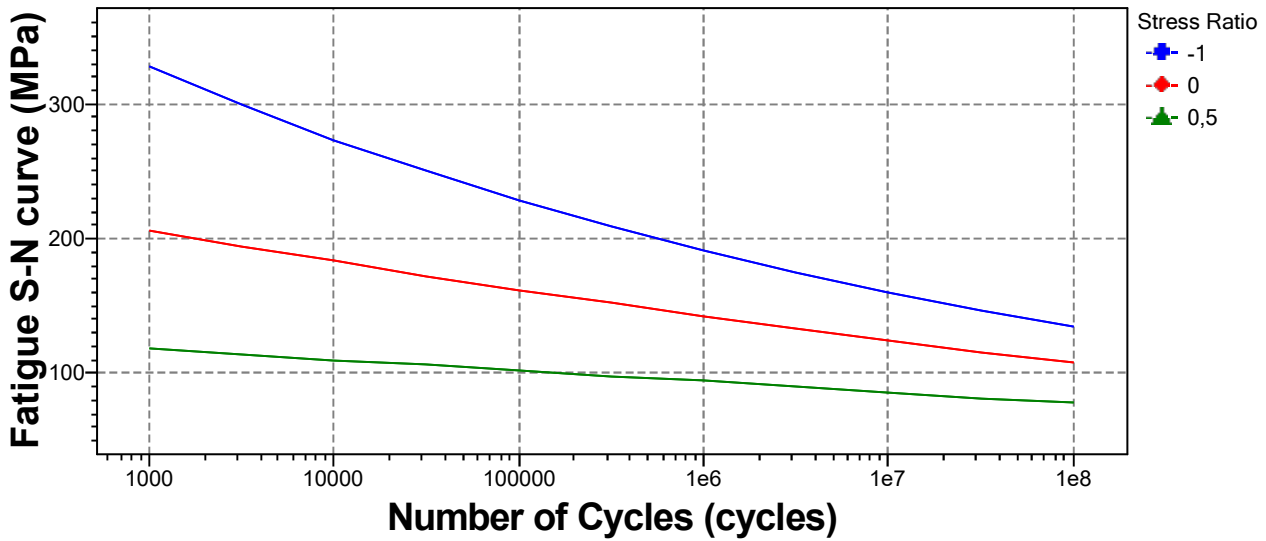
Datos de puntos funcionales

Fatigue S-N curve

160

MPa

[Parámetros:](#) Number of Cycles = 1e7cycles, Stress Ratio = -1

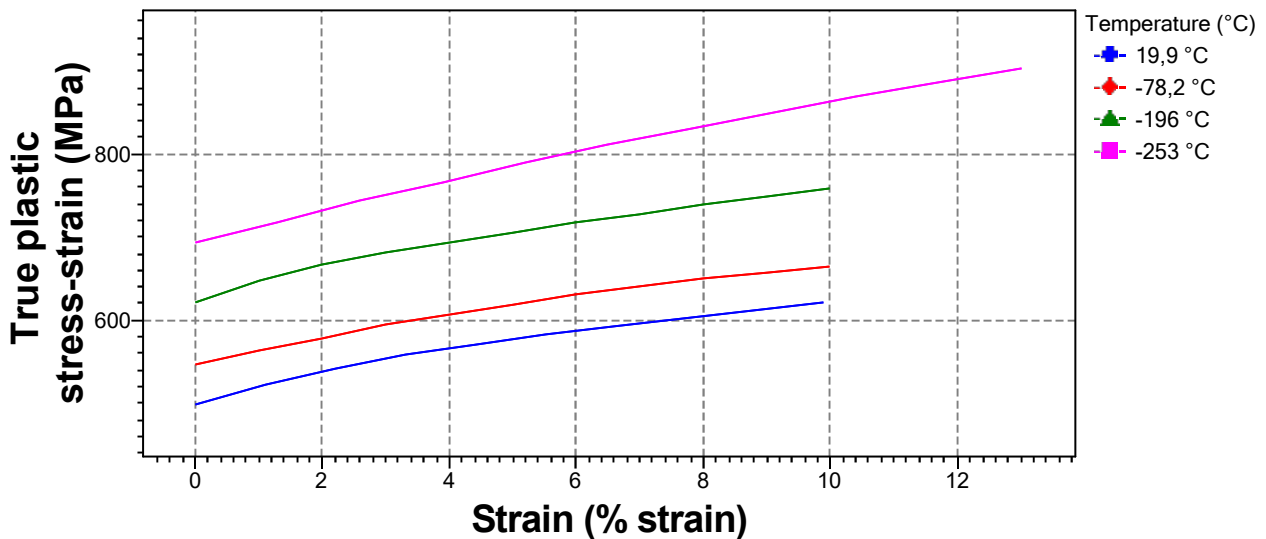


True plastic stress-strain

Fuera de rango

MPa

Parámetros: Strain = 0,1% strain, Temperature = 23°C



Atributo lógico

Biodegrade	✗
Combust for energy recovery	✗
Downcycle	✓
Included in Materials Data for Simulation	✓
Landfill	✓
Recycle	✓

Atributos discretos

Base material	Al (Aluminum)
Contains >5wt% critical elements?	Yes
Flammability	Non-flammable

Galling resistance (adhesive wear)	Limited use
Notes	
Aluminum alloys perform poorly when self-mated but can be processed without galling when mated with steels.	
Generic material class	Metal (non-ferrous)
Magnetic type	Non-magnetic
Material family	Metal (non-ferrous)
Metal casting	Unsuitable
Metal cold forming	Acceptable
Metal deep drawing	Acceptable
Metal hot forming	Excellent
Metal press forming	Acceptable
Organic solvents	Excellent
Oxidation at 500C	Unacceptable
Stress corrosion cracking	Highly susceptible
Notes	Rated in chloride; Other susceptible environments: Halide, water
Strong acids	Excellent
Strong alkalis	Unacceptable
Transparency	Opaque
UV radiation (sunlight)	Excellent
Water (fresh)	Excellent
Water (salt)	Acceptable
Weak acids	Excellent
Weak alkalis	Acceptable
Weldability	Poor
Notes	Due to its susceptibility to stress corrosion cracking, welding should be extremely limited.

Atributos de texto corto

Condition	T6 (Solution heat-treated and artificially aged)
EN name	EN AW-7075 (EN AW-Al Zn5,5MgCu)
EN number	3.4365
Materials Data for Simulation name	Aluminum alloy, wrought, 7075, T6
Record History GUID	C0692C05-6DC1-4E58-8271-DC5D9815018B
UNS number	A97075

Atributos de texto largo

Compositional summary

Al87-91 / Zn5.1-6.1 / Mg2.1-2.9 / Cu1.2-2 / Cr0.18-0.28 (impurities: Fe<0.5, Si<0.4, Mn<0.3, Ti<0.2, Other<0.15)

Designation

Aluminum, 7075, T6, wrought

Keywords

0.7075 to CSA HA.4; 0.7075 to CSA HA.5; 0.7075 to CSA HA.7; 0.7075 to CSA HA.8; 17411 to NS 17411; 1950; 2L.88 to BS 2L.88; 3.4365; 3.4365/AlZnMgCu1.5 to DIN 1725-1; 3.7552.00/AlZnMgCu0.5; 3.7553.00/AlZn5MgCu1.5 to JUS C.C2.100; 424222; 7075; 7075 to AS 1865; 7075 to AS 2848.1; 7075 to ASTM B209M; 7075 to ASTM B210M; 7075 to ASTM B211M; 7075 to ASTM B221M; 7075 to ASTM B241M; 7075 to ASTM B247M; 7075 to ASTM B316/B316M; 7075 to COPANT 862; 7075 to NF A50-411; 7075 to NF A50-451; 7075Alclad to CSA HA.4; 7175; 76528 to IS; A-Z5GU(7075); A7075BD to JIS H4040; A7075BE to JIS H4040; A7075FD to JIS H4140; A7075FH to JIS H4140; A7075P to JIS H4000; A7075S to JIS H4100; A7075TD to JIS H4080; A7075TE to JIS H4080; AlZn5.5MgCu to ISO 209-1; AlZn6Mg2Cu; AlZn6MgCu; AlZn6MgCuMn; AlZnMgCu1.5 to ONORM M3430; Alcan 75S; Alcan 75S Alclad; Alcoa 7075; Baw 7075; EN AW-7075 (EN AW-Al Zn5.5MgCu); EN AW-7075 to CEN EN 573-3; Noral M75 S; Perunal-215; UNSA97075; V95

Other notes

Prices of Aluminum alloys fluctuate greatly and are dependent on batch size, unit size, forming methods, etc.

Standards with similar compositions

- Australia:
7075 to AS 1865, 7075 to AS 2848.1
- Austria:
AlZnMgCu1.5 to ONORM M3430
- Canada:
0.7075 to CSA HA.4, 0.7075 to CSA HA.5, 0.7075 to CSA HA.7, 0.7075 to CSA HA.8, 7075Alclad to CSA HA.4
- Europe:
EN AW-7075 to CEN EN 573-3
- France:
7075 to NF A50-411, 7075 to NF A50-451
- Germany:
3.4365/AlZnMgCu1.5 to DIN 1725-1
- India:
76528 to IS
- International:
AlZn5.5MgCu to ISO 209-1
- Japan:
A7075BD to JIS H4040, A7075BE to JIS H4040, A7075FD to JIS H4140, A7075FH to JIS H4140, A7075P to JIS H4000, A7075S to JIS H4100, A7075TD to JIS H4080, A7075TE to JIS H4080
- Norway:
17411 to NS 17411
- UK:
2L.88 to BS 2L.88
- USA:
7075, 7075 to ASTM B209M, 7075 to ASTM B210M, 7075 to ASTM B211M, 7075 to ASTM B221M, 7075 to ASTM B241M, 7075 to ASTM B247M, 7075 to ASTM B316/B316M, UNSA97075
- Venezuela:
7075 to COPANT 862
- Yugoslavia:
3.7553.00/AlZn5MgCu1.5 to JUS C.C2.100

Tradenames

Alcoa; Perunal

Typical uses

Aircraft structures & other components, weapons, bolts, sporting goods, mobile/cell phones, smart phones, laptops, tablets, computers, smart watches, fitness trackers, VR headsets, gaming consoles, electric cars, hybrid cars

Enlaces

MMPDS equivalent alloys

MMPDS similar alloys

ProcessUniverse

Producers

Reference

Shape



Ficha técnica: Tubo hueco fibra de carbono



Descripción

Tubos huecos realizados con fibra de carbono y resina epoxy.

Aplicaciones

Las tubos están realizados para aplicarlos en diferentes sectores y a diferentes productos, tanto en trabajos estructurales como estéticos.

Tabla de agentes químicos

Aceite caliente, diesel	+	Ácido sulfúrico < 5%	0	Glicol	0
Aceite crudo	+	Ácido tánico diluido < 7%	+	Grasas, aceites y ceras	+
Aceite de creosota (Ac. alquitrán)	-	Agua clorada	+	Hidrocarburos alifáticos (derivados de aceite crudo)	+
Aceites crudos y derivados	+	Álcalis (materiales básicos)	+	Hidrocarburos aromáticos (benceno, tolueno, xileno)	-
Aceites impregnados	+	Alcohol amílico	+	Hidróxido cálcico	+
Aceites minerales	+	Alcohol butílico	+	Hidróxido de bario	+
Aceites, vegetales y animales	+	Amil acetato	+	Hidróxido de magnesio	+
Acetona	0	Amoniaco	+	Hidróxido potásico 0-20%	+
Ácido ftálico, anhídrico ftálico	+	Anhídrido sulfuroso	+	Hidróxido sódico <20% (sosa caústica)	0
Ácido acético diluido < 5%	+	Baños de cromo	+	Lechada de cal	+
Ácido bronhídrico <10%	+	Benzol etilo (Etilbenceno)	-	Metanol (Alcohol metílico) <85%	0
Ácido carbólico (fenol)	-	Alcohol etílico	0	Naftaleno	-
Ácido clorhídrico < 10%	+	Bicarbonato sódico (sodio hidrogenocarbo)	+	Nafteno	-
Ácido clorhídrico 10-20%	+	Butil acetato	+	Parafina	+
Ácido cloroacético	-	Carbonato sódico (soda)	+	Percloroetileno	0
Ácido clorosulfónico	-	Cloroformo (triclorometano)	0	Peróxido de hidrógeno < 30%	+
Ácido creosólico	-	Cloruro sódico (sal cocina)	+	Petroleo (92-100 octanos)	+
Ácido crónico	+	Etanol < 85% (alcohol etílico)	0	Potasio carbonato	+
Ácido fluorhídrico diluido	0	Etil eter	+	Solución potasa caústica	+
Ácido fórmico > 10%	-	Gases de combustión	+	Tolueno	-
Ácido fosfórico <5%	+	Gasoil	+	Trementina	+
Ácido húmico	+	Glicerina	+	Tricloroetileno	0
Ácido maleico	+	Sulfuro de carbono	+	Xileno	-
Ácido nítrico < 5%	0	Tetracloruro de carbono (tetraclorometano)	+	+ = Resistente // 0 = Resistencia limitada	
Ácido oxálico < 25%	+	Tetralin (tetrahidronaftaleno)	0	- = No Resistente	

Características generales

Estas tablas se refieren a sólo dos de las muchas posibles orientaciones de las fibras. La mayoría de los componentes están hechos usando combinaciones de los materiales anteriores y las orientaciones de las fibras está dictadas por los requisitos de rendimiento del producto. ClipCarbono puede ayudar en el diseño de los componentes cuando sea requerido.

Propiedades mecánicas de Composites de Fibras (Carbono, Kevlar y Vidrio) con resina Epoxy (Curados a 120 °C)													
	Símbolo	Unidades	Fibra de Carbono tejida bidireccional (0°/90°)	Fibra de Carbono HM tejida bidireccional (0°/90°)	Fibra de Vidrio tejida bidireccional (0°/90°)	Fibra de Kevlar tejida bidireccional (0°/90°)	Fibra de Carbono Unidireccional (0°)	Fibra de Carbono HM Unidireccional (0°)	Fibra de Vidrio Unidireccional (0°)	Fibra de Kevlar Unidireccional (0°)	Acero S97	Aluminio L65	Titanio dtd 5173
Módulo de Young 0°	E1	GPa	70	85	25	30	135	175	40	75	207	72	110
Módulo de Young 90°	E2	GPa	70	85	25	30	10	8	8	6	207	72	110
Módulo de cizallamiento en el plano	G12	GPa	5	5	4	5	5	5	4	2	80	25	
Coefficiente de Poisson (Mayor)	v12		0.10	0.10	0.20	0.20	0.30	0.30	0.25	0.34			
Resistencia máxima a la rotura por tracción 0°	Xt	MPa	720	350	440	480	1500	1000	1000	1300	990	460	
Resistencia máxima a la rotura por compresión 0°	Xc	MPa	570	150	425	190	1200	850	600	280			
Resistencia máxima a la rotura por tracción 90°	Yt	MPa	720	350	440	480	50	40	30	30			
Resistencia máxima a la rotura por compresión 90°	Yc	MPa	570	150	425	190	250	200	110	140			
Resistencia máxima a la rotura por cizallamiento en plano	S	MPa	90	35	40	50	70	60	40	60			
Límite deformación por tracción 0°	ext	%	0.85	0.40	1.75	1.60	1.05	0.55	2.50	1.70			
Límite deformación por compresión 0°	exc	%	0.80	0.15	1.70	0.60	0.85	0.45	1.50	0.35			
Límite deformación por tracción 90°	eyt	%	0.85	0.40	1.75	1.60	0.50	0.50	0.35	0.50			
Límite deformación por compresión 90°	eyc	%	0.80	0.15	1.70	0.60	2.50	2.50	1.35	2.30			
Deformación por esfuerzo cortante máximo en el plano	es	%	1.80	0.70	1.00	1.00	1.40	1.20	1.00	3.00			
Densidad		g/cc	1.60	1.60	1.90	1.40	1.60	1.60	1.90	1.40	7,8	2,7	4,54
	Símbolo	Unidades	Fibra de Carbono tejida bidireccional (+45°/-45°)	Fibra de Vidrio tejida bidireccional (+45°/-45°)	Fibra de Carbono Unidireccional (0°)	Fibra de Carbono HM Unidireccional (0°)	Fibra de Vidrio Unidireccional (0°)	Acero	Aluminio				
Módulo longitudinal	E1	GPa	19.1	12.2	17	17	12.3	207	72				
Módulo transversal	E2	GPa	19.1	12.2	17	17	12.3	207	72				
Módulo de cizallamiento en el plano	G12	GPa	30	8	33	47	11	80	25				
Coefficiente de Poisson	v12		.74	.53	.77	.83	.53						
Resistencia a la tracción	Xt	MPa	120	120	110	110	90	990	460				
Resistencia a la compresión	Xc	MPa	120	120	110	110	90	990	460				
Resistencia al cizallamiento en el plano	S	MPa	310	150	260	210	100						

Exención de responsabilidad:

Estas tablas son para referencia / información, en ningún caso son una garantía de rendimiento. Se pretende exclusivamente facilitar información genérica a efectos comparativos ya que cada pieza fabricada van a sufrir variaciones. El usuario debe de evaluar la idoneidad de cada producto para su aplicación en concreto.

Ángulos de las fibras: "Las fibras se pueden colocar en cualquier ángulo dentro del tubo, con diferentes capas en diferentes ángulos para resistir las diversas cargas internas y externas aplicadas. Los tubos rara vez se hacen con todas las fibras a 0 ° o a 90 ° ya que de hacerlo así se dividirían fácilmente. este problema de división es el que presentan los tubos fabricados por pultrusión.

Las aplicaciones principales según los ángulos serían:

0 Grados (Axial)

Son tubos resistentes a la flexión longitudinal y axial de tracción / compresión

90 Grados (Arco)

Resisten la presión interna / externa y ayudan a los tubos a mantenerse redondos, consolidando los tubos fabricados por arrollamiento.

± 45 grados

Es el ángulo de la fibra ideal para resistir la torsión pura."

Tipos de fibras:

"Un tubo está compuesto de varias capas, el tipo de fibra y el ángulo para cada capa está dispuesta para dar las propiedades mecánicas globales requeridas por la aplicación.

(Las propiedades que figuran a continuación son para materiales compuestos hechos de fibras unidireccionales y resina epoxy)

Fibra de vidrio,

Una fibra de bajo coste con buena resistencia, pero relativamente baja rigidez y alta densidad.
Resistencia a la rotura 1.0 GPa, Módulo (Ex) 40 GPa, Densidad 1,9 g / cc

Fibra de aramida,

Comercialmente nombrado 'Kevlar' o 'Twaron', las fibras de aramida tienen una excelente resistencia a la tracción, casi dos veces más rígida que la fibra de vidrio y más ligera, pero a menudo tiene que ser combinada con otras fibras para lograr resistencias a la compresión aceptables.

Mecanizarla es un gran problema debido a su tenacidad y resistencia al corte.

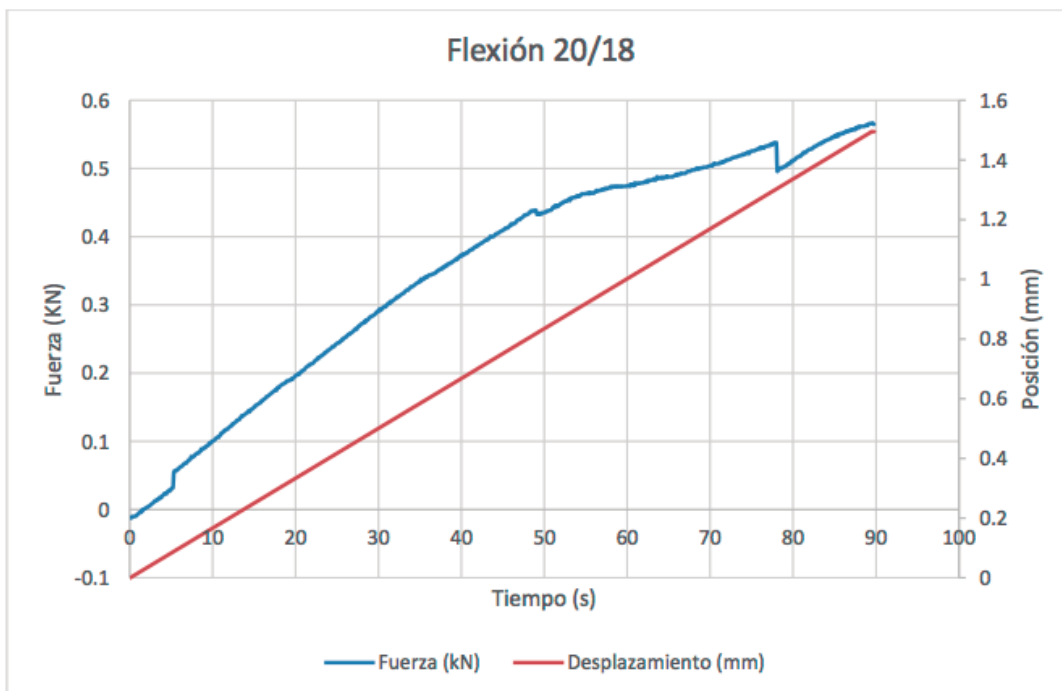
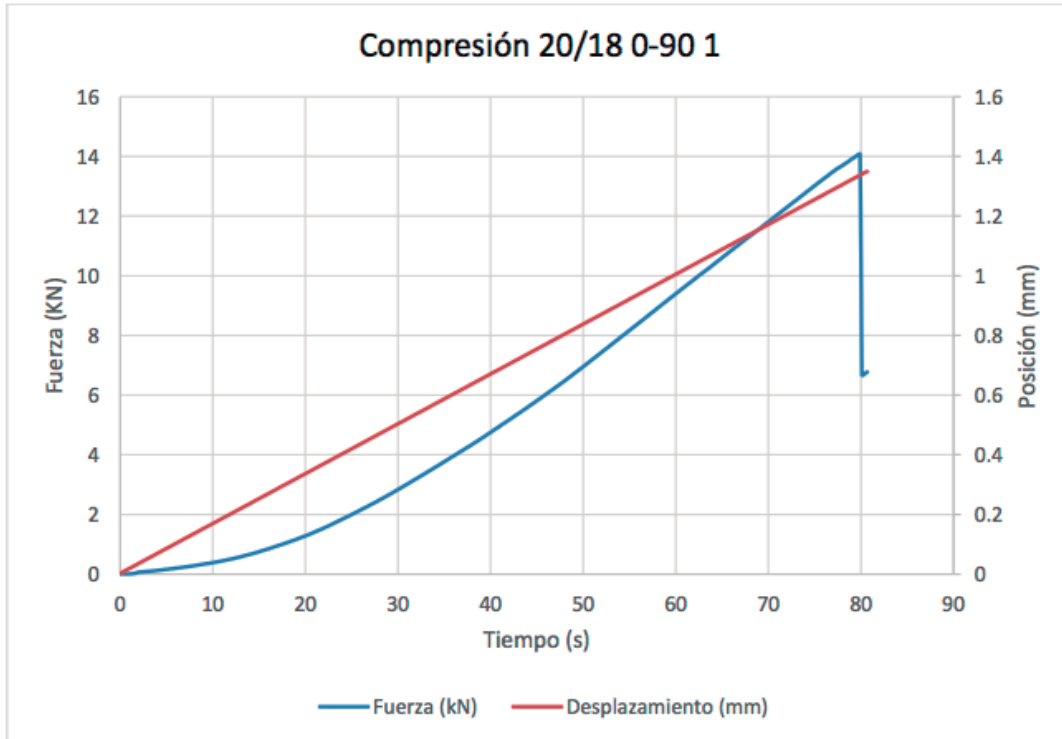
Resistencia a la rotura 1.3 GPa, Módulo (Ex) 75 GPa, Densidad 1,4 g / cc

Fibra de carbono,

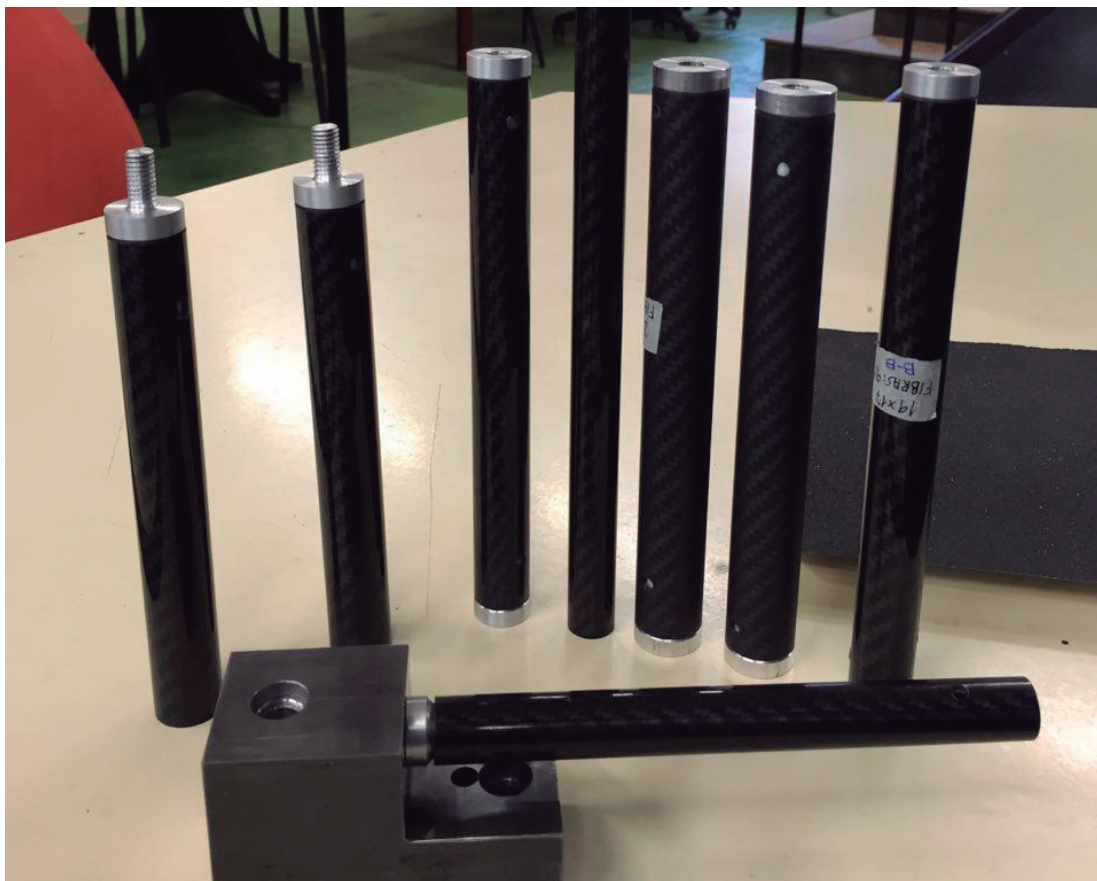
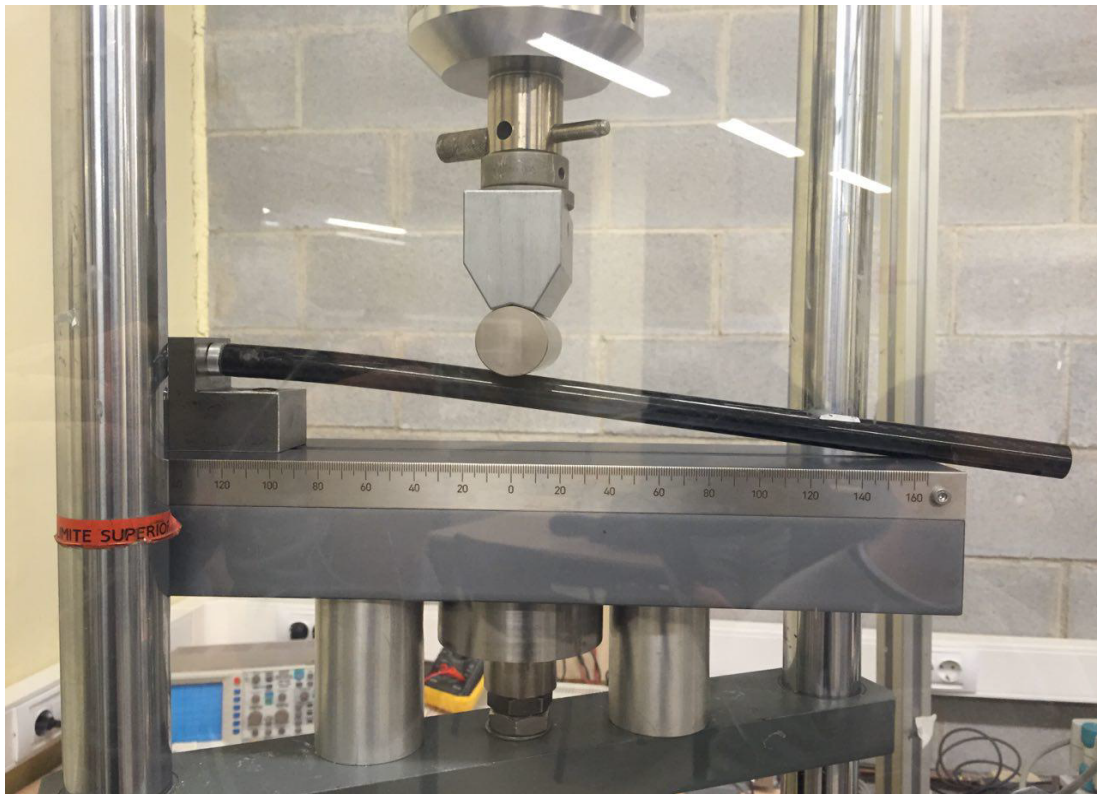
Tiene una muy buena combinación de fuerza con rigidez. Con un módulo específico de 92, más de tres veces superior al del metal (acero, titanio y aluminio tienen prácticamente el mismo en torno a 25)

Resistencia a la rotura 1,5 Gpa, Módulo (Ex) 130 GPa, Densidad 1,6 g / cc"

Ensayo tipo sobre tubo 100% fibra de carbono (0° / 90°) 20x18 mm.



Ensayo tipo sobre tubo 100% fibra de carbono (0° / 90°) 20x18 mm.





Adhesivo Epóxico Scotch-Weld^{MR} DP-420 Negro



Ficha Técnica

Descripción

Es un adhesivo de alto desempeño, compuesto de dos partes, que ofrece una resistencia superior al cizalle y al descascarado, y altos niveles de duración.

Características

- Alta resistencia al cizalle
- Alta resistencia al descascarado
- Desempeño ambiental sobresaliente
- Fácil de mezclar
- Flujo controlado
- Tiempo de trabajo 15-30 minutos
- Negro para calce de color y visibilidad

Características Físicas antes del Curado

	Base	Acelerador
Viscosidad @ 23°C	140,000 cps	19,500 cps
Resina Base	Epóxica	Am. Ite
Color	Negro	Ambar
Peso Neto (Kg/Lt)	1.125	1.09
Relación de Mezcla (B:A)	Volumen	2:1
	Peso	2:0.97
Tiempo de Trabajo (23°C)		
Mezclado:	20 gr	15 minutos
	10 gr	20 minutos
	5 gr	30 minutos

Características Térmicas Típicas de Curado

Físicas		
Color		Negro
Dureza Shore D		75-80
Térmicas		
Tg via DSC Coeficiente de Expansión Térmica (in./in./°C)	Bajo Tg	0.00008
	Sobre Tg	0.000194
Conductividad Térmica (btu · ft./ft. ² · hr. · °F) @ 45°C		0.104
Eléctricas		
Fuerza Dieléctrica (ASTM D 149)		888 volts/mil
Resistividad al Volumen (ASTM D 257)		1.6 x 10 ¹⁵ ohm-cm

Flujo





Scotch-Weld^{MR} DP-420 Negro

Ficha Técnica

Instrucciones de Uso

DP-420 negro en cartuchos Duo-Pack con jeringas plásticas duales para ser usadas con el sistema aplicador 3M^{MR} EPX^{MR}. Los cartuchos Duo-Pack están disponibles en 37 ml, 200 ml y 400 ml. Para usar el cartucho de 37 ml simplemente inserte el cartucho Duo-Pack en el aplicador EPX y encienda el desatascador dentro de los cilindros haciendo presión ligera sobre el gatillo. Luego, remueva la punta protectora del cartucho Duo-Pack y expela una pequeña cantidad de adhesivo para asegurarse que ambos lados del cartucho están fluyendo pareja y libremente. Si se desea mezclado simultáneo de la parte A y B, coloque la jeringa de mezclado EPX al cartucho Duo-Pack y comience a dispensar el adhesivo.

Con cartuchos neumáticamente aplicados de 200 ml, 400 ml y 37 ml, la jeringa debe estar colocada antes de dispensar cualquier material para prevenir que el adhesivo no mezclado se introduzca en el sujetador del aplicador de cartuchos. Una pequeña cantidad de material debería desecharse hasta que se logre consistencia, color uniforme y flujo parejo.

Cuando mezcle la parte A y la parte B manualmente, los componentes deben ser mezclados en la relación indicada en la sección "Características Físicas antes de Curado" de esta ficha técnica (pg 1). Una mezcla completa de los dos componentes es requerida para obtener propiedades óptimas.

Equipos de mezclado/dispensado/proporcionado de dos partes están disponibles para uso intermitente o para producción en línea. Estos sistemas son ideales para producción en línea debido a su tamaño de disparo y flujo variable. Son adaptables a la mayoría de las aplicaciones.

Preparación de la Superficie

MEK/Abrasión/MEK

Limpie la superficie con un estropajo empapado en metil etil ketona (MEK), gaste con Discos de Pulido 3M Scotch-Brite y limpie con un estropajo empapado en MEK. Permita que el solvente se evapore antes de aplicar el adhesivo.

Nota: Cuando use solventes, extinga todas las fuentes de ignición y siga las instrucciones y precauciones de uso de los fabricantes.

Características Típicas de Desempeño del Adhesivo

Sustratos y Pruebas

A. Cizalle de Traslapes (ASTM 1002-72)

Las fuerzas de cizalle de traslapes (FCT) fueron medidas sobre muestras de 2.54 cm de ancho, con un traslape de 1.25 cm. Estas uniones fueron hechas individualmente usando piezas del sustrato (2.54 cm x 10.16 cm) excepto para el aluminio. Dos paneles (1.6 mm de espesor, 10.16 cm x 17.8 cm) de aluminio revestido 2024 T-3 fueron unidos y cortados en muestras de 2.54 cm de ancho después de 24 horas. El espesor de la línea de unión fue entre 1.3 mm y 1.63 mm. Todas las fuerzas fueron medidas a 23°C excepto cuando se mencione lo contrario.

La tasa de separación de las mandíbulas de prueba fue 2.54 mm por minuto para los metales, 50.8 mm por minuto para plásticos y 508 mm por minuto para gomas. El espesor de los sustratos fue: acero - 1.5 mm; otros metales - 1.27 mm a 1.63 mm; gomas - 3.2 mm; plásticos - 3.2 mm.

B. T-peel (ASTM D 1002-72)

Las fuerzas de descascarado fueron medidas sobre uniones de 2.54 cm de ancho a 23°C. La tasa de separación de las mandíbulas de prueba fue 508 mm por minuto. Los sustratos tenían un espesor de 0.8 mm.

C. Ciclo de Curado

Con excepción de la tasa de pruebas de fuerza de levantamiento, todas las uniones fueron curadas durante 7 días a 23°C y 50% de humedad relativa antes de la prueba o sometidas a aquellas condiciones o envejecimiento ambiental.



Scotch-Weld^{MR} DP-420 Negro

Ficha Técnica

Aluminio, Cizalle de Traslape, a Temperatura (PSI)

Temperatura	PSI
-55°C	4500
23°C	4500
82°C (15 min) (1)	1000
(30 min) (1)	900
(60 min) (1)	1500
(4 hr) (1)	1500
121°C (15 min)	250

(1) Representa el tiempo en la cámara del horno de prueba antes de la prueba que se describe.



Metales, Cizalle de Traslape @ 23°C (PSI)

Aluminio	Grabado al Agua Fuerte	4500
	Oakite Degrease	4000
	MEK/Abrasión/MEK	2500
Acero Enrollado	MEK/Abrasión/MEK	2000
Cobre	MEK/Abrasión/MEK	2500
Latón	MEK/Abrasión/MEK	3000
Acero Inoxidable	MEK/Abrasión/MEK	1100
Acero Galvanizado	Hot Dipped	2000
	Electrodepositado	2500

Otros Sustratos, Cizalle de Traslape, @ 23°C (PSI)

Sustrato	Prep. Superficie 1	Prep. Superficie 2
ABS	450	600
PVC	525	500
Policarbonato	510	500
Poliacrílico	210	350
Poliestireno	450	450
FRP	700	1750
Phenolic	1400 (3)	1500 (3)
Acero/SBR	110	100
Acero/Neopreno	75	100 (3)

- 1 Limpieza con alcohol isopropílico.
- 2 Alcohol isopropílico/Abrasión/Alcohol Isopropílico
- 3 Falla del sustrato

Resistencia Ambiental

Ambiente	Condición	PSI
23°C / 50% HR	30 días	5000
Agua Destilada	30 días	4200
Vapor de Agua	49°C/100% HR, 30 días	4000
	93°C/100% HR, 14 días	3000
Anticongelante/H2O (50/50)	82°C, 30 días inmerso	3000
Alcohol Isopropílico	23°C, 30 días inmerso	4500
MEK	23°C, 30 días inmerso	3500
Sal en Spray (5%)	35°C, 30 días	2800
Skydrol LD-4	66°C, 30 días inmerso	4000

Para mayor información:

3 Centro de Atención al Consumidor

600-300-3636

E-mail: atencionconsumidor@3m.com